3-23-2017

Combined Stereo Vision and Inertial Navigation for Automated Aerial Refueling

Daniel T. Johnson

Follow this and additional works at: https://scholar.afit.edu/etd

Part of the Navigation, Guidance, Control and Dynamics Commons

COMBINED STEREO VISION AND INERTIAL NAVIGATION FOR AUTOMATED AERIAL REFUELING

THESIS

Daniel T. Johnson, Captain, USAF

AFIT-ENG-MS-17-M-036

DEPARTMENT OF THE AIR FORCE
AIR UNIVERSITY

AIR FORCE INSTITUTE OF TECHNOLOGY

Wright-Patterson Air Force Base, Ohio

COMBINED STEREO VISION AND INERTIAL NAVIGATION FOR AUTOMATED
AERIAL REFUELING

THESIS

Presented to the Faculty

Department of Electrical and Computer Engineering

Graduate School of Engineering and Management

Air Force Institute of Technology

Air University

Air Education and Training Command

in Partial Fulfillment of the Requirements for the

Degree of Master of Science in Electrical Engineering

Daniel T. Johnson, B.S.E.E.

Captain, USAF

23 March 2017

AFIT-ENG-MS-17-M-036

COMBINED STEREO VISION AND INERTIAL NAVIGATION FOR AUTOMATED

AERIAL REFUELING

THESIS

Daniel T. Johnson, B.S.E.E.
Captain, USAF

Committee Membership:

Dr. Scott Nykl
Chair

Dr. John Raquet
Member

Dr. Kyle Kauffman
Member

Dr. Robert Leishman
Member

AFIT-ENG-MS-17-M-036

Abstract

The lack of aerial refueling is a fundamental shortcoming of current Unmanned Aerial Vehicles (UAVs). UAV deployment continues to increase but the corresponding operational capabilities are limited by an inability to conduct extended operations. To alleviate this limitation and achieve the Air Forces global mobility and global strike missions, UAV must procure the capability to perform Automated Aerial Refueling (AAR). Such capability requires computing the precise relative attitude and separation (pose) between the tanker and unmanned receiver. This relative pose is fundamentally required to hold the receiver within the tankers refueling envelope throughout the duration of the refueling procedure.

The Global Positioning System (GPS) is one viable data source from which this relative navigation solution may be computed; however, GPS signals may be degraded or denied within an operational environment. Other sensors, such as Light Detection and Ranging (LiDAR), Machine Vision (MV), and Stereo Machine Vision (SMV), are also viable candidates. Other work has utilized different combinations of these sensors utilizing a Kalman Filter (KF) to compensate for individual weaknesses.

This work presents an integrated SMV / Inertial Navigation System (INS) as a method to compute the relative pose solution; optionally, GPS may be also integrated, if it is available. This integration is accomplished through design of an Extended Kalman Filter (EKF) used to bolster the SMV via INS/GPS. SMV errors caused by noise and processing are reduced by the EKF and the SMV prevents the INS from drifting. The INS/GPS/SMV EKF solution was generated and tested in a virtual simulation employing a stereo camera pair observing an approaching C12 aircraft in a custom 3D Virtual World (3DVW). Experimental results demonstrate that the EKF is able to combine SMV and GPS with INS individually or in tandem to achieve Root Mean Squared Error (RMSE) less than 2 cm when both sensors are available. When GPS is denied or lost the EKF with SMV achieves RMSE less than 10 cm at distances greater than 20 m from the stereo camera system.

iv

Acknowledgements

First, I wish to thank my advisor, Dr. Scott Nykl. His willingness to provide hours of guidance, amidst his own busy schedule, was indispensable. I also wish to thank the members of my committee, Dr. John Raquet, Dr. Kyle Kauffman, and Dr. Robert Leishman, who also sacrificed much of their valuable time to provide support, correction, and advice. I want to acknowledge Mr. Daniel Marietta for his aid in helping me to understand and implement the ANT Center provided code essential to my work. I wish to extend a special thanks to Maj Scott Pierce who provided significant help to me in the early stages of research but was required to leave the committee due to his unexpected deployment. I also wish to thank my sponsors, Mr. Ba Nguyen, Mr. Dan Schreiter, and the rest of AFRL/RQ Aerospace Systems directorate, for their support and feedback throughout this experiment. My wife was critical to my success. Her support and encouragement throughout this process helped to keep me focused. Lastly, I thank God for His work in my life. He gave me this opportunity, and He is the reason for my success. Without Him I am nothing.

Table of Contents

List of Figures

xi

List of Tables

List of Abbreviations

COMBINED STEREO VISION AND INERTIAL NAVIGATION FOR AUTOMATED AERIAL REFUELING

I. Introduction

Since the Berlin Airlift, it has been no secret that the United States Air Force (USAF) is capable of rapidly responding to any situation at any necessary scale. The Berlin Airlift required a mission to be flown every 90 seconds delivering 2,323,738 tons of supplies to West Berlin [9]. It was this venture that set the stage for the Allies resisting future Soviet advances and growth. Since then Global Mobility and Global Strike have been cemented as two of the Core Missions of the Air force. For both of theses Missions, in-flight-refueling is a key capability requirement. Aerial refueling enables increased range and increased flight time for extended missions enabling the USAF to meet its Core Missions [10]. However, there is currently no system in place that allows Unmanned Aerial Vehicles (UAVs) to take advantage of this capability. UAV use in the last decade and a half has risen significantly. Between 2002 and 2010 the Department of Defense (DoD) increased the number of UAVs by a factor of 40 [11] and, in 2010, the USAF procured more unmanned than manned aircraft [12]. As UAV use increases the USAF is looking for ways to bring aerial refueling to UAVs. In order to do this, the process must be automated leading to Automated Aerial Refueling (AAR). The DoD is heavily researching ways to make AAR for UAVs possible.

Many different technologies have already been evaluated for their effectiveness in AAR use. GPS was looked at early on and found to be capable of achieving cm level accuracy [13,14]. However, GPS may not be robust enough. It is susceptible to denial and degradation or blockage from the tanker while refueling [15]. To rectify this, other technologies have also been tested. Optics have been a strong field of study in the last decade. Areas such as LiDAR [1], Monocular Machine Vision (MV) [16,17], and SMV [8,18,19] have all been explored. Specifically for MV and GPS, research has been conducted to combine multiple

sensors to minimize the weaknesses in each. Initially this was as simple as using GPS while it is available, and using the MV as soon as the receiver is too close to the tanker for the GPS to be effective [5, 20]. A more effective approach has been to combine the MV and GPS with INS through the use of a KF [6, 21, 22].

Currently, none of this work has explored combining SMV with other sensors in the same fashion. Additionally, the majority of the work combining sensors have two key issues that can not be ignored. First, most of the optical approaches involve the receiver aircraft looking up at the aircraft, with the exception of [22,23]. This potentially requires impossibly expensive and impractical modification to receiver platforms. The upcoming KC-46 Pegasus refueling tanker already has a stereo camera system in place for the boom operators which could be utilized to perform SMV [24]. Additionally, many of the vision algorithms used rely on markers or beacons to assist the MV systems [6, 22, 23, 25] which may require additional expensive modifications to all receiver aircraft. Combining SMV, GPS, and INS through a KF will allow the system to make the best use of all three sensors and take advantage of the existing KC-46 technology.

1.1 Problem Statement

The goal of this research is to demonstrate the effectiveness of combining SMV pose estimation with GPS/INS data for AAR utilizing a realistic simulated aerial refueling trajectory. Both a tanker and a receiver aircraft will be represented in the simulated refueling trajectory. The SMV estimate from the refueling tanker, the relative position estimate generated by the INS from both aircraft, and DGPS will be combined through the use of the EKF. This research will test different combinations of SMV, DGPS, and INS sensors with the EKF to compare their performance in estimating the relative position of the two aircraft. Quantitative analysis will be conducted on the accuracy and reliability of each approach to determine the effectiveness of adding SMV estimates as well as the effectiveness of the individual approaches.

1.2 Scope and Assumptions

This research specifically looks at combining the SMV, GPS, and INS in an EKF within a simulated environment. The EKF will be designed to handle all necessary measurements. Multiple filters designs are not evaluated though variations on tuning parameters are explored. All sensor data is simulated. The INS data is generated from navigation grade IMU specifications. Because of this, the attitude measurements of the SMV system will not be incorporated or evaluated. For the duration of this simulation, the INS attitude calculations are more accurate than what the SMV system can provide.

While the research uses actual computed SMV measurements from a 3D Virtual World (3DVW) [26, 27], the development of the algorithm to calculate those measurements is not a part of this work. Instead, this research uses the algorithm implemented by [28, 29]. The simulated cameras used to generate the SMV measurements are considered ideal, without distortion effects.

The SMV algorithm will be run in the 3DVW on a realistic AAR flight path in order to test it as accurately as possible. This simulated receiver will follow a direct approach from the rear of the tanker. Approaches from formation will not be evaluated. The flight path will be generated with flight dynamics software to ensure the aircrafts' relative poses align with realistic flight [30]. No additional noise will be injected into the virtual world. There are accurate flight dynamics, but no additional turbulence, wind, or wake effects.

1.3 Overview

This thesis is organized into five chapters: Introduction (I), Background and Previous Work (II), Methodology (III), Results and Analysis (IV), and Conclusion (V). Chapter I, provides a brief overview of the motivation behind this research and what makes it necessary and useful. It also bounds what is going to be explained and studied through this research. This will include some brief background and history, but the majority of that will be covered in Chapter II.

Chapter II really consists of two different sections. The first is the theory overview.

Some of the concepts used later in the research require explanation of the basic background and mathematical theory behind their operation to set up more detailed, research specific explanations in Chapter III. The second section is the background. This covers the concepts and ideas that have been implemented or studied previously that are relevant, included, or built upon in this research. Topics include the GPS, LiDAR, MV, and SMV measurement techniques as well as the Fuzzy Filter and EKF sensor fusion techniques.

Chapter III explains the specific approach used to perform the experiment. It further develops some of the theory from Chapter II into the specific designs such as the development of the error state filter model and the relative filter. All aspects of the simulation are explained as well, beginning with simulated flight paths and sensor generation through implementation of the filter software. It also contains some results of preliminary work required to successfully implement the filter. However, the major results of the research are contained in Chapter IV.

Chapter IV presents the experimental findings. Filter performance is displayed for the different scenarios and tuning parameters used in the experiment. Following presentation of the data, the different implementations are compared and evaluated. Finally, the impact of the results will be discussed.

Chapter V summarizes what was accomplished in this research. This will highlight important take-aways from the results and discuss what could be done to fix or improve them. This chapter will provide recommendations for future work that could improve or build upon the work that was accomplished here.

II. Background and Previous Work

This chapter provides the necessary background on the theories and techniques used to perform this research. Critical topics include KFs, INSs, and SMV. A presentation of past research work is also outlined.

2.1 Reference Frames

The information obtained in navigation is only useful when the frame of reference is known. While there are a many different reference frames commonly used to determine navigation solutions, this section explains the basic definitions for the frames used in this specific research.

2.1.1 Earth-Centered Inertial Frame.

The Earth-Centered Inertial Frame (ECI) is a reference frame aligned with the center of the earth, the earth's spin axis, and the stars. The earth's center is the center of the ellipsoidal representation of the earth's surface. The inertial label indicates that the frame does not rotate with the earth's rotation. Any object stationary on the earth has motion within ECI to match the rotation of the earth. A complete definition requires identifying a point at which the ECI and the Earth-Centered Earth Fixed (ECEF) align. Although other definitions exist, the scientific community achieves this point by directing the x-axis to point from the earth to the sun at the vernal equinox. The ECI is notated with the symbol i [31].

2.1.2 Earth-Centered Earth-Fixed.

The ECEF frame is similar to the ECI frame except, as the name suggests, it is fixed to the earth and rotates with it. It shares the same origin as the ECI frame, and the z-axis is also aligned with the earth's spin axis pointing toward the true North Pole. The x-axis points from the origin to the meridian defining $0°$ longitude and the y-axis points from the origin to the $90°$ east meridian. Because position is often needed relative to the earth,

the ECEF frame is necessary for an absolute representation of such a position. The ECEF frame is notated with the symbol e [31].

2.1.3 Local Navigation Frame.

The Local Navigation (Nav) frame is different from the previous two frames due to its use of a moving origin. The origin of the Nav frame is the object described by a navigation solution. One common Nav frame definition is North-East-Down (NED). The z-axis is the line from the origin down to the point normal to the surface of the ellipsoidal representation of the earth's surface. The x-axis points from the origin to the North Pole but is maintained orthogonal to the z-axis. The y-axis is defined to be the line pointing from the origin to the east, and it is also orthogonal to z- and x-axes. This research will use the NED frame. The NED frame is notated with the symbol n [31]. The NED frame is in Figure 2.

2.1.4 Body Frame.

The Body frame shares its origin with the Nav frame. The primary purpose of the Body frame is to notate the origin and orientation of the object of interest. The z-axis points down from the bottom of the object. The x-axis points forward, often in the direction of travel. The y-axis points out the right side of the object. The three axes are orthogonal to each other like the other reference frames. The Body frame is most useful for describing the angular motion of an object. Common methods for describing the rotations about the z-, x-, and y-axes in aircraft are roll, pitch, and yaw. Many of the sensors used to determine navigation solution reside in the Body frame [31]. The Body frame is notated with the symbol b. The Body frame is in Figure 1.

Figure 1. 3DVW Setup and Reference Frames

2.1.5   Geodetic Frame.

The World Geodetic System 1984 (WGS-84) is a Conventional Terrestrial Reference System (CTRS). WGS-84 works with the understanding that spherical models of the earth are inadequate, and the earth is best represented as an ellipsoid of equal gravitational potential. The geodetic coordinate system is based off of the surface of this ellipsoid while the origin is the center of the ellipsoid. The z-axis points from the origin to the International Earth Rotation and Reference System Service (IERS) Reference Pole. The x-axis points from the origin to the Bureau International del'Heure (BIH) Zero Meridian orthogonal to the z-axis. The y-axis is defined as orthogonal to both the x-axis and the z-axis in a right-handed coordinate system. However, Geodetic frame coordinates are not expressed relative to x-, y-, and z-axes. Instead, they are expressed in latitude, longitude, and height. Latitude is the angle from the equator, the x-,y-plane, to the North Pole. Longitude is the angle between the Zero Meridian plane and the plane formed by the meridian of the object location. Height is defined as the orthogonal distance from the ellipsoid surface. Geodetic coordinates can also be used to track the location of the origin for navigation solutions. When an object is traveling along the surface of the earth, its motion is easiest to define relative to the earth. Geodetic coordinates easily make this reference at any point on the surface by representing each point as two rotations and a height above the ellipsoid [32].
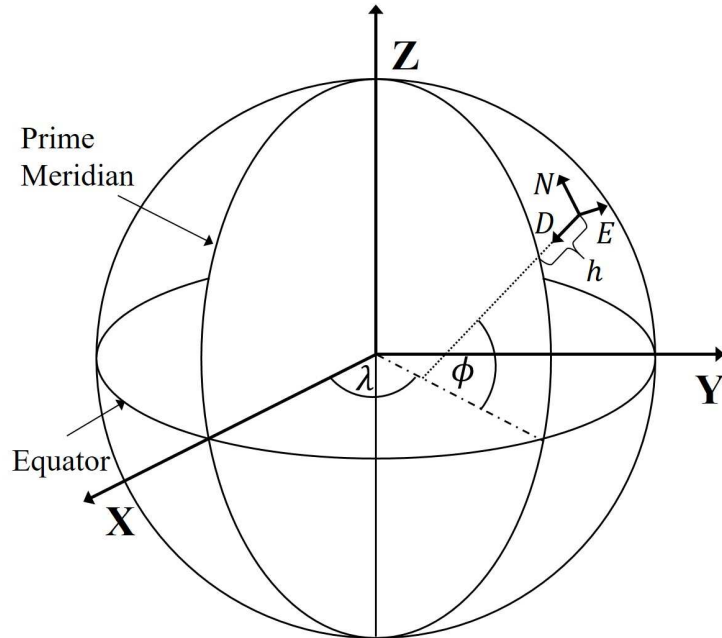
Figure 2. NED and Geodetic frames

2.2 Notation

This section explains some of the notation that will be used throughout this document.

Scalar: represented by upper or lower case letters

ex: A or a

Vector: represented by bold lower case letters

ex: $\mathbf{a}$

Matrix: represented by bold upper case letters

ex: $\mathbf{A}$

DCM: subscripts indicate starting reference frame, superscripts represent ending reference frame

ex: $\mathbf{x}^b \mathbf{C}_a^b \mathbf{x}^a$ rotates vector $\mathbf{x}$ from frame a to frame b

Rotations: subscripts represent relative rotations from one frame to another, super-
scripts represent frame of reference

ex: $\mathbf{\Omega}_{ba}^c$ is the rotation of a relative to b expressed in frame c

Time: represented as a function of t or a subscript of another variable

ex: $\mathbf{x}_i$ and $\mathbf{x}(t_i)$ both represent the vector $\mathbf{x}$ at time i

2.3 Kalman Filters

The KF is a recursive algorithm used to combine data for reduced estimation error. KFs are commonly used to estimate information such as position, speed, and attitude required for navigation. These values are the system states. The KF performs estimation by determining the statistical mean of the states and their associated covariance or uncertainty. Each KF performs two basic actions: propagate and update. The propagate stage utilizes the known system dynamics to predict future states when measurements are not available. As the system propagates with no known measurements, the covariance continues growing to accurately represent the knowledge of the system. The update stage incorporates measurements and utilizes their known mean and covariances to correct the propagated estimate. The effectiveness of the KF lies in its ability to utilize all information given to it regardless of the quality. The update state uses the measurements and their known covariances to correct the system estimates. While all measurements improve the system uncertainty, measurements with large uncertainty impact the system less than measurements with low uncertainty. The KF and EKF are discussed in this section.

2.3.1 Kalman Filter.

The basic KF, or Linear KF, forms the structure that the EKF also utilizes. However, the KF requires the system and measurement dynamics to be linear. This limitation is discussed further in Section 2.3.2. The KF dynamics are defined by

$$\dot{\mathbf{x}}(t) = \mathbf{F}(t)\mathbf{x}(t) + \mathbf{B}(t)\mathbf{u}(t) + \mathbf{G}(t)\mathbf{w}(t) \tag{1}$$

which represents the derivative $\dot{\mathbf{x}}(t)$ of the states, $\mathbf{x}(t)$. In Equation (1), $\mathbf{F}(t)$ models the state dynamics, $\mathbf{B}(t)$ is the input matrix, and $\mathbf{G}(t)$ is the noise matrix while $\mathbf{u}(t)$ represents the known control inputs and $\mathbf{w}(t)$ represents the white, zero-mean, Gaussian system noises. Likewise, the measurement dynamics are defined in the same fashion. The measurement dynamics for a measurement $\mathbf{z}(t_i)$ at a given time t_i are defined by

$$\mathbf{z}(t_i) = \mathbf{H}(t_i)\mathbf{x}(t_i) + \mathbf{v}(t_i) \tag{2}$$

where $\mathbf{H}(t_i)$ is the measurement matrix relating the measurement to the states and $\mathbf{v}(t_i)$ is the white, zero-mean, Gaussian measurement noise. Equation (1) forms the basis of a filter in continuous time while Equation (2) shows measurements can only be taken in a discrete time (t_i). To account for this Equation (1) is modified to

$$\mathbf{x}(t_{i+1}) = \mathbf{\Phi}(t_i)\mathbf{x}(t_i) + \mathbf{B_d}(t_i)\mathbf{u}(t_i) + \mathbf{w_d}(t_i) \tag{3}$$

where $\mathbf{w_d}(t_i)$ is the discrete noise realization, $\mathbf{B_d}(t_i)$ is the discrete input matrix, and $\mathbf{\Phi}(t_i)$ is the discrete state transition matrix defined by

$$\mathbf{\Phi} = e^{\mathbf{F}\Delta t} \tag{4}$$

For this research there are no known control inputs to the system so the $\mathbf{B}$ term is ignored for all future equations [33].

2.3.1.1 KF Propagate.

The propagate equation with the inputs removed for the KF estimate to a discrete point in time i is

$$\widehat{\mathbf{x}}_i^- = \mathbf{\Phi}_{i-1}\widehat{\mathbf{x}}_{i-1}^+ \tag{5}$$

where $\widehat{\mathbf{x}}_{i-1}^+$ is the state estimate of $\mathbf{x}(t_{i-1})$ after any measurements have been incorporated, and $\widehat{\mathbf{x}}_i^-$ is the state estimate at the next time step before any measurements are incorporated.

A $^-$ denotes the a priori estimate before a measurement is incorporated at that time. A $^+$ denotes the a posteriori estimate after the measurement is incorporated. The state's covariance propagation equation for $\mathbf{P}$ is

$$\mathbf{P}_i^- = \mathbf{\Phi}_{i-1}\mathbf{P}_{i-1}^+\mathbf{\Phi}_{i-1}^T + \mathbf{Q}_d \tag{6}$$

where $\mathbf{Q}_d$ is the discretized noise covariance defined by

$$\mathbf{Q}_d = \int_{t_{i-1}}^{t_i} \mathbf{\Phi}(t_i - \tau)\mathbf{G}\mathbf{Q}(\tau)\mathbf{G}^T\mathbf{\Phi}(t_i - \tau)^T d\tau \tag{7}$$

Adding $\mathbf{Q}_d$ incorporates the new process noise being added to the system at each step [33].

2.3.1.2 KF Update.

The measurement dynamics model was defined in Equation (2) but the update equations define how the filter will incorporate the new measurements. Before updating the state estimate or covariance, the Kalman gain $\mathbf{K}$ is calculated by

$$\mathbf{K}_i = \mathbf{P}_i^-\mathbf{H}^T \left[\mathbf{H}\mathbf{P}_i^-\mathbf{H}^T + \mathbf{R}_i\right]^{-1} \tag{8}$$

where $\mathbf{R}_i$ is the measurement noise covariance matrix. Once $\mathbf{K}$ is calculated the new state estimate is

$$\widehat{\mathbf{x}}_i^+ = \widehat{\mathbf{x}}_i^- + \mathbf{K}_i \left[\mathbf{z}_i - \mathbf{H}\widehat{\mathbf{x}}_i^-\right] \tag{9}$$

where $\mathbf{z}_i$ is the measurement at time i. The covariance is calculated by

$$\mathbf{P}_i^+ = \mathbf{P}_i^- - \mathbf{K}_i\mathbf{H}\mathbf{P}_i^- \tag{10}$$

Once updated, the new post measurement estimate and covariance are fed back into the propagate equations to continue the estimation for future times [33].

2.3.2 Extended Kalman Filter.

The EKF utilizes the same basic principles as the KF but slightly modifies the approach to help account for nonlinear system and measurement dynamics. Thus, the dynamics defined in Equation (1) change to account for the nonlinearity. The dynamics representing how $\mathbf{x}(t)$ change over time are now

$$\dot{\mathbf{x}}(t) = \mathbf{f}\left[\mathbf{x}(t), \mathbf{u}(t), t\right] + \mathbf{G}(t)\mathbf{w}(t) \tag{11}$$

and are a function of the current state, inputs and time with noise. The measurement equation is also modified in the same way giving

$$\mathbf{z}(t) = \mathbf{h}\left[\mathbf{x}(t), t\right] + \mathbf{v}(t) \tag{12}$$

where it is a function of the current state and time with noise. To account for the new dynamics, the EKF linearizes about a nominal estimate. Modifying the system dynamics again provides

$$\dot{\mathbf{x}}_n(t) = \mathbf{f}\left[\mathbf{x}_n(t), \mathbf{u}(t), t\right] \tag{13}$$

and

$$\mathbf{z}_n(t) = \mathbf{h}\left[\mathbf{x}_n(t), t\right] \tag{14}$$

for the measurement dynamics, where $\dot{\mathbf{x}}_n(t)$ is the nominal state and $\mathbf{z}_n(t)$ is the nominal measurement. Because the nominal state does not perfectly match the true state, there is a difference between the two values called the perturbation defined by

$$\left[\mathbf{x}(t) - \mathbf{x}_n(t)\right] \tag{15}$$

resulting in the perturbation equation

$$\delta\dot{\mathbf{x}}(t) = \mathbf{F}\left[t; \mathbf{x}_n(t)\right]\delta\mathbf{x}(t) + \mathbf{G}(t)\mathbf{w}(t) \tag{16}$$

where $\mathbf{F}$ is determined by finding the Jacobian of $\mathbf{f}$

$$\mathbf{F}\left[t; \mathbf{x}_n(t)\right] = \left. \frac{\partial \mathbf{f}\left[\mathbf{x}, \mathbf{u}(t), t\right]}{\partial \mathbf{x}} \right|_{\mathbf{x}=\mathbf{x}_n(t)} \tag{17}$$

at the nominal value of $\mathbf{x}$. A similar perturbation model is defined for the measurements

$$\delta \mathbf{z}(t_i) = \mathbf{H}\left[t; \mathbf{x}_n(t)\right] \delta \mathbf{x}(t_i) + \mathbf{v}(t_i) \tag{18}$$

where the Jacobian is also used such that

$$\mathbf{H}\left[t_i; \mathbf{x}_n(t)\right] = \left. \frac{\partial \mathbf{h}\left[\mathbf{x}, t_i\right]}{\partial \mathbf{x}} \right|_{\mathbf{x}=\mathbf{x}_n(t_i)} \tag{19}$$

The EKF estimates the perturbation of the nominal instead of measuring the estimate states. Thus, the resulting output of the filter is the best estimate of the perturbation about the nominal. To obtain the best estimate of the states, $\widehat{\mathbf{x}}(t)$ is determined by

$$\widehat{\mathbf{x}}(t) \triangleq \mathbf{x}_n(t) + \widehat{\delta \mathbf{x}}(t) \tag{20}$$

where the best estimate of the perturbations, $\widehat{\delta \mathbf{x}}(t)$ is added to the nominal value. Once a measurement is incorporated and the system is re-linearized, the best estimate of the perturbation $\widehat{\delta \mathbf{x}}(t)$ is now 0 giving

$$\mathbf{x}_n(t_i) = \widehat{\mathbf{x}}(t_i^+) \tag{21}$$

for the new nominal value [33].

2.3.2.1 EKF Propagate.

Since the EKF is estimating the perturbation, $\widehat{\mathbf{x}}$ is propagated by integrating the linearized state dynamics according to

$$\widehat{\mathbf{x}}_{t_{i+1}}^- = \widehat{\mathbf{x}}_i^+ + \int_{t_i}^{t_{i+1}} \mathbf{f}\left[\widehat{\mathbf{x}}_i^+, \mathbf{u}, t_i\right] dt \tag{22}$$

13

The propagation of the state covariances is found by

$$\mathbf{P}_{i+1}^- = \mathbf{\Phi}_i \mathbf{P}_i^+ \mathbf{\Phi}_i^T + \mathbf{Q}_{\mathbf{d}i} \tag{23}$$

which appears identical to Equation (6). However, $\mathbf{\Phi}$ is calculated using Equation (4) and $\mathbf{F}$ found in Equation (17) [33].

2.3.2.2 EKF Update.

The measurement update portion of the EKF, like most of the EKF, is similar to the process in Section 2.3.1.2 while still maintaining some differences. The Kalman gain $\mathbf{K}$ can be found by

$$\mathbf{K}_{i+1} = \mathbf{P}_{i+1}^- \mathbf{H}^T \left[t_{i+1}; \widehat{\mathbf{x}}_{i+1}^- \right] \left\{ \mathbf{H} \left[t_{i+1}; \widehat{\mathbf{x}}_{i+1}^- \right] \mathbf{P}_{i+1}^- \mathbf{H}^T \left[t_{i+1}; \widehat{\mathbf{x}}_{i+1}^- \right] + \mathbf{R}_{i+1} \right\}^{-1} \tag{24}$$

where $\mathbf{H}$ comes from Equation (19). The resulting update equation for the perturbation estimate is

$$\widehat{\delta \mathbf{x}}_{i+1}^+ = \widehat{\delta \mathbf{x}}_{i+1}^- + \mathbf{K}_{i+1} \left\{ \mathbf{z}_{i+1} - \mathbf{z}_n(t_i) - \mathbf{H}_{i+1} \widehat{\delta \mathbf{x}}_{i+1}^- \right\} \tag{25}$$

Recall that $\widehat{\delta \mathbf{x}}_{i+1}^-$ becomes 0 after the update and re-linearizion. Propagating this perturbation will simply propagate 0 meaning that $\widehat{\delta \mathbf{x}}_{i+1}^- = 0$ and the update equation for the perturbation now becomes

$$\widehat{\delta \mathbf{x}}_{i+1}^+ = \mathbf{K}_{i+1} \left\{ \mathbf{z}_{i+1} - \mathbf{h} \left[\mathbf{x}_{n,t+1}, t_{i+1} \right] \right\} \tag{26}$$

Utilizing Equation (20) and Equation (26) the updated state estimate becomes

$$\widehat{\mathbf{x}}_{i+1}^+ = \widehat{\mathbf{x}}_{i+1}^- + \mathbf{K}_{i+1} \left\{ \mathbf{z}_{i+1} - \mathbf{h} \left[\mathbf{x}_{n,i+1}, t_{i+1} \right] \right\} \tag{27}$$

and the updated covariance matrix becomes

$$\mathbf{P}_{i+1}^+ = \mathbf{P}_{i+1}^- - \mathbf{K}_{i+1} \mathbf{H} \left[t_{i+1}; \widehat{\mathbf{x}}_{i+1}^- \right] \mathbf{P}_{i+1}^- \tag{28}$$

Once the measurements have received an update, the filter will re-linearize, zero out the perturbation estimate, and repeat the process of propagating and updating. By repeatedly performing this process, the EKF will approximate the nonlinear dynamics as a first order linear system provided the nominal estimate does not drift too far from the truth [33].

2.4   Inertial Navigation System

The IMU is the core sensor for the filter used in this research. It provides both the mechanized positions for each aircraft and the error models used as the basis for the EKF propagation. This research uses a simulated strapdown IMU producing three dimension accelerations and rotational rates. An INS is a self-contained system capable of determining a vehicles navigation state. Unlike most other navigation techniques, an INS does not require any external inputs or measurements from the environment once initialized. The system drift over time makes it unlikely to be the sole source of measurement, but the self-contained system makes it a critical component of many navigation systems.

2.4.1   INS Basic Operation.

The INS contains two basic components, an IMU and a processor, although the IMU and processor may be different components of a larger system [34]. Each IMU contains three rate gyroscopes and three accelerometers. Each gyro is capable of measuring the angular rate about a single axis. Thus, three gyros are placed orthogonally in the IMU to allow it to measure angular rates about all three axes. Like the gyro, each accelerometer is able to measure in a single axis, requiring three orthogonally placed units. However, accelerometers measure the specific force along that axis. Therefore, the accelerometers measure both the forces acting on the vehicle due to its acceleration and the forces acting on the vehicle due to gravity. The accelerometer is unable to differentiate between the acceleration forces and the gravitational forces. To accurately calculate the inertial accelerations, the measured effects of gravity must be removed before being integrated. The integration is performed by the processor in the INS or by the part of the IMU found in the larger system [31]. This process is discussed more in Section 2.4.2.

2.4.2 Inertial Navigation System Equations.

The mechanization of IMU measurements within an INS is a well-developed set of equations. This paper uses the equations and methods from Titterton and Weston [34].

The current state, $\mathbf{x}$, of each aircraft is stored as navigation data. $\mathbf{p}^w$ is the current position in Geodetic coordinates consisting of the latitude L, the longitude ℓ and the Height Above Ellipsoid (HAE) h. The term $\mathbf{v}^n$ is the velocity in the NED frame. The term $\mathbf{C}_b^n$ is the Direction Cosine Matrix (DCM) representing the rotation from the body frame to the NED frame.

The state is updated by mechanizing the local navigation frame strapdown inertial navigation equations shown in Equations (29) to (31) [34]. The position navigation equation is

$$\dot{\mathbf{p}}^n = \mathbf{v}^n \tag{29}$$

where $\dot{\mathbf{p}}^n$ is the derivative of the NED position. The NED velocity vector, $\mathbf{v}^n$, will be discussed further in Equation (34). The velocity navigation equation is

$$\dot{\mathbf{v}}^n = \mathbf{C}_b^n \mathbf{f}^b - (2\boldsymbol{\omega}_{ie}^n + \boldsymbol{\omega}_{en}^n) \times \mathbf{v}^n + \mathbf{g}_l^n \tag{30}$$

where $\dot{\mathbf{v}}^n$ is the derivative of the NED velocity, $\mathbf{f}^b$ is the specific force vector measured by the IMU, $\boldsymbol{\omega}_{ie}^n$ is the earth rotation rate in the NED frame, $\boldsymbol{\omega}_{en}^n$ is the rotation of the NED frame relative to the earth in the NED frame, also called the transport rate, and $\mathbf{g}_l^n$ is the local gravity expressed in the NED frame. The rotation navigation equation is

$$\dot{\mathbf{C}}_b^n = \mathbf{C}_b^n \boldsymbol{\Omega}_{nb}^b \tag{31}$$

where $\dot{\mathbf{C}}_b^n$ is the derivative of the body to NED rotation and $\boldsymbol{\Omega}_{nb}^b$ is the matrix form of the body rate. The matrix form of the body rate is defined as

$$\boldsymbol{\Omega}_{nb}^b = \left[\boldsymbol{\omega}_{nb}^b\right]_\times \tag{32}$$

where $\boldsymbol{\omega}_{nb}^b$ is the body rate with respect to the NED frame expressed in the body frame, and the $[\ ]_\times$ places that vector into a skew symmetric cross product matrix. The IMU measures all of the rates, not just the rates in the NED frame. To calculate the rates in the NED frame, the components not caused by the direct motion of the aircraft must be removed. Thus, the body rate with respect to the NED frame can be found by differencing the measured body rates and the navigation frame rates expressed in the body frame. This is broken down by

$$\boldsymbol{\omega}_{nb}^b = \boldsymbol{\omega}_{ib}^b - \mathbf{C}_n^b \left[\boldsymbol{\omega}_{ie}^n + \boldsymbol{\omega}_{en}^n \right] \tag{33}$$

where $\boldsymbol{\omega}_{ib}^b$ represents the measured body rates provided by the IMU and $\mathbf{C}_n^b = [\mathbf{C}_b^n]^T$. The earth's rotation and the the frame's transport rate are both summed and rotated into the body frame before differencing with the measured rates.

One additional step is required because Equation (29) is expressed in the NED frame while the current position is expressed in Geodetic coordinates. The rate of change for the position in the Geodetic frame is defined as

$$\dot{\mathbf{p}}^w = \begin{bmatrix} \dot{L} \\ \dot{\ell} \\ \dot{h} \end{bmatrix} = \begin{bmatrix} \dfrac{v_N}{R_N + h} \\ \dfrac{v_E \sec L}{R_E + h} \\ -v_D \end{bmatrix} \; ; \qquad \mathbf{v}^n = \begin{bmatrix} v_N \\ v_E \\ v_D \end{bmatrix} . \tag{34}$$

where $\dot{L}$ is the rate of change in the latitude, $\dot{\ell}$ is the rate of change in the longitude, $\dot{h}$ is the rate of change in the height, R_N is the meridian radius of curvature and R_E is the transverse radius of curvature. The velocity vector $\mathbf{v}^n$ is broken into v_N, v_E, and v_D, the north, east, and down velocities respectively. The final Geodetic position can be determined by integrating the Geodetic rates for the given time increment [34].

2.4.3 Inertial Measurement Unit Error Model.

Like any measurement devices, the gyro and accelerometer contained in the IMU are imperfect. This results in measurements containing some noise. The noise model for the IMU is used as a basis for the propagation of the EKF covariance. By knowing the behavior

of the gyro and accelerometer noise parameters, the uncertainty in their integrated solution can also be calculated. Both the accelerometer and the gyro contained in the IMU can be modeled in a similar fashion. This paper uses a simplified gyro model from [35] without the static bias, which can be seen in Equation (35):

$$\mathbf{f}_b = \mathbf{g} + \mathbf{b}_g + \mathbf{w}_{gw} \tag{35}$$

The measured specific forces $\mathbf{f}_b$ consist of the true gyro rates $\mathbf{g}$, a First-Order Gauss-Markov (FOGM) bias $\mathbf{b}_g$, and a zero-mean, Gaussian, white noise parameter $\mathbf{w}_{gw}$ defined by the process noise covariance matrix $\mathbf{Q}_{gw}$ where

$$\mathbf{Q}_{gw} = \sigma_{gw}^2 \mathbf{I}_{3\times3} \tag{36}$$

The term σ_{gw}^2 is the variance of $\mathbf{w}_{gw}$. The FOGM gyro bias term is defined as

$$\dot{\mathbf{b}}_g = -\frac{\mathbf{b}_g}{\tau_g} + \mathbf{w}_{gb} \tag{37}$$

where τ_g is the FOGM time constant, and $\mathbf{w}_{gb}$ is a white noise term defined by the process noise covariance matrix $\mathbf{Q}_{gb}$ where

$$\mathbf{Q}_{gb} = \frac{2\sigma_{gb}^2}{\tau_g} \mathbf{I}_{3\times3} \tag{38}$$

The term σ_{gb}^2 is the variance of the gyro bias. The values of the gyro parameters are in Table 2.

The accelerometer is modeled in the same way as the gyro model. The simplified accelerometer model is defined as

$$\boldsymbol{\omega}_{ib}^b = \mathbf{a} + \mathbf{b}_a + \mathbf{w}_{aw} \tag{39}$$

The measured angular rates $\boldsymbol{\omega}_{ib}^b$ consist of the true accelerometer rates $\mathbf{a}$, a FOGM bias $\mathbf{b}_a$, and a zero-mean, Gaussian, white noise parameter $\mathbf{w}_{aw}$ defined by the process noise

18

covariance matrix $\mathbf{Q}_{aw}$ where

$$\mathbf{Q}_{aw} = \sigma_{aw}^2 \mathbf{I}_{3\times3} \tag{40}$$

The term σ_{aw}^2 is the variance of the accelerometer random walk. The FOGM accelerometer bias term is defined as

$$\dot{\mathbf{b}}_a = -\frac{\mathbf{b}_a}{\tau_a} + \mathbf{w}_{ab} \tag{41}$$

where $\dot{\mathbf{b}}_a$ is the derivative of the accelerometer bias, τ_a is the accelerometer FOGM time constant and $\mathbf{w}_{ab}$ is the accelerometer white noise term defined by the process noise covariance matrix $\mathbf{Q}_{ab}$ where

$$\mathbf{Q}_{ab} = \frac{2\sigma_{ab}^2}{\tau_a} \mathbf{I}_{3\times3} \tag{42}$$

The term σ_{ab}^2 is the variance of the accelerometer bias. For both the gyro and accelerometer errors, it is assumed the variance values given in the IMU specifications are the same for all three axes.

2.5 Previous Work

Vision aided navigation and its application in AAR is well researched. Unlike most vision aided navigation, AAR is interested in the relative positioning of two aircraft during the refueling process rather than the absolute position of a single aircraft over a given flight path. The selected research summarized below highlights the progression of vision aided navigation and AAR.

2.5.1 GPS.

The U.S. DoD created the GPS to provide accurate position, velocity, and timing. Initially such accuracy was only specified to 10 m for military users and 100 m for civilian users. Improvements in GPS technology and changes in policy led to a significantly higher

accuracy for all users, including civilians. A user can now obtain theoretical relative position accuracies in the mm range. DGPS and carrier-phase measurements achieve that accuracy by working together. DGPS uses two receivers and subtracts their solutions from one another. This subtraction removes errors common to both receivers such as satellite clock, ephemeris, and atmospheric error. However, DGPS alone will only achieve approximately 0.5 m accuracy without the carrier-phase measurements. Code measurements are the most common method of calculating position in GPS. Code measurements simply calculate the difference between the satellite transmission time and the reception time. Because the signal is traveling at the speed of light, even small differences in time can amount to large errors. To obtain higher levels of accuracy, carrier-phase measurements determine the phase difference between the transmitted signal and the receiver signal. These differences are expressed in cycles which can be translated to distance with wavelength. These wavelengths can be 19 cm or 24 cm depending on which signal is being used. This is a much smaller scale of error leading to more accurate measurements [36].

DGPS accuracy is ideal for relative navigation and AAR. Major Christopher Spinelli at the Air Force Institute of Technology (AFIT) tested DGPS for the relative navigation of two aircraft. Each aircraft was given a GPS receiver. The lead aircraft reference receiver had a combined INS/GPS unit which provided roll, pitch, yaw, and roll rate as well as the unadjusted GPS measurements. The wing aircraft was treated as the mobile receiver referenced from the lead. Maj Spinelli conducted eight separate flight tests with two data sets per test. After 11 hours of test time, he achieved Mean Radial Spherical Error (MRSE) of 3.3 cm, though the total average MRSE for all flight tests was 9.5 cm [13].

While this work demonstrates GPS to be an effective relative navigation tool, there are other factors that prevent it from being the sole source of relative navigation estimation for AAR. First, AAR requires a receiver to fly in close proximity to the tanker from which it is refueling. This results in sky blockage where the proximity of the tanker blocks the receiver's line of sight to the satellites needed for its solution [15]. Second, GPS is susceptible to interference. The Air Force Research Lab (AFRL) specifically targets the use of additional sensors to allow the AAR system to function where GPS is "denied or degraded" [37].

2.5.2 LiDAR.

Once such avenue that has been explored is to use LiDAR. LiDAR uses light or lasers to measure object distance. By shining a laser at the target and measuring the return, a LiDAR system can obtain a distance from the target. Second Lieutenant Joseph Curro at AFIT explored this application. He utilized a scanning LiDAR which projects the lasers in a grid or pattern which allow for a measurement over an area and, thus, calculate more of the aircraft in Figure 3. Lt Curro installed the LiDAR on the receiving vehicle looking up at the representation of the tanker. Utilizing this approach, Lt Curro was able to obtain MRSE of 33-42 cm, dependent on the flight measured [1]. While this level of accuracy is desired, the use of LiDAR requires modification to either all receiver aircraft or all tankers to incorporate the new system. LiDAR is also an active sensor, sending bursts of energy out from the originating aircraft. This research focuses on utilizing capabilities and equipment already present on the KC-46 tanker and existing receiver aircraft while using a more passive approach.
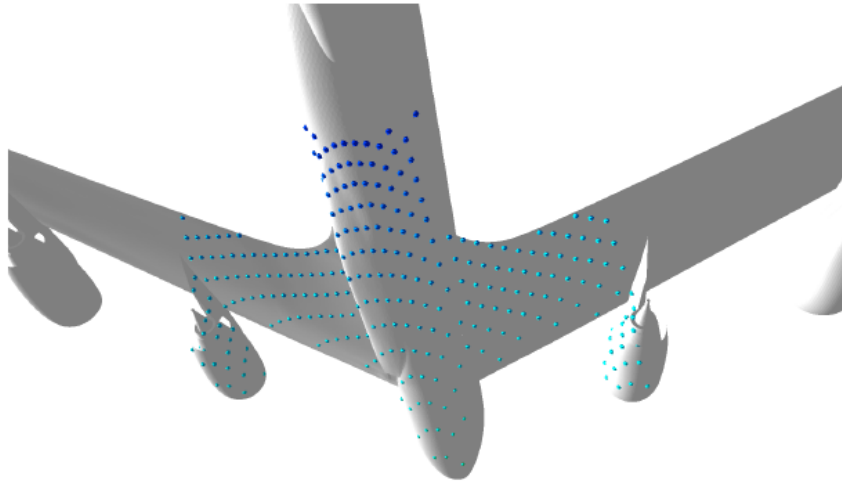
Figure 3. Snapshot of LiDAR scan [1].

2.5.3 Monocular Vision.

Monocular Vision (MV) is another approach used to support or even replace GPS. Unlike LiDAR, MV is entirely passive. MV utilizes a single camera to estimate an object's

location. Mammarella et al. utilize a MV approach to estimate a receiver's position in a refueling scenario. They place a camera on the receiver looking up at the tanker in Figure 4. The camera takes pictures of the tanker and utilizes known algorithms to identify and track features. The algorithm takes the previous estimate, from the MV system or the GPS, and uses it to translate feature pixel coordinates to a 3D estimate of the receiver location. They achieved mean errors of 4-10 cm in the x, y, and z dimensions with a total distance error inside the refueling window of 19.4 cm and a 1-σ of 9.2 cm [2]. Using the same approach with different feature matching algorithms, Fravolini et. al. achieved similar results with total mean error of 15.7 cm and 1-σ of 4.9 cm [3]. Experiments with feature detection and tracking have been done in in numerous other AAR tests and experiments seen in [2, 4, 20, 21, 38–40].
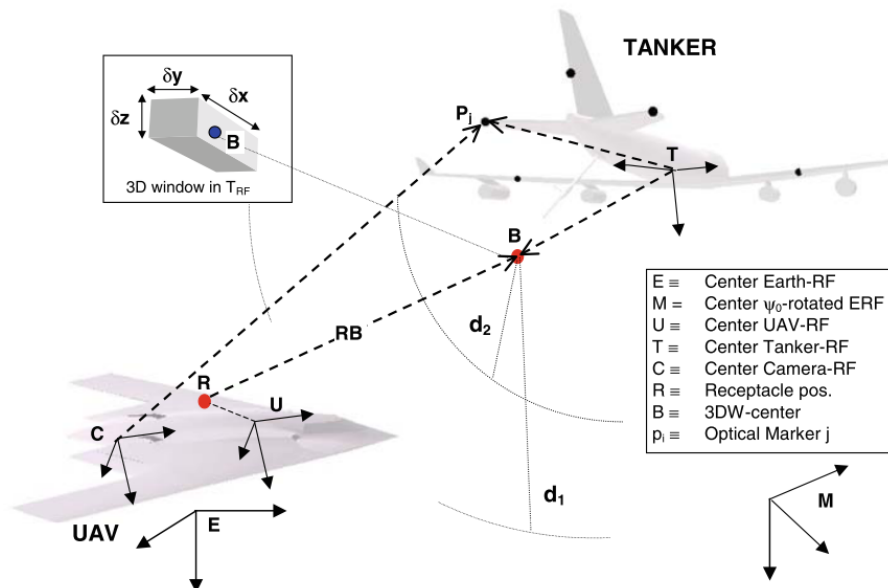
Figure 4. Experimental set up for simulation from [2–7].

There are many different configurations that have been used to test MV estimation. Some experiments add passive optical markers to the viewed aircraft or identify specific features to aid the detection and tracking as seen in [5–7, 16, 20, 23, 41–43]. Instead of markers, some add active beacon configurations. Rather than simply placing a symbol on the viewed aircraft, a form of light is placed where the MV system can see it broadcasting at

specific frequencies and patterns seen in [16, 17, 44, 45]. Ding, Wei, and Wang implemented a beacon-based experiment and achieved accuracies in the mm range within 10 m of the tanker [46]. Variations are also seen in the camera placement with some receiver-based MV systems as in [2–7, 16, 20, 21, 38–43] and some tanker-based as in [22, 23]. Much of the work done with MV has been virtual due to the complexities and cost associated with live flight tests, though there have been multiple experiments that tested MV in a non-virtual setting [38–40]. Howard and Veth implemented a MV approach with predictive rendering in a non-virtual experiment. The mean errors for the entire flight were 54 cm, 26 cm, and 9, cm in the x-, y-, and z-axes at distances of up to 40 m from the tanker [38]. Calhoun, Curro, and Raquet implemented a MV image rendering approach that achieved mean relative error of 17 cm with 9 cm 1-σ in a live flight test [40].

Unfortunately, MV is limited in its capable range and lacks depth information due to its use of a single camera. MV is a close range estimation technique requiring a different measurement method when the receiver is at a greater distances from the tanker [20]. When using the MV approach, a 3D scenario is represented in a single 2D image. To alleviate this shortfall most approaches utilize the known markers or specific features on the aircraft. Markers require modification to existing platforms and specific features are more easily obscured and provide a less robust solution [47]. This research focuses on a similar technique using two cameras. While this does not fix the range shortfall, it does allow the system to obtain the depth lost in a MV system which reduces the need for beacons, markers, or specific features.

2.5.4   Stereo Machine Vision.

Stereo Machine Vision (SMV) incorporates depth information the MV approach could not obtain. While not extensively explored in the AAR realm, SMV has been utilized in terrestrial applications. Nedevschi et al. demonstrated the use of stereo vision for obstacle detection and horizontal ranging in traffic. The SMV system creates a full 3D reconstruction of the scene. 3D points are grouped into objects as it becomes apparent that they share the same trajectory. A KF is used to predict object location to help the algorithm maintain

the same object frame to frame. When a new set of stereo images are taken, the prediction is used as a threshold to search for objects. Objects inside the threshold with similar trajectories are grouped as the same object. Once the object identifies, its new 3D location is used to update the KF. The system was tested in urban, highway, and country road traffic conditions. The final result was less than 10 cm error at a 10 m baseline distance up to 2 m error at 95 m. This scenario is simpler than AAR by effectively removing one dimension and ignoring attitude, but it clearly demonstrates the effectiveness of stereo image position estimation [48]. SMV applications can also be seen in robotics [49, 50] and in many small UAV navigation approaches utilizing SMV as part of a visual odometry algorithm [51–53].

AFIT's Lt Kyle Werner investigated the effectiveness of a stereo positioning approach where only MV had been tested previously. To accomplish this he utilized a simulated AAR environment with an F-15 approaching a tanker fitted with a stereo camera system. He used the stereo vision system to generate disparity maps of the F-15. A speckle filter application was used to remove high-disparity noise by eliminating matches which were not surrounded by enough similar-disparity matches for a given filter window size. Once filtered, the disparity maps were used to generate the point cloud representation of the aircraft seen in Figure 5.

(a) Frontal View   (b) Side View
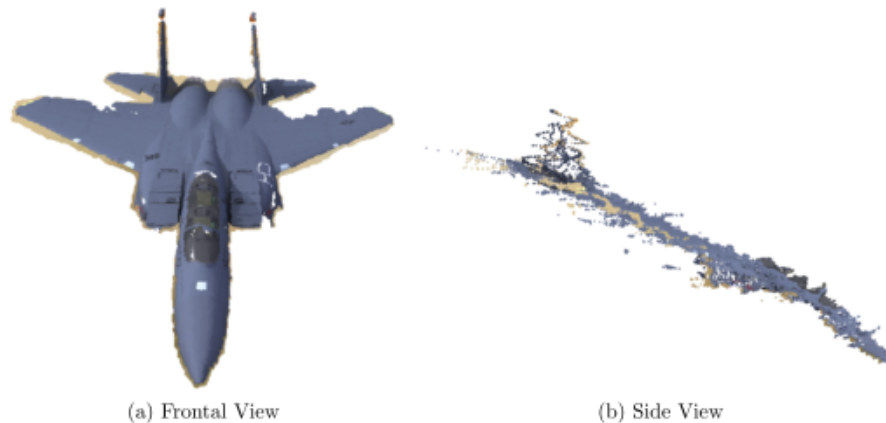
Figure 5. Filtered SMV point cloud generated from stereo image pair [8].

To obtain the desired position and attitude estimates, a variant of the Iterative Closest Point (ICP) algorithm was implemented on the generated point cloud with the stored F-15

model. To ensure the feasibility of a real world application, the algorithm was also tested on a disparity map created from a physical 1:7 scale F-15 model with a stereo vision system. To test the full scenario, stereo estimates were created throughout a 25 second simulation of the F-15 approaching the tanker. The results showed the effectiveness of the stereo estimate for AAR. As the aircraft moved to within 14 m of the tanker, the error in all three axes dropped under 10 cm and all three rotation errors dropped below 1° [8].

AFIT students, Brad Denby and Capt Kevin Colson, have since explored a non-virtual application of SMV to AAR. They utilized the same physical model as Lt Werner. Instead of simply using it to validate their algorithm, they used it to simulate the end of a refueling approach vector. The camera was attached to a guide cable between a large and a small truss with the F-15E model located at the small truss. The camera took stereo image pairs as it slid down the cable to simulate the F15 approaching the tanker [18, 19]. From here their work diverged from each other.

Denby explored three different stereo algorithms focusing on real-time application. He looked at semi-global block matching on a CPU, block matching on a CPU, and block matching on a Graphics Processing Unit (GPU). He utilized the stereo algorithms to generate disparity maps. The disparity maps were then filtered, used to reconstruct the 3D point cloud and then matched to a virtual F15 model to determine the translation and rotation of the F15 and, ultimately, the position estimate. The setup was unable to achieve sufficient accuracy for AAR due to camera calibration issues. Errors were as large as 1.85 m in the 1:7 scaled down environment. However, he was able to achieve near real-time operation with 28.4 Hz operation of the GPU algorithm [19].

Capt Colson explored structure from motion, block matching stereo reprojection, and simulated stereo reprojection to generate point clouds rather than disparity maps. This relies on multiple viewpoints to create a 3D point cloud of the object. Once the point cloud was generated, Capt Colson used a number of different techniques to match the point cloud to the model. He used Principle Component Analysis, Singular Value Decomposition, and ICP with varied numbers of iterations. These processes determined his F15 translation and rotation allowing him to calculate the relative position. Each method of point cloud

generation and point cloud alignment were looked at for speed and accuracy. Like Denby, every approach had relatively high errors in the position, though he was able to identify which algorithms tended to perform more quickly.

2.6 Sensor Fusion

This section explores two of the most common methods used to fuse different sensor types for improved estimation in AAR. One early method was the fuzzy filter, while more recently the EKF has been the method of choice.

2.6.1 Fuzzy Filter.

Research in recent years has shifted from looking at any single sensor to provide the needed data to combinations of sensors or sensor fusion to utilize each sensor's advantages while using other sensors to minimize the disadvantages. Many different sensors are tested but the work outlined below will most commonly use GPS, INS, and vision sensors. The simplest sensor combination is called a fuzzy filter.

A fuzzy filter uses a linear function to adjust the weights of the GPS and MV measurements. When the receiver aircraft is far enough from the tanker to avoid the distortion the filter only uses GPS. As the receiver closes the distance to the tanker, the weights are adjusted until the receiver reaches the point at which the system switches entirely to MV based on the linear distance from the tanker. In one example, 40 m from the tanker began the transition and 23 m from the tanker was completely MV. This system measured the distance from the receiver to the tanker at 20 m with RMS values of 8 cm, 4 cm, and 7 cm in the x, y, and z directions respectively [20]. Because this is a linear combination only, the fuzzy filters combine only two separate measurement types, allowing GPS, MV or a mix. Similar approaches can be seen in [5, 20, 41, 42]. Sensor fusion has since been accomplished primarily with the more robust KF.

2.6.2 Extended Kalman Filter.

An EKF is used in this research instead of a KF due to the nonlinear nature of aircraft, and the majority of the AAR work is done in the virtual realm. Mammarella et al. exploited the simulation environment and experimental setup used in [5] to test the fusion of MV and GPS/INS data through the use of an EKF. The EKF calculated the covariance and gain like the standard KF. However, the EKF propagated the system states and determined the output vector using nonlinear state dynamics equations. The EKF received the command vector, the output vector (calculated from the states), and the number of corners from the Pose Estimation algorithm to ensure the MV measurement was valid. The EKF fusion resulted in errors with two orders of magnitude less than either the GPS or MV solutions individually. The fusion also resulted in errors with an order of magnitude better than the authors' previous work with a fuzzy sensor fusion strategy [4].

Williamson et al. utilized a similar approach by implementing a Global Extended Kalman filter to combine differential carrier-phase GPS, INS, and Electro-Optic (EO) sensors for relative position estimation. However, experimental setup placed the EO sensor on a simulated tanker near where the boom operator is located instead of the receiver. Infrared beacons were placed on the trailing aircraft for the EO system to identify and derive position and attitude. Three different combinations of GPS, INS, and EO were tested to compare functionality. The GPS/INS/EO, INS/EO, and GPS/INS all performed with less than a 10 cm position error in all three axes. The experiment also revealed relative attitude errors of less than $2°$. The determined positions and attitudes were fed the outputs of the relative estimate to the boom controller. Using only the provided data, the boom controller automatically connected to the receiver [22]. The combinations of GPS, INS, and MV utilizing an EKF in a virtual environment for relative navigation are also in [6, 21, 23, 45, 54].

While there is a significant amount of work done in AAR applying EKFs to MV sensor fusion, the same application has not been applied to SMV. However, there have been a number of terrestrial applications utilizing SMV as part of their sensor fusion strategy. SMV is a more popular resource in UAV stereo odometry. Stereo odometry utilizes the

distances to known features to track changes in position between sets of measurements. Rather than measuring the distance from the camera to an object, it tracks the motion of the camera from those object measurements. Kelly, Saripalli, and Sukhatme tested a UAV navigation system combining stereo visual odometry and IMU data in [53]. The Kanade-Lucas-Tomasi algorithm was used to identify feature points which were matched to the corresponding point in the right image with normalized cross-correlation. The 3D positions of the matched feature points were calculated with stereo triangulation. The stereo positioning was combined with the IMU data through the EKF. The EKF took the 100 Hz IMU measurements and combined it with the slower updating visual system. The system clearly demonstrates the effectiveness of combining the stereo vision with the inertial measurements in actual UAV flight. The UAV position estimate tracks the GPS and IMU trajectory for the duration of the entire flight. The final position was only 0.6% off for a total 405 m flight distance utilizing only stereo vision and IMU data [53]. SMV odometry fusion with GPS and/or INS information is also in [51–53, 55, 56].

This background shows the significant amount of work in simulation, AAR, MV, SMV, and sensor fusion. This chapter provides the needed theory used to form the methodology in the next chapter. The purpose is to examine the performance of an EKF combining a stereo vision algorithm with an INS data in a realistic refueling scenario. The trajectory is generated with flight dynamics software to represent an authentic refueling trajectory. The stereo cameras are placed on the simulated tanker facing the approaching receiver below. Utilizing a stereo camera system on the tanker takes advantage of the next generation KC-46 and avoids having to install new camera systems, markers, or beacons on existing platforms. While the primary purpose is to examine the filter performance in a GPS denied environment, this system is able to incorporate the GPS measurements when available. Thus, this simulation looks at measurements both when GPS is available and when it is not. This work presents a novel EKF combining SMV, INS, and optional GPS to provide precise relative navigation throughout an aerial refueling maneuver. The next chapter explains how this research uniquely combines the previously researched theories and techniques in a way that demonstrates an effective AAR solution utilizing and EKF, GPS, INS, and SMV.

III. Methodology

This chapter discusses the process to design an experiment to test the SMV and EKF fusion. Figure 6 depicts the flow of the different components required for the research.
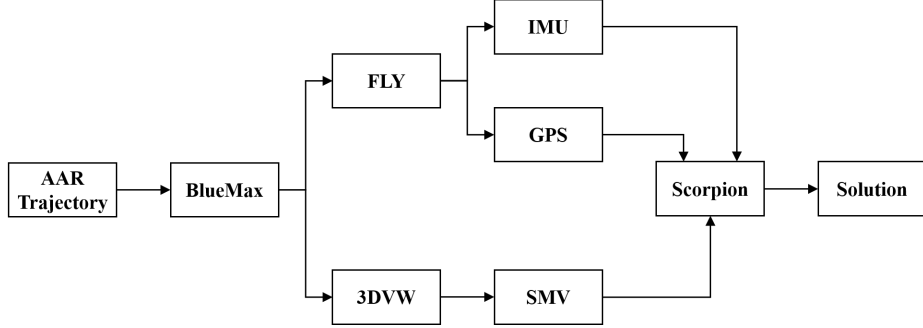
Figure 6. Research Flowchart

3.1   Extended Kalman Filter Design

The EKF used in this paper is an error state EKF, or perturbation filter, implemented within the filtering software Scorpion [57]. The actual states described in Section 2.4.2 are mechanized outside of the EKF while the EKF is used to track the current navigation errors. The relationship between the truth, estimate, and errors are defined by Equations (43), (45) and (46). The Geodetic truth position is defined by

$$\mathbf{p}^w \equiv \bar{\mathbf{p}}^w + \mathbf{A}_n^w \delta \mathbf{p}^n \tag{43}$$

where $\mathbf{p}^w$ is the Geodetic true position, $\bar{\mathbf{p}}^w$ is the a priori solution or INS solution, $\delta \mathbf{p}^n$ is the NED error, and $\mathbf{A}_n^w$ is a matrix that converts from meters to radians defined as

$$\mathbf{A}_n^w = \begin{bmatrix} \frac{1}{R_N + h} & 0 & 0 \\ 0 & \frac{\sec L}{R_E + h} & 0 \\ 0 & 0 & -1 \end{bmatrix} \tag{44}$$

The other two components, velocity and rotation, are defined similarly. The truth velocity is defined by

$$\mathbf{v}^n \equiv \bar{\mathbf{v}}^n + \delta\mathbf{v}^n \tag{45}$$

where $\mathbf{v}^n$ is the true NED velocity, $\bar{\mathbf{v}}^n$ is the a priori solution or INS solution, and $\delta\mathbf{v}^n$ is the NED velocity error [34]. The rotation error is defined by

$$\bar{\mathbf{C}}_b^n \equiv [\mathbf{I} - \mathbf{\Phi}]\,\mathbf{C}_b^n \tag{46}$$

where $\mathbf{C}_b^n$ is the true rotation, $\bar{\mathbf{C}}_b^n$ is the a priori or INS rotation solution, and $\mathbf{\Phi}$ is the skew-symmetric matrix of the tilt errors [34]. According to this definition, the tilt errors are assumed to be small angles. The tilt errors are related to the Psi-Angle model by

$$\boldsymbol{\phi} = \boldsymbol{\psi} + \delta\boldsymbol{\theta} \tag{47}$$

where $\boldsymbol{\phi}$ is the vector form of $\mathbf{\Phi}$, $\boldsymbol{\psi}$ is the vector of errors in the inertial maintained navigation frame or the attitude error, and $\delta\boldsymbol{\theta}$ is the misalignment error of the computed navigation frame against the true navigation frame defined by

$$\delta\dot{\boldsymbol{\theta}} = -\boldsymbol{\omega}_{en}^n \times \delta\boldsymbol{\theta} + \delta\boldsymbol{\omega}_{en}^n \tag{48}$$

where $\delta\dot{\boldsymbol{\theta}}$ is the derivative of the misalignment error, $\boldsymbol{\omega}_{en}^n$ is the rotation of the NED frame to the earth, also called the transport rate, and $\delta\boldsymbol{\omega}_{en}^n$ is the error in the transport rate [58,59].

3.1.1 Pinson 15 Model.

This filter instead uses a error state model, identified in this research as the Pinson 15 error state model. Unlike the traditional EKF described in Section 2.3.2, the Pinson model does not utilize the Jacobian to linearize the state dynamics matrix $\mathbf{F}$. Instead, a set of linearized dynamics are used to relinearized at each point in time as seen in [34]. For this research, the Psi-Angle model dynamics were used and taken from [58,59]. These errors are represented in the computed navigation frame, still referenced with the superscript n. The

position error is derived to be

$$\delta\dot{\mathbf{p}}^n = -\boldsymbol{\omega}_{en}^n \times \delta\mathbf{p}^n + \delta\mathbf{v}^n \tag{49}$$

where $\delta\dot{\mathbf{p}}^n$ is the derivative of the NED position error, $\delta\mathbf{p}^n$ is the NED position error, and $\delta\mathbf{v}^n$ is the NED velocity error. The velocity error is derived to be

$$\delta\dot{\mathbf{v}} = \mathbf{f}^n \times \boldsymbol{\psi} + \mathbf{C}_b^n \delta\mathbf{f}^b - (\boldsymbol{\omega}_{en}^n + 2\boldsymbol{\omega}_{ie}^n) \times \delta\mathbf{v}^n + \delta\mathbf{g}^n \tag{50}$$

where $\delta\dot{\mathbf{v}}$ is the derivative of the velocity error, $\mathbf{f}^n$ is the measured specific forces in the NED frame, $\mathbf{C}_b^n$ is the DCM from the body to the NED frame, $\delta\mathbf{f}^b$ are the errors in the measured specific forces, $\boldsymbol{\omega}_{ie}^n$ is the earth rotation rate in the NED frame, $\delta\mathbf{v}^n$ are the velocity errors in the NED frame, and $\delta\mathbf{g}^n$ is the local gravity vector in the NED frame. The attitude error is derived to be

$$\dot{\boldsymbol{\psi}} = -\boldsymbol{\omega}_{in}^n \times \boldsymbol{\psi} - \mathbf{C}_b^n \delta\boldsymbol{\omega}_{ib}^b \tag{51}$$

where $\dot{\boldsymbol{\psi}}$ is the derivative of the attitude error, $\boldsymbol{\omega}_{in}^n = \boldsymbol{\omega}_{ie}^n + \boldsymbol{\omega}_{en}^n$, and $\delta\boldsymbol{\omega}_{ib}^b$ are the errors in the measured body rates.

The filter model is represented by Equations (52) to (54) and (56). The growth of the error is expressed in its basic state space form by

$$\delta\dot{\mathbf{x}} = \mathbf{F}\delta\mathbf{x} + \mathbf{D}\mathbf{w} \tag{52}$$

where $\delta\dot{\mathbf{x}}$ is the derivative of the error state $\delta\mathbf{x}$, $\mathbf{F}$ is the dynamics matrix, $\mathbf{D}$ is the noise sensitivity matrix defined to be identity, and $\mathbf{w}$ is the noise vector. The Pinson 15 error state $\delta\mathbf{x}$ is defined by

$$\delta\mathbf{x} = \begin{bmatrix} \delta\mathbf{p}^n \\ \delta\mathbf{v}^n \\ \boldsymbol{\psi} \\ \delta\mathbf{b}_a \\ \delta\mathbf{b}_g \end{bmatrix} \tag{53}$$

This differs slightly from typical derivations [21, 22] by also incorporating the accelerometer and gyro bias states, $\delta\mathbf{b}_a$ and $\delta\mathbf{b}_g$ as seen in [25]. This addition of the 6 bias states makes it a Pinson 15 versus the typical Pinson 9 model. The accelerometer bias term $\delta\mathbf{b}_a$ is $\delta\mathbf{f}^b$ from Equation (50) and the gyro bias term $\delta\mathbf{b}_g$ is $\delta\boldsymbol{\omega}_{ib}^b$ from Equation (51). Equations (49) to (51) are used to create the dynamics matrix $\mathbf{F}$ defined as

$$\mathbf{F} = \begin{bmatrix} -\left[\boldsymbol{\omega}_{en}^n\right]_\times & \mathbf{I} & \mathbf{0} & \mathbf{0} & \mathbf{0} \\ \mathbf{G} & -\left[2\boldsymbol{\omega}_{ie}^n + \boldsymbol{\omega}_{en}^n\right]_\times & \left[\mathbf{f}^n\right]_\times & \mathbf{C}_b^n & \mathbf{0} \\ \mathbf{0} & \mathbf{0} & -\left[\boldsymbol{\omega}_{ie}^n + \boldsymbol{\omega}_{en}^n\right]_\times & \mathbf{0} & -\mathbf{C}_b^n \\ \mathbf{0} & \mathbf{0} & \mathbf{0} & -(1/\tau_a)\mathbf{I} & \mathbf{0} \\ \mathbf{0} & \mathbf{0} & \mathbf{0} & \mathbf{0} & -(1/\tau_g)\mathbf{I} \end{bmatrix} \tag{54}$$

where element in this matrix represents a 3x3 matrix of its own. The gravity gradient matrix $\mathbf{G}$ represents the gravity gradient expressed in the NED frame [34]. The NED specific forces $\mathbf{f}^n$ defined as

$$\mathbf{f}^n = \mathbf{C}_b^n \mathbf{f}^b \tag{55}$$

The current nominal estimates of the states are provided to the filter to re-linearize Equation (54) as the filter propagates forward. The noise vector $\mathbf{w}$ is defined by

$$\mathbf{w} = \begin{bmatrix} \mathbf{0} \\ \mathbf{w}_{aw} \\ \mathbf{w}_{gw} \\ \mathbf{w}_{ab} \\ \mathbf{w}_{gb} \end{bmatrix} \tag{56}$$

The process noise matrix associated with the noise vector $\mathbf{w}$ by $\mathrm{E}\left[\mathbf{w}\mathbf{w}^t\right] = \mathbf{Q}$ is defined in

Equation (57).

$$\mathbf{Q} = \begin{bmatrix} \mathbf{0} & \mathbf{0} & \mathbf{0} & \mathbf{0} & \mathbf{0} \\ \mathbf{0} & \sigma_{aw}^2\mathbf{I} & \mathbf{0} & \mathbf{0} & \mathbf{0} \\ \mathbf{0} & \mathbf{0} & \sigma_{gw}^2\mathbf{I} & \mathbf{0} & \mathbf{0} \\ \mathbf{0} & \mathbf{0} & \mathbf{0} & \dfrac{2\sigma_{ab}^2}{\tau_a}\mathbf{I} & \mathbf{0} \\ \mathbf{0} & \mathbf{0} & \mathbf{0} & \mathbf{0} & \dfrac{2\sigma_{gb}^2}{\tau_g}\mathbf{I} \end{bmatrix} \tag{57}$$

Each element in the $\mathbf{Q}$ matrix represents its own 3x3 matrix. The process noise matrix is created with the given IMU specifications The values of the gyro and accelerometer parameters are seen in Table 2. The actual propagation performed in Scorpion uses a discretized noise matrix $\mathbf{Q}_d$ which is defined as [33]:

$$\mathbf{Q}_d(t_{i-i}) = \int_{t_{i-1}}^{t_i} \mathbf{\Phi}(t_i, \tau)\mathbf{D}(\tau)\mathbf{Q}(\tau)\mathbf{D}^T(\tau)\mathbf{\Phi}^T(t_i, \tau)d\tau \tag{58}$$

The state transition matrix $\mathbf{\Phi}$ is defined as

$$\mathbf{\Phi} = e^{\mathbf{F}\Delta t} \tag{59}$$

By multiplying out the identity terms and performing trapezoidal integration Equation (58) can be simplified to

$$\mathbf{Q}_d(t_{i-1}) = \frac{1}{2}\left[\mathbf{\Phi}(t_i, t_{i-1})\mathbf{Q}(t_{i-1})\mathbf{\Phi}^T(t_i, t_{i-1}) + \mathbf{Q}(t_{i-1})\right]\Delta t \tag{60}$$

3.1.2 Relative Navigation Filter.

To appropriately determine relative navigation states and uncertainties, each aircraft has its own set of Pinson 15 states from Equation (53), dynamics from Equation (54), and noise parameters from Equation (57). The two sets of states are combined together into a

single error dynamics equation defined as

$$\begin{bmatrix} \delta\dot{\mathbf{x}}_T \\ \delta\dot{\mathbf{x}}_R \end{bmatrix} = \begin{bmatrix} \mathbf{F}_T & \mathbf{0}_{15\times15} \\ \mathbf{0}_{15\times15} & \mathbf{F}_R \end{bmatrix} \begin{bmatrix} \delta\mathbf{x}_T \\ \delta\mathbf{x}_R \end{bmatrix} + \begin{bmatrix} \mathbf{w}_T \\ \mathbf{w}_R \end{bmatrix} \tag{61}$$

The error state is now defined as the combination of the tanker Pinson 15 error state $\delta\dot{\mathbf{x}}_T$ and the receiver Pinson 15 error state $\delta\dot{\mathbf{x}}_R$. As defined, the tanker state dynamics matrix $\mathbf{F}_T$ and the receiver state dynamics matrix $\mathbf{F}_R$ have no impact on each other. The tanker noise vector $\mathbf{w}_T$ and the receiver noise vector $\mathbf{w}_R$ are also combined into a single vector.

3.2 Measurement Models

This section develops the measurement processors designed to allow Scorpion to incorporate the different measurement types. Processors were design for both SMV and DGPS measurements.

3.2.1 Stereo Vision.

The stereo vision system returns both a position and an attitude or rotation measurement to be fed to the filter. Both measurements are given in the tanker's reference frame. Measurement processors have been designed for both; however, for this application the position measurement is more useful than attitude. With a navigation grade IMU, the small attitude drift results in a more accurate INS attitude estimate than the stereo vision system, so it is not shown here.

The basic stereo algorithm returns the translation and rotation relative to the left camera acquiring the images. The SMV measurement output is converted into the tanker's reference frame, prior to being fed into the filter. Since both aircraft are in close proximity and the errors are tracked in the NED frame, incorporating the measurement only requires calculating the measurement error relative to the INS solution and rotating it into the appropriate frame. The stereo position measurement is defined by

$$\widetilde{\mathbf{p}}_R^{bK} = \mathbf{C}_n^{bK} \mathbf{A}_w^n \left(\mathbf{p}_R^w - \mathbf{p}_T^w\right) + \mathbf{b}_s + \boldsymbol{\nu}_s \tag{62}$$

$\widetilde{\mathbf{p}}_R^{bK}$ is the raw measurement of the receiver position in the tanker frame, $\mathbf{C}_n^{bK}$ is the DCM rotating from the NED frame to the tanker body frame, $\mathbf{A}_w^n$ is the matrix converting from Geodetic radians to NED meters equal to $(\mathbf{A}_n^w)^T$, $\mathbf{p}_R^w$ is the Geodetic position of the receiver, $\mathbf{p}_T^w$ is the Geodetic position of the tanker, $\mathbf{b}_s$ is the SMV measurement FOGM bias, and $\boldsymbol{\nu}_s$ is the SMV measurement noise.

The measurement noise is defined as

$$\boldsymbol{\nu}_p = \begin{bmatrix} \nu_N & \nu_E & \nu_D \end{bmatrix}^T \tag{63}$$

where ν_N, ν_E, and ν_D are zero-mean, white, Gaussian noise in the north, east, and down directions. The σ_N, σ_E, and σ_D accuracy for each measurement is determined experimentally and is explained in Section 3.3.3.3. Error in the stereo measurements can vary depending upon the specific scenario being implemented and non-modeled errors may appear, causing issues in the EKF if not accounted for. In order to best account for uncharacterized errors in the stereo measurement, a FOGM bias $\mathbf{b}_s$ is also incorporated into the measurement equation and defined as

$$\mathbf{b}_s = \begin{bmatrix} b_N & b_E & b_D \end{bmatrix}^T \tag{64}$$

The individual FOGM biases are b_N, b_E, and b_D in the north, east, and down directions respectively. The values used for the FOGM bias τ's and σ's are defined and discussed further in Section 3.3.3.3.3. Inserting Equation (43) into Equation (62) gives

$$\widetilde{\mathbf{p}}_R^{bK} = \mathbf{C}_n^{bK} \left(\Delta\bar{\mathbf{p}}_{RT}^n + \delta\mathbf{p}_R^n - \delta\mathbf{p}_T^n \right) + \mathbf{b}_s + \boldsymbol{\nu}_s \tag{65}$$

$\Delta\bar{\mathbf{p}}_{RT}^n$ is the NED difference between the receiver and tanker INS solutions, $\delta\mathbf{p}_R^n$ is the NED receiver position error, and $\delta\mathbf{p}_T^n$ is the NED tanker position error. Rearranging the terms give the final measurement equation

$$\widetilde{\mathbf{p}}_R^{bK} - \mathbf{C}_n^{bK}\Delta\bar{\mathbf{p}}_{RT}^n = \mathbf{C}_n^{bK} \left(\delta\mathbf{p}_R^n - \delta\mathbf{p}_T^n \right) + \mathbf{b}_s + \boldsymbol{\nu}_s \tag{66}$$

From Equation (66), the measurement matrix $\mathbf{H}_s$ is calculated and defined as

$$\mathbf{H}_s = \begin{bmatrix} -\mathbf{C}_n^{bK} & \mathbf{0} & \mathbf{0} & \mathbf{0} & \mathbf{0} & \mathbf{C}_n^{bK} & \mathbf{0} & \mathbf{0} & \mathbf{0} & \mathbf{0} & \mathbf{I}_{3\times3} \end{bmatrix} \tag{67}$$

Each term is its own 3x3 matrix. The SMV measurement $\mathbf{z}_s$ is defined as

$$\mathbf{z}_s = \widetilde{\mathbf{p}}_R^{bK} - \mathbf{C}_n^{bK}\Delta\bar{\mathbf{p}}_{RT}^n \tag{68}$$

The measurement equation is now rewritten as the linear update

$$\mathbf{z}_s = \mathbf{H}_s \begin{bmatrix} \delta\mathbf{x}_T \\ \delta\mathbf{x}_R \\ \mathbf{b}_s \end{bmatrix} + \boldsymbol{\nu}_s \tag{69}$$

The addition of the measurement bias requires that the states be added to EKF equations defined in Equation (61) resulting in

$$\begin{bmatrix} \delta\dot{\mathbf{x}}_T \\ \delta\dot{\mathbf{x}}_R \\ \delta\dot{\mathbf{b}}_s \end{bmatrix} = \begin{bmatrix} \mathbf{F}_T & \mathbf{0}_{15\times15} & \mathbf{0}_{15\times3} \\ \mathbf{0}_{15\times15} & \mathbf{F}_R & \mathbf{0}_{15\times3} \\ \mathbf{0}_{3\times15} & \mathbf{0}_{3\times15} & \mathbf{F}_s \end{bmatrix} \begin{bmatrix} \delta\mathbf{x}_T \\ \delta\mathbf{x}_R \\ \delta\mathbf{b}_s \end{bmatrix} + \begin{bmatrix} \mathbf{w}_T \\ \mathbf{w}_R \\ \mathbf{w}_s \end{bmatrix} \tag{70}$$

$\delta\dot{\mathbf{b}}_p$ is the derivative of SMV bias error state

$$\mathbf{b}_s = \begin{bmatrix} \mathbf{b}_x & \mathbf{b}_y & \mathbf{b}_z \end{bmatrix}^T \tag{71}$$

where $\mathbf{b}_x$, $\mathbf{b}_y$, and $\mathbf{b}_z$ are the SMV FOGM bias states in the tanker body frame x, y, and z. The FOGM white noise term $\mathbf{w}_s$ is represented by the process noise covariance matrix $\mathbf{Q}_s$ defined as

$$\mathbf{Q}_s = \begin{bmatrix} \dfrac{2\sigma_x^2}{\tau_x}\mathbf{I} & 0 & 0 \\ 0 & \dfrac{2\sigma_y^2}{\tau_y}\mathbf{I} & 0 \\ 0 & 0 & \dfrac{2\sigma_z^2}{\tau_z}\mathbf{I} \end{bmatrix} \tag{72}$$

where σ_x, σ_y, and σ_z are the σ values for the SMV FOGM bias state. The bias state matrix $\mathbf{F}_s$ is defined as

$$\mathbf{F}_s = \begin{bmatrix} -\dfrac{1}{\tau_x} & 0 & 0 \\ 0 & -\dfrac{1}{\tau_y} & 0 \\ 0 & 0 & -\dfrac{1}{\tau_z} \end{bmatrix} \tag{73}$$

τ_x, τ_y, and τ_z are the time constants for the SMV FOGM bias states in the tanker body frame x, y, and z. While the filter tracks the error states of each aircraft separately, this research is primarily interested in the relative position of the two aircraft. In order to display the relative position and uncertainty of the two aircraft, the uncertainty matrix $\mathbf{P}$ must by transformed by the difference of the two aircraft positions. The resulting similarity transformation matrix $\mathbf{A}_p$ is

$$\mathbf{A}_p = \begin{bmatrix} -\mathbf{I} & 0 & 0 & 0 & 0 & \mathbf{I} & 0 & 0 & 0 & 0 & 0 \end{bmatrix} \tag{74}$$

where each term is its own 3x3 matrix. This transformation is applied to the uncertainty matrix by

$$\mathbf{P}_p = \mathbf{A}_p \mathbf{P} \mathbf{A}_p^T \tag{75}$$

yielding $\mathbf{P}_p$, the relative position covariance matrix. The measurements received by this filter are relative measurements only and have little impact on the individual states of each aircraft. It is only by incorporating the cross covariances through the transformation of $\mathbf{P}$ to $\mathbf{P}_{\text{pos}}$ that the filter's effects are seen. Likewise the relative velocity transformation matrix $\mathbf{A}_v$ is

$$\mathbf{A}_v = \begin{bmatrix} 0 & -\mathbf{I} & 0 & 0 & 0 & 0 & \mathbf{I} & 0 & 0 & 0 & 0 \end{bmatrix} \tag{76}$$

the relative velocity covariance matrix $\mathbf{P}_v$ is

$$\mathbf{P}_v = \mathbf{A}_v \mathbf{P} \mathbf{A}_v^T \tag{77}$$

37

the relative attitude transformation matrix $\mathbf{A}_a$ is

$$\mathbf{A}_a = \begin{bmatrix} \mathbf{0} & \mathbf{0} & -\mathbf{I} & \mathbf{0} & \mathbf{0} & \mathbf{0} & \mathbf{0} & \mathbf{I} & \mathbf{0} & \mathbf{0} & \mathbf{0} \end{bmatrix} \tag{78}$$

and the relative attitude covariance matrix $\mathbf{P}_a$ is

$$\mathbf{P}_a = \mathbf{A}_a \mathbf{P} \mathbf{A}_a^T \tag{79}$$

3.2.2 Differential Global Positioning System.

The DGPS measurements are modeled in the Geodetic frame giving

$$\widetilde{\mathbf{p}}_{TR}^w = (\mathbf{p}_R^w - \mathbf{p}_T^w) + \boldsymbol{\nu}_d \tag{80}$$

$\widetilde{\mathbf{p}}_{TR}^w$ is the measured position of the receiver relative to the tanker in Geodetic radians and $\boldsymbol{\nu}_d$ is the zero-mean Gaussian DGPS measurement noise. Converting both sides into NED results in

$$\mathbf{A}_w^n \widetilde{\mathbf{p}}_{TR}^w = \mathbf{A}_w^n (\mathbf{p}_R^w - \mathbf{p}_T^w) + \mathbf{A}_w^n \boldsymbol{\nu}_d \tag{81}$$

$\boldsymbol{\sigma}_d$ is 2 cm in all three axes. Equation (81) further simplifies to

$$\mathbf{A}_w^n (\widetilde{\mathbf{p}}_{TR}^w - \Delta \bar{\mathbf{p}}_{RT}^w) = (\delta \mathbf{p}_R^n - \delta \mathbf{p}_T^n) + \mathbf{A}_w^n \boldsymbol{\nu}_d \tag{82}$$

$\Delta \bar{\mathbf{p}}_{RT}^w$ is the Geodetic difference between the receiver and tanker INS solutions. From Equation (82), the DGPS measurement matrix $\mathbf{H}_d$ is calculated and defined as

$$\mathbf{H}_d = \begin{bmatrix} -\mathbf{I} & \mathbf{0} & \mathbf{0} & \mathbf{0} & \mathbf{0} & \mathbf{I} & \mathbf{0} & \mathbf{0} & \mathbf{0} & \mathbf{0} & \mathbf{0} \end{bmatrix} \tag{83}$$

where each term is its own 3x3 matrix. The DGPS measurement $\mathbf{z}_d$ is defined in Equation (84):

$$\mathbf{z}_d = \mathbf{A}_w^n (\widetilde{\mathbf{p}}_{TR}^w - \Delta \bar{\mathbf{p}}_{RT}^w) \tag{84}$$

The measurement equation is now rewritten as the linear update

$$\mathbf{z}_d = \mathbf{H}_d \begin{bmatrix} \delta \mathbf{x}_T \\ \delta \mathbf{x}_R \\ \mathbf{b}_s \end{bmatrix} + \boldsymbol{\nu}_d \tag{85}$$

3.3 Building the Simulation

This section describes the steps necessary to generate the synthetic data required to implement the filter. Because there is no real-world data available for SMV AAR, this experiment is entirely simulated. The following subsections will explain the process used to create the simulated flight path, 3DVW, and the IMU, GPS, and SMV sensor data.

3.3.1 Simulated Flight Path.

The flight path is simulated specifically to mimic a real refueling maneuver with authentic aircraft flight dynamics. To achieve this end, the flight path is generated using BlueMax6 flight dynamics software [30]. Using existing profiles, the tanker is simulated with a model similar in size and specifications to existing tanker aircraft and the receiver is modeled as a smaller aircraft similar in size to a typical receiver. The KC-135 is used for the tanker and the F15 is used for the receiver. The flight path for the aircraft adheres to the AAR requirements for relative positions and velocities. This section is in ft and n.m. for the sake of comparison to the AAR requirements. Both aircraft are flying due north with the receiver 1.2 nm behind and 1000 ft below the contact point. The simulated contact point is 29.18 m behind and 13.53 m below the tanker center. Figure 7 shows the receiver approach within 2000 ft. The vertical jumps represent points where the receiver stops to stabilize. This is a byproduct of BlueMax which can overshoot an altitude, requiring a moment for the receiver to settle. In simulation this is not an extreme motion and the flight appears smooth. Figure 8 is a plot of the relative velocity between the two aircraft over the same distance. By the time the receiver is approaching contact, its relative velocity under 1 ft/s.
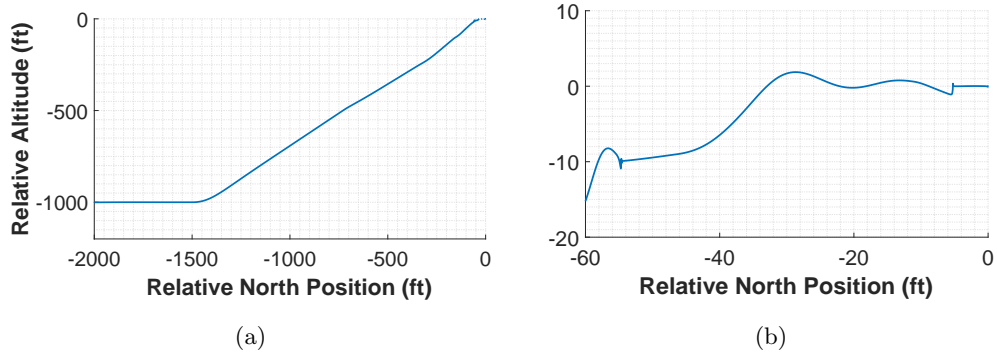
Figure 7. Relative Altitude Plotted Against Relative Horizontal Position for the Last a) 2000 ft and b) 60 ft
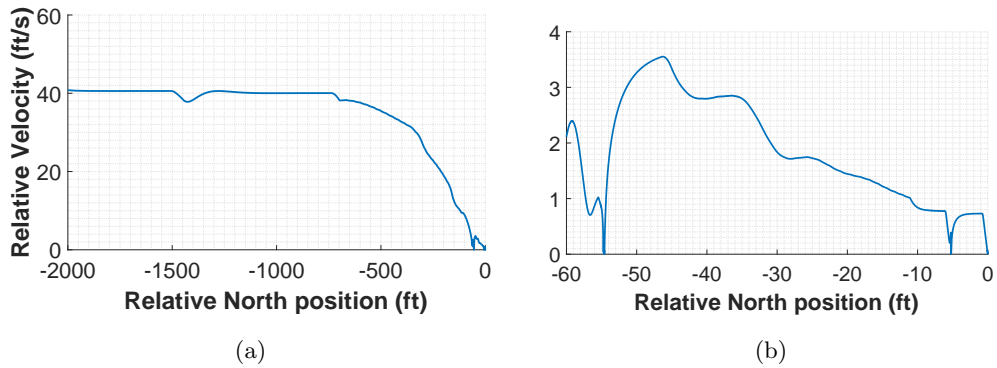
Figure 8. Relative Velocity Plotted Against Relative Horizontal Position for the Last a) 2000 ft and b) 60 ft

3.3.2 Simulation Environment.

This paper uses a 3DVW developed by Dr. Scott Nykl [26–28] in order to best simulate the stereo vision system.

3.3.2.1 Aircraft Models.

Each aircraft is modeled in the simulated environment in a geometrically accurate manner. To utilize existing models, the tanker is modeled as a KC-46 and the receiver is modeled as a C12. These differ from the models used in the flight path generation due to model availability in the flight simulation software. These models are sufficient for performing the experiment. The flight path is still representative of a possible AAR flight path even if the

40

dynamics of the aircraft are slightly altered. The C12 is used for the receiver model for two primary reasons. First, ICP requires a point cloud model to match. Second, a real-life flight test to obtain real-world data for the the SMV system will be performed by Captain Stuart in Fall of 2017 using a C12 as the receiver aircraft. Both the KC-46 and the C12 are represented in the virtual world according to near real-life dimensions as seen in Figure 1. To mimic refueling flight accurately, a simulated refueling boom is toggled on or off and placed at the rear of the tanker close to where a boom is located.
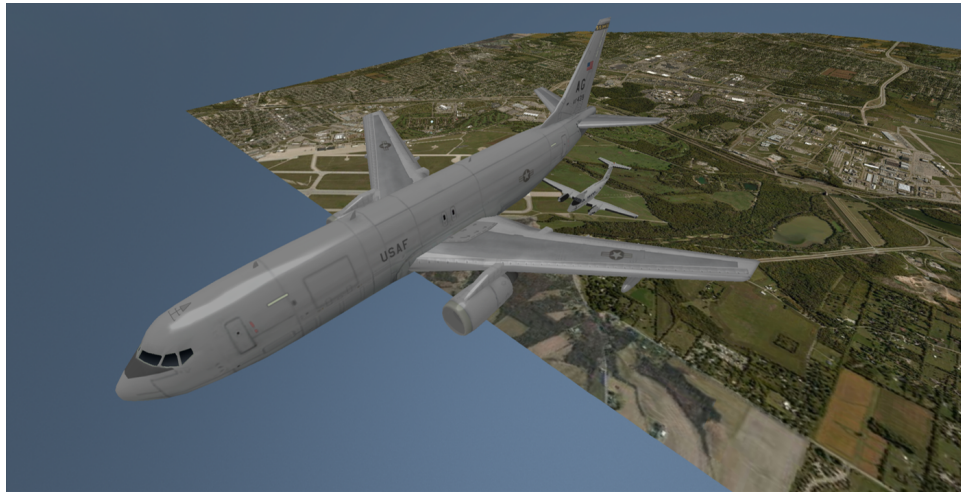
Figure 9. View of the 3DVW Showing the Tanker and the Receiver in Formation Flight Above Terrain Generated from Satellite Imagery

3.3.2.2 World Model.

Implementing the research in this virtual world provides numerous avenues for studying SMV. The 3DVW naturally operates in a open space navigation frame but is also capable of incorporating flight paths generated with a world model. The open space navigation frame allows the receiver to be placed anywhere in the world relative to the tanker. This allows a more general characterization of the stereo algorithm behavior. However, the 3DVW can also take two separate WGS-84 flight paths and place them in the virtual world with the correct relative motion between them. In order to aid in simulation observability, one aircraft is held stationary while the other is placed in an accurate relative position. The tanker origin is also treated as the origin of the 3DVW for each time epoch. From the

perspective of the 3DVW, the tanker is stationary while other objects move around it.

The 3DVW can also include terrain profiles. Like the tanker, the terrain is stationary though it rotates according to the tanker's motion around the earth. This ensures the correct relative position to the tanker for its altitude and orientation to the surface. Figure 9 shows the aircraft in flight above a terrain profile. The terrain also incorporates local elevation data from [60] to provide depth to the satellite imagery [61]. The aircraft can be placed at any altitude above this terrain, though for this simulation the tanker is placed at 3900 m. The terrain is large enough for the entire view of the camera system to fall within the terrain in Figure 12. In 3DVW the absolute truth for instant error measurement is always given. This ensures that the measurements and their times line up. The real system has transmission delays making it a challenge to precisely timestamp images and measurements. Unfortunately, because the terrain is stationary, any terrain characteristics affecting the algorithm will be present for the entire simulation. This affect is observed clearly in one of the original simulations. The aircraft, placed at 2000 m, identified a building with a parallel roof structure by the SMV algorithm as a set of features much closer to the aircraft. Figure 10 shows this from two different angles.

(a) Points on Roof   (b) Points Near Aircraft

Figure 10. Example of Ground Features Causing Point Point Cloud Error. In a), the 3D Points are Aligned with the Roof Structure. However, in b) the Points are Reconstructed Closer to the Stereo Cameras and the Receiver

While point cloud filtering through a median filter helps to ignore erroneous 3D points, these features appear close enough to the receiver point cloud to be missed by the filter. The resulting ICP error is seen in Figure 11. The presence of the points cause a sharp increase in the position error which gradually decreases as the aircraft progresses.
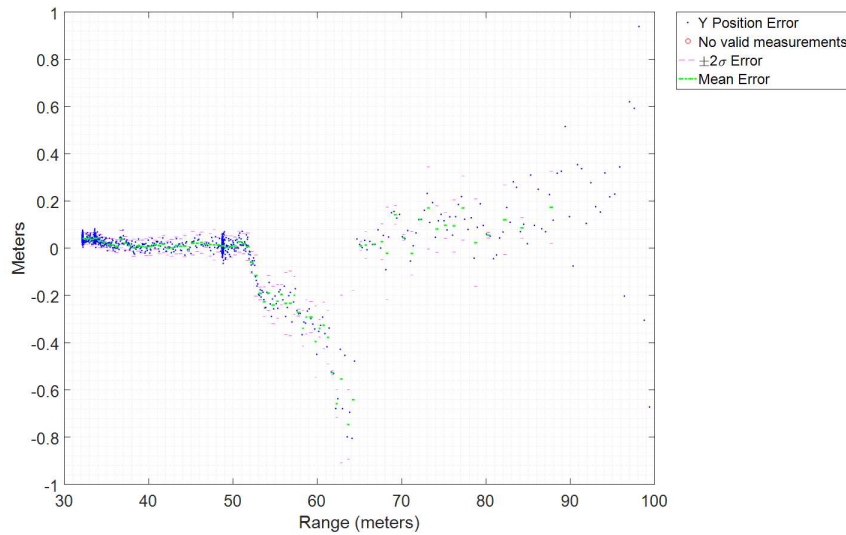
Figure 11. ICP Position Translation Error Caused by Ground Features

As the aircraft moves above the terrain, the feature, causing it to line up geometrically at the precise moment, quickly fades. Higher altitudes and blurring from the fixed focal length camera may potentially help prevent similar errors in operation.

3.3.2.3 Stereo Camera System Model.

The key capability in the 3DVW is the ability to simulate the stereo imagery. This allows for the implementation of the SMV algorithm. SMV parameters, including field of view and intrinsic and extrinsic camera calibration, generate high fidelity synthetic SMV data. This approximates the stereo parameters of the KC-46 vision system offering these images in a deterministic simulation environment. A pair of virtual cameras are affixed to the tanker just behind the location of the boom in Figure 1. The cameras are oriented at 30 degree downward angle from the tanker xy-plane. A sample stereo pair in this simulation environment are captured in Figure 12.

(a) Left Image   (b) Right Image

Figure 12. A Stereo Image Pair Collected by the Virtual Stereo Cameras

The Horizontal Field of View (HFOV), focal length, resolution, and baseline parameters for the stereo camera system are in Section 3.3.2.3.

Table 1. Stereo Camera Parameters

Focal Length	16.44	mm
HFOV	56	deg
Resolution	1024x768	pixels
Baseline	0.5	m

The cameras' orientations and fields of view are in Figure 13. The red lines represent the edge of the cameras' field of view as they extend out. The blue and green lines box in the image captured by the camera.
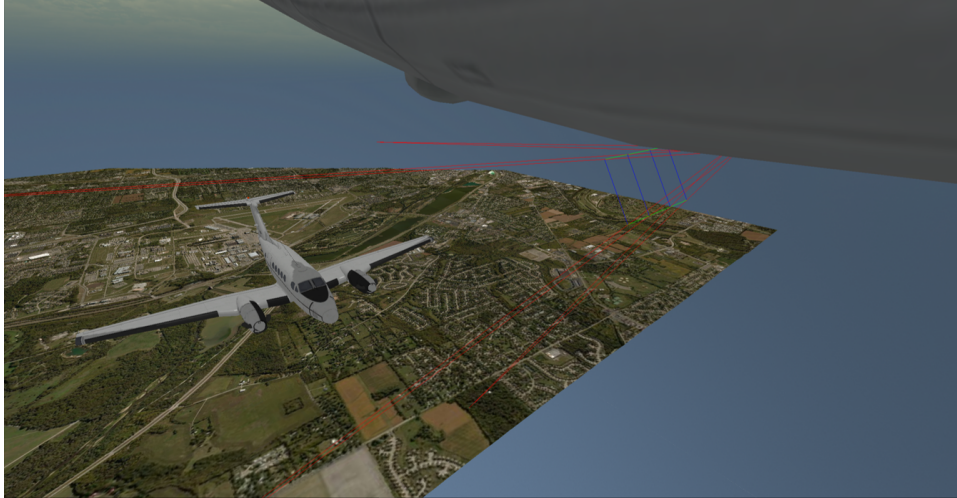
Figure 13. Capture from the 3DVW Showing the Camera Field of View

3.3.3 Simulated Sensor Data.

Beside the stereo vision measurements, the simulated sensor data used in this research is generated through the use of FLY. FLY is an in-house software developed by the AFIT Autonomy and Navigation Technology (ANT) center to generate different forms of simulated sensor data such as IMU, INS, GPS, position, and velocity measurements with realistic errors [62]. Where possible, simulated measurements' specifications are based on the Geodetics RelNAV system which will be used in future AFIT flight tests [63].

3.3.3.1 Inertial Measurement Unit.

In order to generate simulated IMU data, FLY requires the truth Geodetic data for each aircraft and the corresponding accelerometer and gyro parameters shown in Table 2, respectively.

Table 2. IMU Parameters

	Bias 1-σ	Bias τ	Random Walk 1-σ
Accelerometer	0.05 mg	3600 s	0.07 (m/s)/$\sqrt{\text{hr}}$
Gyro	0.05°/hr	3600 s	0.012°/$\sqrt{\text{hr}}$

The IMU specifications are taken from the specifications for the KVH 1750 Laser Ring

Gyro used by the Geodetics system [64]. With the truth values and the IMU specifications, FLY generates the simulated Δv and $\Delta \theta$ values with the specified error characteristics [62]. The IMUs are assumed to be colocated and aligned with the body frame of the aircraft in which they reside. The results of the IMU simulation will be discussed later in Section 4.1 and in Figures 24 to 26

3.3.3.2   DGPS.

The DGPS simulated measurements are also generated using FLY [62]. Like the IMUs, the accuracy for the DGPS are taken from the Geodetics system which lists accuracy of 2 cm for its DGPS measurements [63]. To generate the specific relative DGPS measurements, FLY added 2 cm of Gaussian random noise to the receiver position truth data in Geodetic coordinates. The tanker truth Geodetic data is subtracted from the noisy receiver data resulting in a relative measurement in radians with 2 cm accuracy. Figure 14 shows the plot of the DGPS simulated measurement error. The DGPS measurements were simulated 500 times. The resulting mean oscillates at an error of 0 cm while the ensemble 1-σ value is at the expected 2 cm line. The RMSE of the x-, y-, and z-axes are 2.00 cm, 2.02 cm, and 1.99 cm respectively.
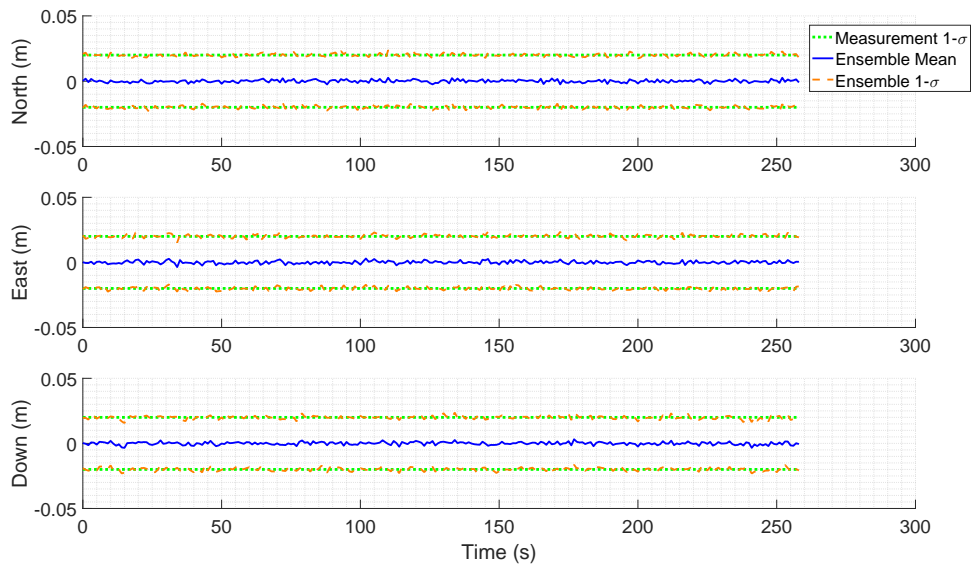
Figure 14. DGPS Measurement Error Mean, Ensemble 1-σ, and Expected Measurement 1-σ

3.3.3.3 Stereo Vision.

This section explains the work accomplished to obtain SMV measurements. The first section explains the basics of the algorithm used to generate measurements. The second section explains the process used to characterize and model the measurements.

3.3.3.3.1 Algorithms. The stereo vision measurements are generated using the 3DVWs simulated stereo cameras and processed with OpenCV [65] and Matlab [66] from the works of 2nd Lieutenant Parsons and Captain Stuart [28,67]. Within the 3DVW, each stereo pair is used by OpenCV to create a disparity map. The disparity map was generated with OpenCV's StereoBM function using numDisparities value of 48, and a Sum of Absolute Differences (SAD) window size of 9. A speckle filter with a maximum speckle size of 144 and a maximum distance between neighbors of 4 was used to reduce noise in the disparity map. The ideal camera reprojection matrix $\mathbf{Q}_{stereo}$ is

$$\mathbf{Q}_{\text{stereo}} = \begin{bmatrix} 1 & 0 & 0 & -5.115\text{e}2 \\ 0 & 1 & 0 & -3.835\text{e}2 \\ 0 & 0 & 0 & 9.629\text{e}2 \\ 0 & 0 & 2.000\text{e}{-}3 & 0 \end{bmatrix} \tag{86}$$

The reprojection matrix is used to create the 3D point cloud, which were were passed to Matlab to be processed. The point clouds were run through a median filter. The filter eliminated any points that were greater than 20 m total distance from the median point in the cloud and greater than 12 m, 12 m, and 2.4 m away from the median in the x, y, and z of the sensed point cloud frame. ICP was conducted with Matlab's pcregrigid function [68]. Subsequently, an implementation of ICP is used to obtain the position measurements between the sensed point cloud and the point cloud model colocated with the tanker [29,69]. The median point was used to seed the pcregrigid function with 20 maximum iterations and with the point to point minimization function. The pcregrigid function was iterated once, seeding it with the previously calculated translation. Once ICP was completed, the position estimate was rotated into the Tanker's body frame [29,69].

3.3.3.3.2   Characterization.   To use the measurements in the EKF, the noise covariance matrix, **R**, is required. Utilizing the 3DVW, the error of the stereo vision implementation is characterized by randomly placing the aircraft in the cameras' field of view at specific ranges and calculating the statistics of the error. The aircraft is characterized every 0.5 m from 30 m to 250 m away from the tanker. At each range, the aircraft was randomly placed 200 times between an elevation of 11 degrees and 34 degrees and an azimuth of -2 and 2 degrees while maintaining the set range. Elevation is defined as the angle down from the tanker xy-plane and the azimuth is the angle from the tanker xz-plane. These boundaries are determined based on the projected flight path of the aircraft. At each iteration, the aircraft is also placed at a random attitude with a max roll, pitch, and yaw of 1, 3, and 1 degrees respectively. These values are also determined by the anticipated flight path which contains very small aircraft attitude deviations. This random sampling was performed with and without a terrain background. The results combine in order to obtain a more general characterization. The errors in the position estimates by the stereo algorithm for the 200 realizations at each range were matched to a normal fit to provide the mean and covariance, as shown in Figure 15.
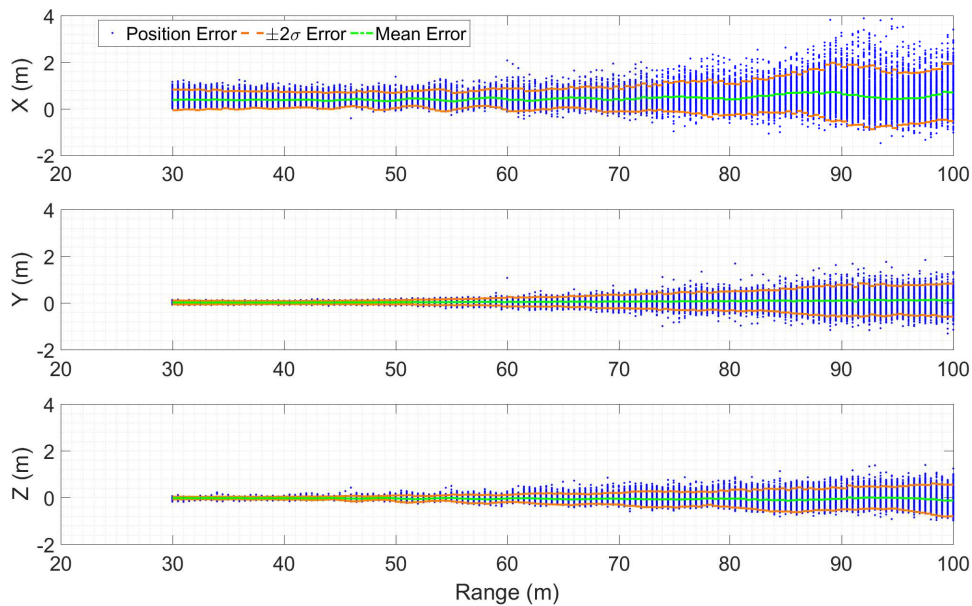
Figure 15. Combined Terrain and No Terrain Characterization of the SMV Measurement Error

48

3.3.3.3.3   Final Measurements. The characterization in Paragraph 3.3.3.3.2 does the final processing on the measurement according to one of two cases. In both cases measurements are only used within 100 m of the tanker. While the SMV system obtains measurements as far out as 250 m, it is more important to look at measurements when the two aircraft are closer. Incorporating the measurements beyond this distance makes it harder to characterize them and thus harder to effectively incorporate them into the filter. The accuracy associated with each measurement does not change between cases since it is based on the standard deviation of the characterization. However,the measurement itself is different for each case.

Case 1. In Case 1, bias corrections are not applied to the incoming SMV measurements. It is intended to be the general case applicable to more than this specific simulation. It assumes the characterization is only a general characterization and is unable to correct for the specific bias present in the measurement. Thus the measurements are taken as the stereo algorithm calculates them. The result is in Figure 16. Ideally, measurements given to a filter are zero-mean. However, with no correction, the measurement error is not zero-mean. This bias is evident in the x-axis which aligns most with the camera z-axis or depth. The depth is the hardest dimension for the camera to estimate so the greatest error should reflect along the x-axis.
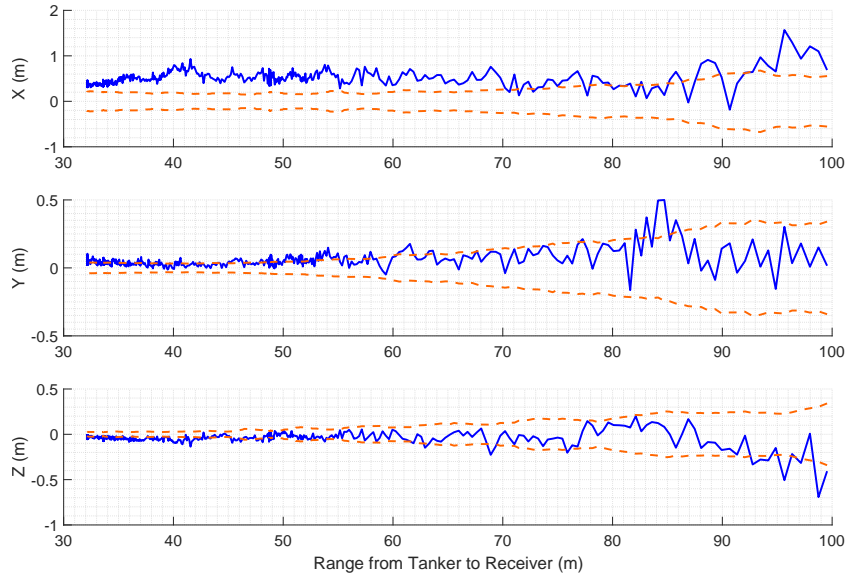
Figure 16. SMV Measurement Error with No Bias Correction. The 1-σ Calculated from the Error Characterization is Plotted over the Uncorrected Measurements.

The specific case also impacts the filter design. The FOGM bias built into the EKF parameters change depending on how measurements are processed. Since Case 1 is a general case, the FOGM bias is designed to incorporate a larger bias in the SMV measurements. The σ and τ values for each axis are determined from the characterized mean error from Figure 15. Figure 17 shows the 2nd order polynomial fit of the characterized mean.
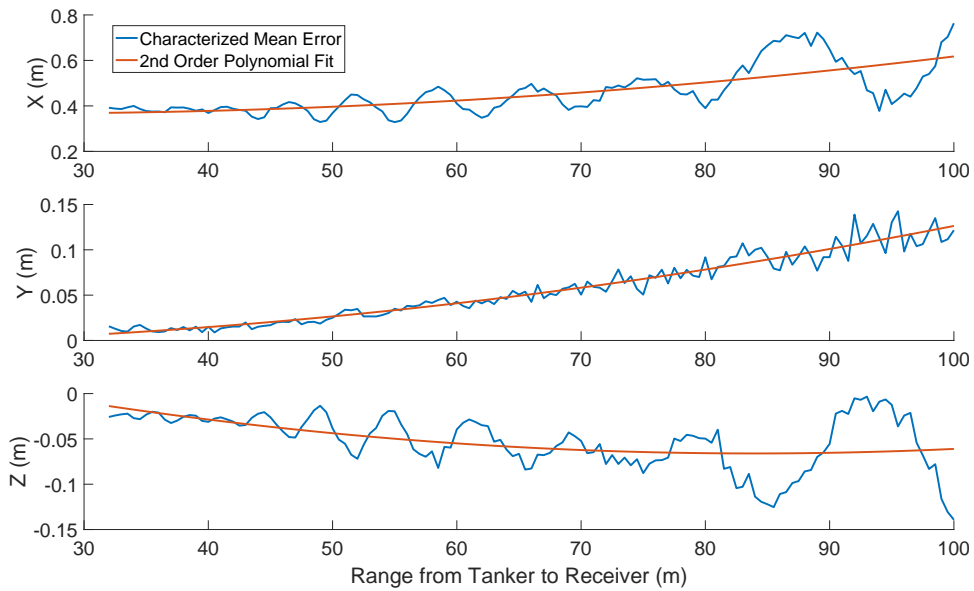
Figure 17. Plot of the Mean SMV Error with the 2nd Order Polynomial Best Fit

The polynomial fit is a function of the range between the tanker and the receiver. The mean error equations follow the form

$$\mu_e = ar^2 + br + c \tag{87}$$

μ_e is the mean error, r is the range between the tanker and the receiver and a, b, and c are the coefficients shown in Table 3 for the x-, y-, and z-axes, respectively.

Table 3. Characterized Mean Error Fit Function Parameters

	a	b	c
X	4.312e−5	−2.046e−3	3.909e−1
Y	1.368e−5	−5.534e−5	−4.909e−3
Z	1.937e−5	−3.252e−3	7.046e−2

Because no correction is done on the SMV measurements in this case, the mean error fit is also used as the FOGM bias 1-σ value. The standard deviation of the FOGM bias is calculated the same as Equation (87):

$$\sigma_b = ar^2 + br + c \tag{88}$$

where σ_b is the standard deviation of the FOGM bias. The parameters for the Case 1 σ polynomial functions are in Table 4.

In order to properly model the FOGM bias, the associated time constant must also be determined. However, the SMV bias is not correlated in time but is based on the range between the tanker and the receiver. To determine the time constant for each axis, a new function is defined as

$$\tau = \frac{\tau_r}{\bar{v}} \tag{89}$$

where τ is the time constant, τ_r is the range constant, and $\bar{v}$ is the current estimated relative velocity. This is developed from the concept that the time constant represents how long it will take two time-based processes to decorrelate. This describes how much the distance

51

between the receiver and the tanker needs to change before the bias value decorrelates. Dividing this range constant by the current velocity then calculates how long it will take the bias to decorrelate at the current velocity.

This effectively allows the range constant to be represented as a time constant in the time-based KF. The range constant is determined by performing an autocorrelation on the characterized mean errors in Figure 17. The resulting normalized autocorrelation functions and range constants are in Figure 18. The range constants are also in Table 3. The autocorrelation was plotted against half meter steps. Mistakenly, these were applied as full meter steps resulting in time constants twice as large as calculated from the autocorrelation function. It was determined that the larger time constant resulted in lower filter error and the larger value was used.
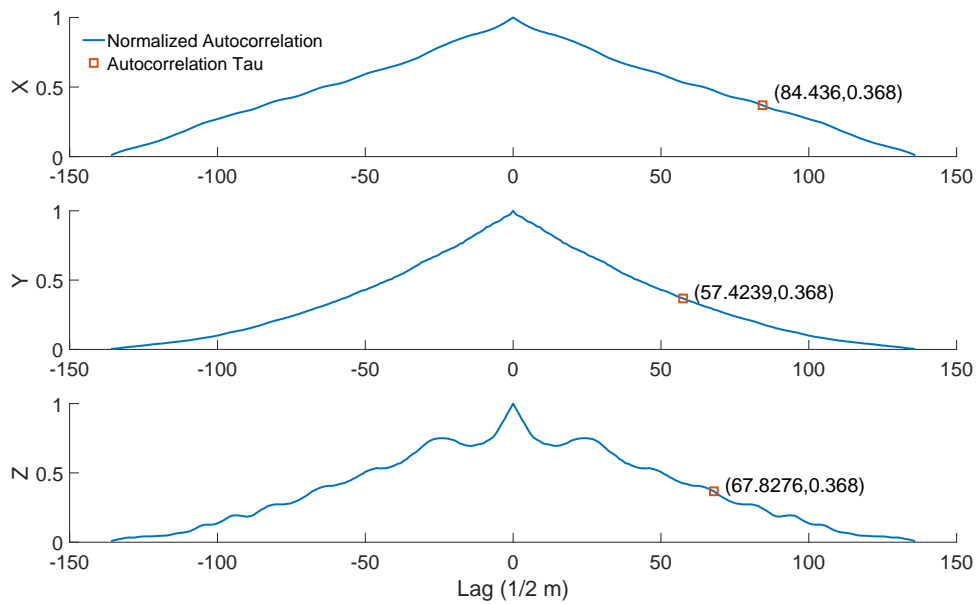
Figure 18. Plot of the Case 1 autocorrelation function of the Characterized Error Bias Mean with Calculated Range Constant

Table 4. Case 1 FOGM polynomial parameters and range constants

	a	b	c	τ_r
X	4.312e−5	−2.046e−3	3.909e−1	84.436
Y	1.368e−5	−5.534e−5	−4.909e−3	57.4239
Z	1.937e−5	−3.252e−3	7.046e−2	67.8276

Case 2. In Case 2, bias corrections are applied to the incoming SMV measurements. Case 2 is intended to be the specific case applicable to this simulation. It assumes the characterization is well known for this scenario and is able to use the characterized mean to adjust the measurements. The polynomial fit from Figure 17 and table 3 is used to correct each measurement as a model of the bias.

To correct the SMV measurements, the SMV measurement is used to calculate the range. This range is then fed to each of the polynomial fit equations to generate the characterized mean error at that distance. The characterized mean error is then subtracted from the SMV measurement to obtain the corrected measurement. Applying this correction to the same measurements from Figure 16 results in the errors seen in Figure 19.
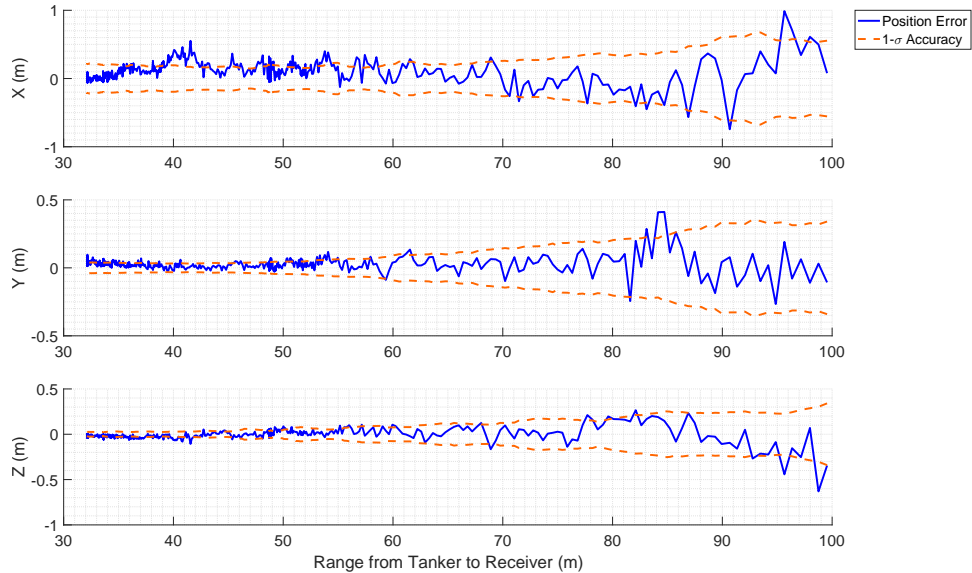
Figure 19. SMV Measurement Error with Bias Correction. The 1-σ Calculated from the Error Characterization is Plotted over the Corrected Measurements

The corrected measurements have a smaller bias as evidenced by the Position Error Mean line dropping much closer to zero. However, some bias still remains. Table 5 shows the mean error for both cases.

Table 5. SMV Mean Error within 100 m

	X	Y	Z
Case 1	46.91 cm	4.987 cm	-3.612 cm
Case 2	7.836 cm	2.926 cm	-0.6155 cm

There is a clear improvement when the measurements are corrected based on the error characterization. It is important to note that the characterization used is specific to this simulation. Different approaches, aircraft, and conditions may affect the SMV behavior, stressing the importance of looking at both cases.

The remainder is used to determine the FOGM bias parameters. Figure 20 shows the characterized mean error after the modeled mean is removed.
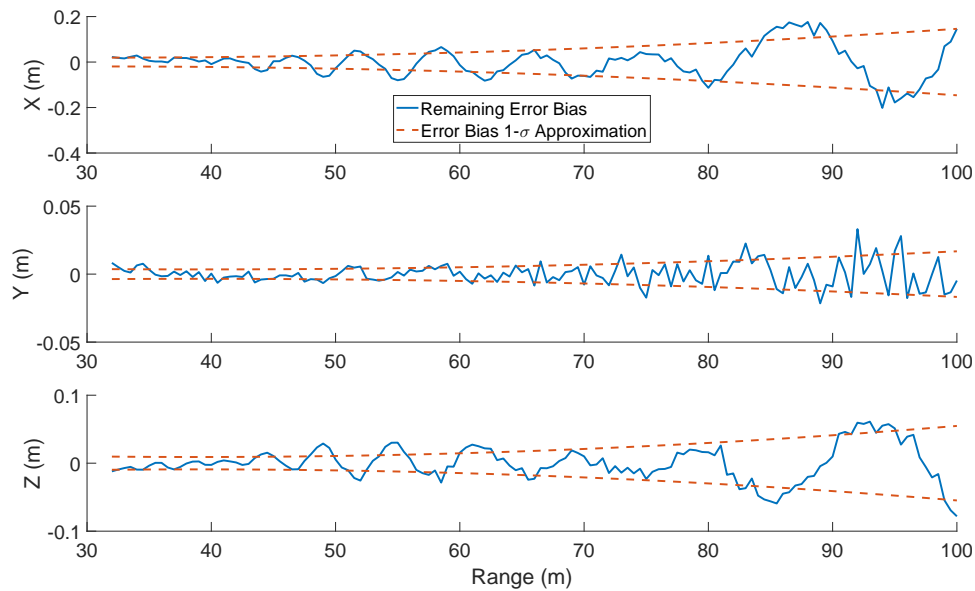
Figure 20. Plot of the Remaining Characterized Error Bias after the Modeled Mean Error is Removed. The 1-σ Approximation to be used for the FOGM Bias is also Plotted over the Remaining Error Bias

The plots appear to oscillate about zero with the error growing as the range between the aircraft increases. Another 2nd order polynomial fit is generated for the remaining

characterized stereo error in each axis. Approximately 68% of the remaining error bias falls within the bounds of the 1-σ approximation. The 2nd order polynomial parameters for calculating the FOGM σ values can be seen in Table 6. As discussed in Section 3.3.3.3.3, Filter tuning determined a more conservative bias σ estimate. The more conservative 3-σ was used instead. A minimum FOGM σ was set to 5 cm to account for additional uncharacterized biases.

The same process is used to determine the range constant for Case 2. The autocorrelation function and range constants are in Figure 21. The range constants are also in Table 6. Like Case 1, the range constant is twice the calculated size.
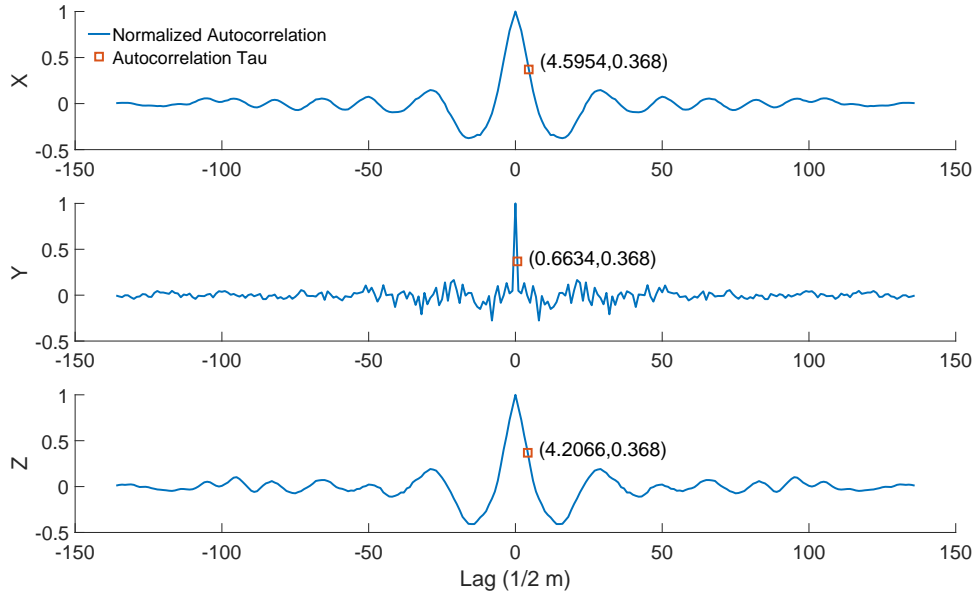
Figure 21. Plot of the Case 2 Autocorrelation Function of the Characterized Error Bias once the Modeled Error Bias has been Removed with Calculated Range Constant

Table 6. Case 2 FOGM polynomial parameters and range constants

	a	b	c	τ_r
X	2.642e−5	−1.624e−3	4.432e−2	4.5954
Y	3.593e−6	−2.812e−4	8.970e−3	0.6634
Z	1.224e−5	−9.520e−4	2.760e−2	4.2066

3.3.4   Filter Software.

The filter is implemented using Scorpion [57]. Scorpion is a soon-to-be-released modular environment for constructing and running filters developed by the AFIT ANT Center. The data flow in Scorpion is seen in Figure 22. The simulated IMU data is fed to the Scorpion mechanization function producing the INS solution. This estimate is given to the EKF to use as a linearization point. The state dynamics defined in Section 3.1 and the measurement processors defined in Sections 3.3.3.2 and 3.3.3.3 are both fed to the EKF initially to tell it how to propagate and update. The EKF then takes in the DGPS and stereo measurements and uses them with the INS solution to calculate the current error state. The EKF produces the error state as well as the covariance matrix, in Figure 22. Both the error state and the INS solution are given to the Scorpion MasterNav class which time-aligns them to generate the corrected solution at any requested time. Note that for this research, the SMV processing time delay was not incorporated into the system, so measurements are incorporated at the time the images are taken.
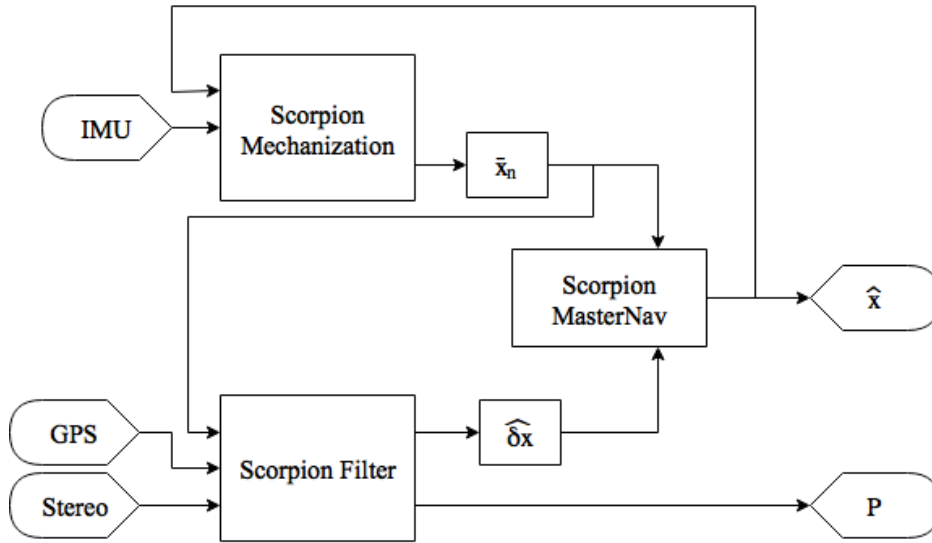
Figure 22. Error State EKF Flow in Scorpion

IV. Results and Analysis

This chapter contains the results of the EKF simulations. The results indicate that SMV can be used in a simulated environment to estimate a receiver aircraft's relative position at refueling distances with AAR accuracy. For this paper, the required AAR level accuracy is less than 1 m. The results from the EKF display according to time. However, in Figures 15 and 19, the stereo error depends on range. To compare filter results with corresponding stereo error, Figure 23 is provided to show the true range of the receiver relative to the tanker while the system receives measurements.
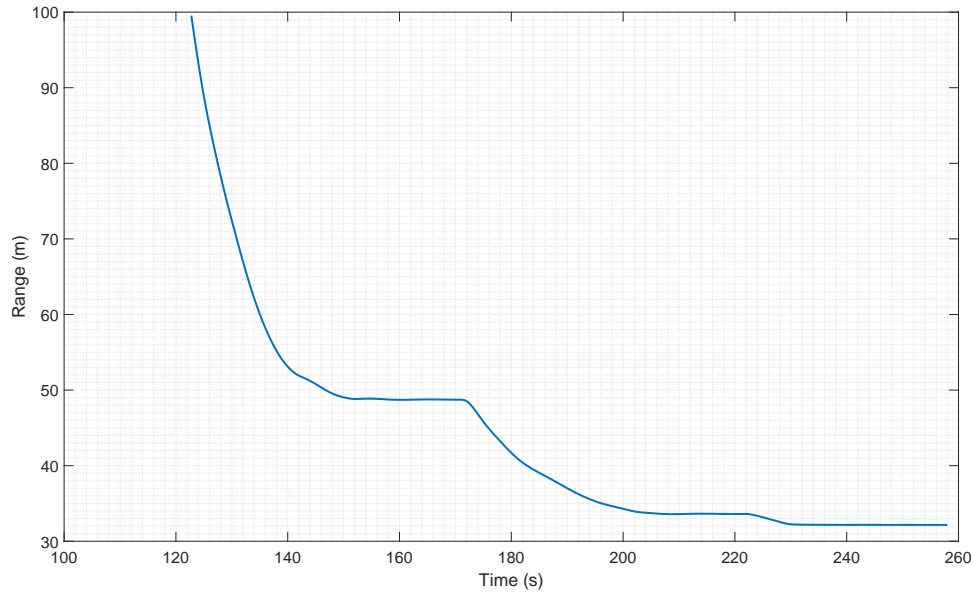
Figure 23. Receiver True Range from Tanker Plotted Against Time

This chapter is divided into 8 sections. The first six sections displays filter results for each of the six individual scenarios. The six different scenarios are:

    I. EKF with INS

    IS. EKF with INS and SMV

    S. SMV with no EKF or other measurements

    IG. EKF with INS and GPS measurements where GPS is lost within 50 m of the
        tanker

IGS. EKF with INS, GPS, and SMV where GPS is lost within 50 m of the tanker

IGS/NL. EKF with INS, GPS, and SMV where GPS is not lost

The seventh section graphically compares the six scenarios to show the strengths of the scenarios. The final section compares the six different scenarios for two different Cases defined is Section 3.3.3.3.3

Scenarios I and IG do not incorporate SMV measurements; therefore, they are identical between the two cases. They are shown to compare filter behavior between scenarios. Attitude plots are only displayed in Scenario I and IS to demonstrate a valid model and a functioning filter. Attitude plots are not displayed in any of the other results. No attitude measurements are taken, so the different scenarios have little influence on the filter attitude output. Additionally, Figure 26 demonstrates the navigation grade IMU has negligible error for this simulation. Each scenario is discussed, though to demonstrate general filter behavior, filter ensemble results are only displayed for scenarios I and IGS. To highlight filter behavior, combinations of the various scenarios are evaluated. It is important to note that the error states of the EKF are never directly evaluated. Evaluation is made on the complete solution by combining the INS solution with the EKF estimated error states. The SMV bias states are the only states discussed directly. It is important to note that the tanker's roll, pitch, and yaw are at a magnitude of 10^{-15}, 10^{-7}, and 10^{-16} rad, respectively. Thus, results displayed in the tanker body frame and in the NED frame can be interpreted as the same frame for this simulation. Besides Scenario I, all scenarios are evaluated as 100 iteration Monte Carlo simulations due to computational restrictions. The Monte Carlo does not apply to the SMV measurements. A single set of SMV was incorporated for each run, while the available IMU andDGPS measurements change for each run.

4.1   Scenario I - INS Only

Running the filter with only the INS does not provide additional accuracy, but it is necessary to see that the model generating the IMU data and the noise model in the filter align with each other. The filter's state estimation and covariances do not match reality

if these two do not align. Figures 24 to 26 show the results of the filter for its position, velocity, and attitude respectively. Each set of INS results is the compilation of a 500 run Monte Carlo simulation. The figures display both the error between the filter mechanized estimate and the true value for each of the runs. It also presents the filter's covariance bounds (represented by the 1-σ value). The ensemble calculated error mean and calculated 1-σ are also present. When the two models match, the mean is zero. The 1-σ bounds for both the filter and the ensemble should also align. The two align very closely in Figure 24. There is a small mean value by the end of the run most likely caused by a known error in the calculation of the IMU bias values. The final mean error values for position, velocity and attitude can be seen in Table 7. However, as Figures 24 to 26 show, the simulated data is a close enough match of the filter model to perform the needed sensor combinations.

Table 7. Mean Error Bias of Ensemble Position Error between the Tanker and the Receiver based on INS Only Filter Input. Results are Displayed in NED Frame

	Position (m)	Velocity (m/s)	Attitude (rad)
North	1.79	0.0119	$-3.40\mathrm{e}{-6}$
East	-0.928	-0.0077	$3.97\mathrm{e}{-6}$
Down	1.16	0.0086	$7.62\mathrm{e}{-6}$
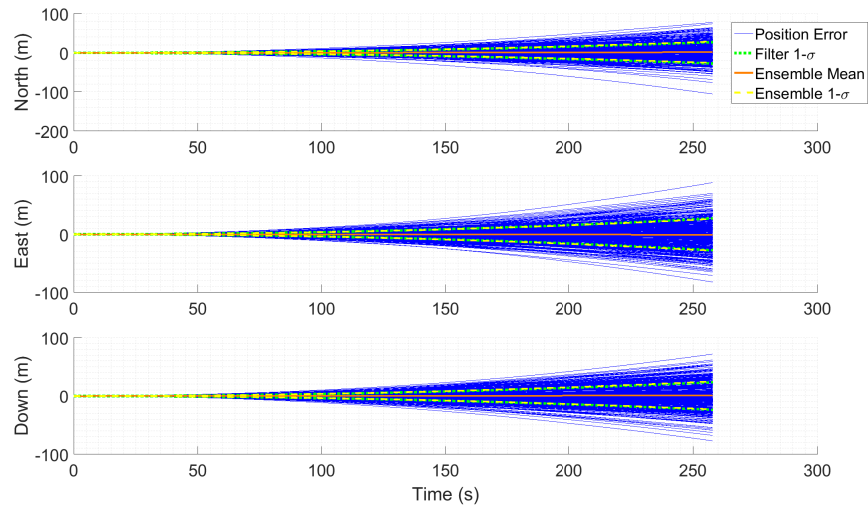
Figure 24. Scenario I Filter Position Results. Displaying Error between Filter Estimated Relative Position and True Relative Position for 500 Iteration Monte Carlo Simulation. The Plot Contains 500 Individual Runs with the Filter Estimated 1-σ, the Ensemble 1-σ, and the Ensemble Mean.
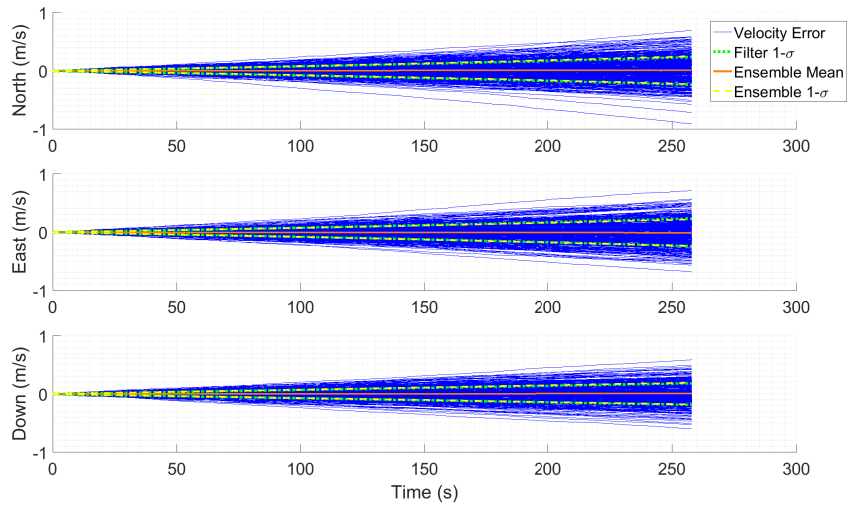
Figure 25. Scenario I Filter Velocity Results. Displaying Error between Filter Estimated Relative Velocity and True Relative Velocity for 500 Iteration Monte Carlo Simulation. The Plot Contains 500 Individual Runs with the Filter Estimated 1-σ, the Ensemble 1-σ, and the Ensemble Mean.

60
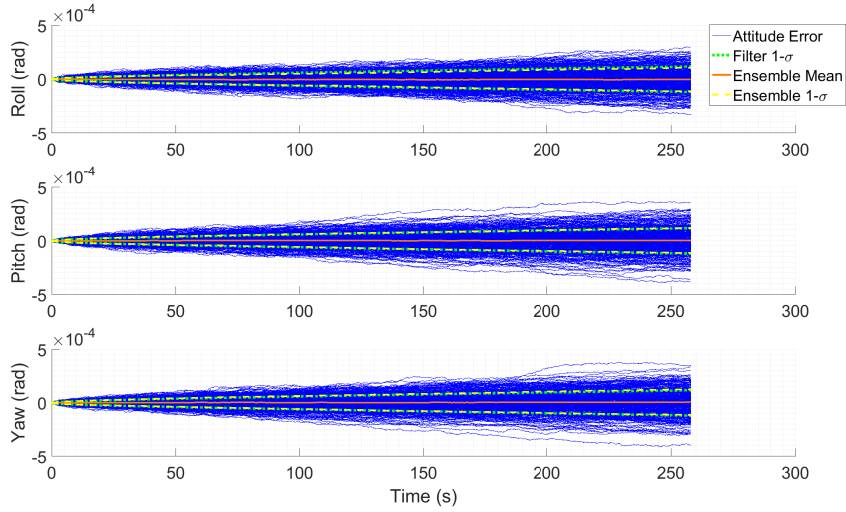
Figure 26. Scenario I Filter Attitude Results. Displaying Error between Filter Estimated Relative Attitude and True Relative Attitude for 500 Iteration Monte Carlo Simulation. The Plot Contains All 500 Individual Runs with the Filter Estimated 1-σ, the Ensemble 1-σ, and the Ensemble Mean.

4.2   Scenario IS - INS and SMV Combined

Scenario IS is the core scenario of this research. The goal is to successfully combine SMV and INS data in an EKF to achieve AAR level accuracy. To highlight the performance of the filter, the full filter ensemble results for Scenario IS are displayed. Each ensemble plot displays the error in the filter's estimated relative state, position, velocity, or attitude. It also displays the calculated ensemble mean of those errors, the calculated ensemble 1-σ of the errors, and the filter estimated 1-σ.

4.2.1   Position.

This section displays the results of the filter Case 1 and Case 2 positions for Scenario IS. All positions are relative positions between the tanker and the receiver in the NED frame. All covariances (1-σ values) are, likewise, transformed into representations of the relative states as calculated in Equations (75), (77) and (79).

61

4.2.1.1 Case 1.

Recall that Case 1 takes the measurements as provided and does not remove the characterized mean through preprocessing the measurements. Case 1 is a general, conservative approach. Rather than compensating for biases present in the measurements, the filter is tuned with larger parameters for the stereo bias state σ and τ. The general approach is an attempt for greater flexibility in other scenarios that do not share similarities in the aircraft, terrain, or flight paths with this simulation.

Figure 27 displays the error for each of the 100 runs in Case 1 for the filter's estimated relative position in the NED frame for the full duration of the simulation. Figure 27 clearly shows that the filter estimated relative position drifts until the SMV snap to a smaller error and covariance to small to observe in this figure. This is expected since the SMV measurements come with approximately half-meter accuracy in Figure 16 and feed into a filter with covariance that has grown to a 6 meter 1-σ. Little else can be observed due to the scale of the figure.

To better observe the filter behavior, Figure 28 focuses on the last 120 s of the simulation. An important filter behavior to observe is the bump in ensemble mean error at the 180 s mark. This is due to a large bias in the SMV measurements unaccounted for in the characterization and is due to the aircraft approach in the simulation. At this point in the simulation, the accuracy of the ICP algorithm drops because the aircraft's tail leaves the camera Field of View (FOV), a real world problem that is ever present. This is an error in the SMV measurements; therefore, it is present in every case and scenario. Most of the iterations fall within the filter 1-σ instead of the expected 68% due to the conservative nature of the design. The filter is intentionally designed to be more conservative while still predicting good 1-σ values at the end of the simulation with 50 cm, 8 cm, and 6 cm in the North, East, and Down, respectively. The variance of the bias states largely dictate these accuracies. Since, the measurement equation incorporates both the measurement noise and the bias, the filter has to incorporate both components. Thus the larger 1-σ of the bias states prevents the filter covariance from shrinking too quickly. The resulting filter covariance is

higher since larger variances in the biases are also present in Case 1.

The bias states do not just limit the covariance, they also absorb and correctly estimate some of the bias. In Figure 29, the filter estimates of the SMV bias are plotted against the SMV error. While this plot is not useful for a quantitative comparison of the bias state against the actual stereo bias, it does show how closely the bias state is able to absorb error in the stereo measurement. For this particular scenario the SMV measurement is the only measurement the filter incorporates. As a result, it does not efficiently determine the bias in the measurement and the correct measurement. Therefore, it only absorbs a portion and poorly estimates the bias in Figure 29.
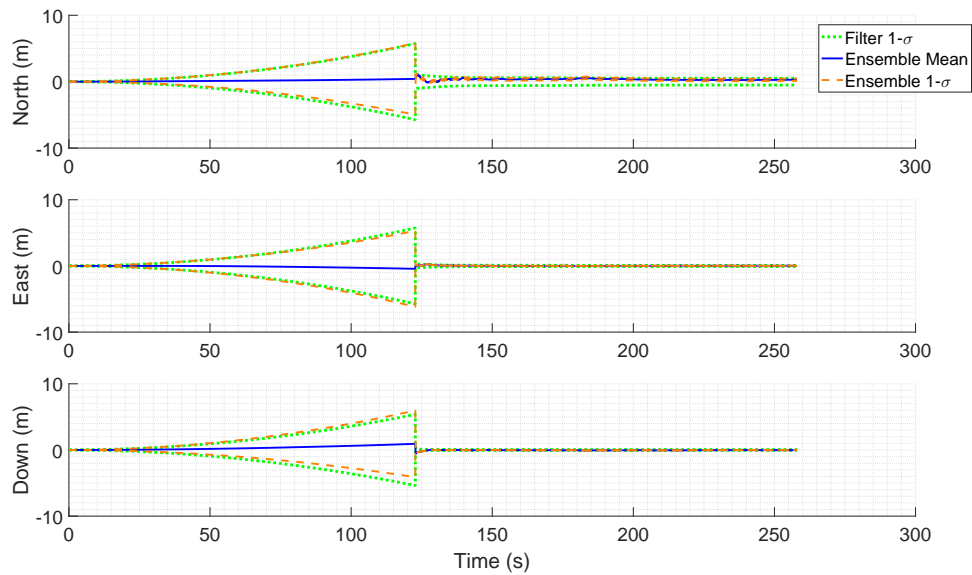
Figure 27. Case 1 Scenario IS Error between Filter Estimated Position and True Position for Full Simulation with 100 Iterations including Ensemble Error Mean, Ensemble Error 1-σ, and Filter 1-σ in the NED Frame

Figure 28. Case 1 Scenario IS Error between Filter Estimated Position and True Position within 50 m with 100 Iterations, Including Ensemble Error Mean, Ensemble Error 1-σ, and Filter 1-σ in the NED Frame
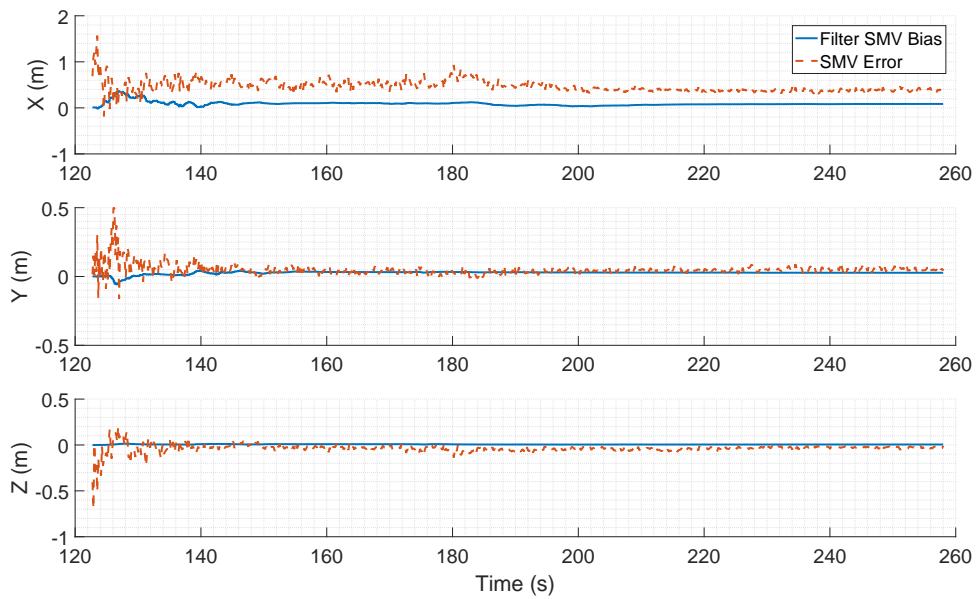
Figure 29. Case 1 Scenario IS Estimated Stereo Bias Against SMV Error

4.2.1.2 Case 2.

Recall that Case 2 preprocesses the measurements by first removing the characterized mean. As discussed in Section 3.3.3.3.3, the SMV measurements are preprocessed to remove the characterized bias from the data. When implementing Case 2, the original parameters

are changed during filter tuning. The σ function developed in Section 3.3.3.3.3 is scaled by a factor of 3 to account for uncharacterized errors and to insure the filter functions properly. Without the increase, the filter covariance shrinks and errors grow to result in a filter estimate outside its predicted covariance.

Figure 30 focuses on the last 120 seconds of the simulation to observe the filter functionality. At first, the filter appears to perform poorly with portions of the simulation outside the 1-σ bounds. However, the filter is more finely tuned, and uncharacterized errors, like the large jump at 180 seconds, are not covered by the covariance. When no uncharacterized errors are present, the filter covariance bounds encompass the entire ensemble. This means the filter is over conservative. Rather than approximately 68% of the estimates falling within in the covariances bounds, 100% of the estimates fall within the 1-σ covariance. It was not possible to completely characterize the SMV biases. Thus the filter was designed to be more conservative to account for the uncharacterized errors. It is better for the filter to be more accurate than it thinks it is than for it to be less accurate than it is estimating. The filter covariance bounds (1-σ) at the end of the simulation are 8 cm, 5 cm, and 5 cm in the North, East, and Down, respectively. These improve bounds over Case 1, especially in the North direction. With the decreased bounds, the filter can still accurately estimate the relative positions.

The offset in the East plot in Figure 30 presents the same bias in the SMV measurements, but the filter no longer has the increased bias state covariance to account for it. The Case 2 decreased ability to estimate the SMV bias is another factor in the "increased" bias. Figure 31 shows the comparison of the filter bias state against the SMV measurement errors. The characterized mean function removes approximately only 0.5 cm at close distances. In Case 2, almost the same amount of SMV bias is present, but now it has a FOGM bias with a smaller 1-σ value and a smaller time constant. This combination causes any previously estimated and stored bias to be lost and the filter has a hard time estimating any of the bias value near the end of the simulation. For Case 2, it actually estimates a slight bias in the wrong direction, increasing the total estimation error.
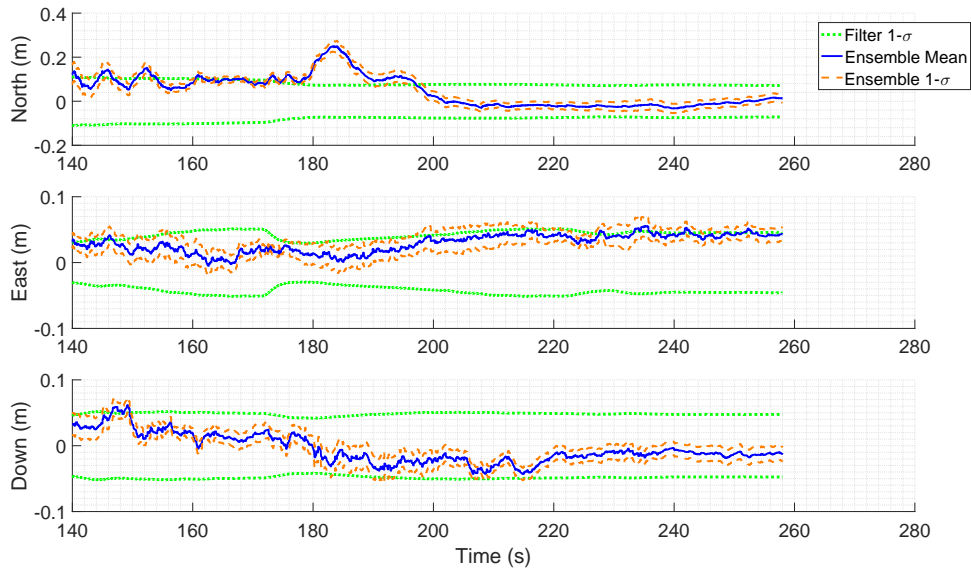
Figure 30. Case 2 Scenario IS Error between Filter Estimated Position and True Position within 50 m with 100 Iterations, Including Ensemble Error Mean, Ensemble Error 1-σ, and Filter 1-σ in the NED Frame
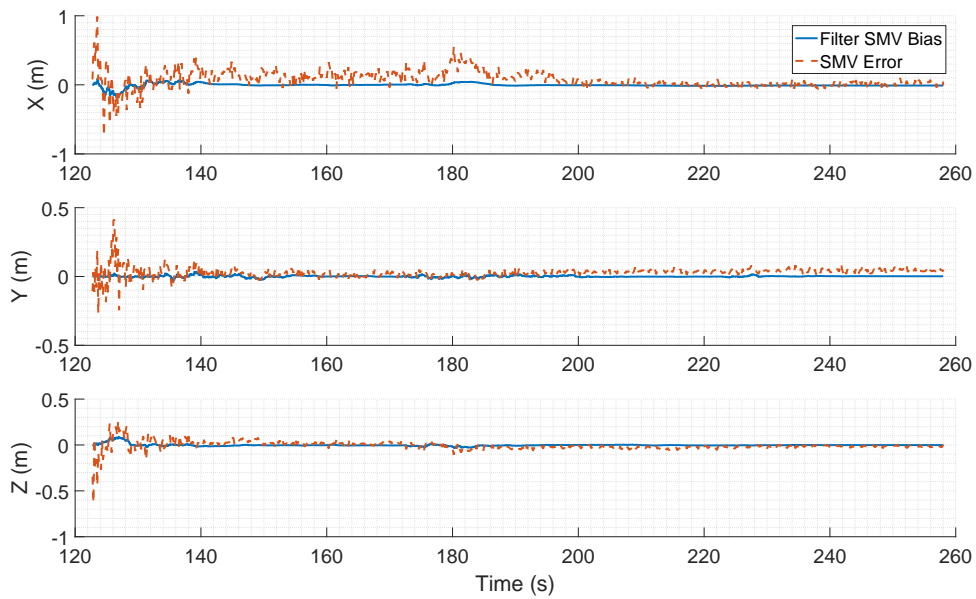
Figure 31. Case 2 Scenario IS Estimated Stereo Bias against Actual SMV Error

Table 8 provides a direct comparison of the Case 1 and Case 2 relative positions results. Instead of looking at the RMSE for specific times, Table 8 looks at the RMSE for a portion of the simulation. The Mean Squared Errors (MSEs) was calculated for each iteration in the ensemble and all values that fell within the desired range were summed together.

66

The square root was taken to obtain the RMSE. Table 8 confirms what Figures 28 and 30 indicate. Case 2 outperforms Case 1 under the conditions of Scenario IS.

Table 8. Comparison of RMSE for Scenario IS Case 1 and Case 2 Filter Estimated Relative Position Errors when Receiver Is within 100 m and 47 m of Tanker

	100 m			47 m		
Scenario	North (m)	East (m)	Down (m)	North (m)	East (m)	Down (m)
Case 1	0.398	0.0497	0.0619	0.375	0.0313	0.0458
Case 2	0.0945	0.0371	0.0454	0.082	0.0382	0.0238

4.2.2   Velocity.

This section displays the results of the filter Case 1 and Case 2 velocities for Scenario IS. All velocities are relative between the tanker and the receiver in the NED frame. All covariances, likewise, transform into representing the relative states.

4.2.2.1   Case 1.

Figure 32 observes the last 120 seconds of the simulation. It is clear the velocity states are observable with only receiver SMV measurements. Ultimately the bias does not reflect much in the velocity because the common error is differenced out. As a result, velocity ensemble covariance closely matches the filter estimated covariance. The ensemble mean does vary as a result of the SMV measurements.
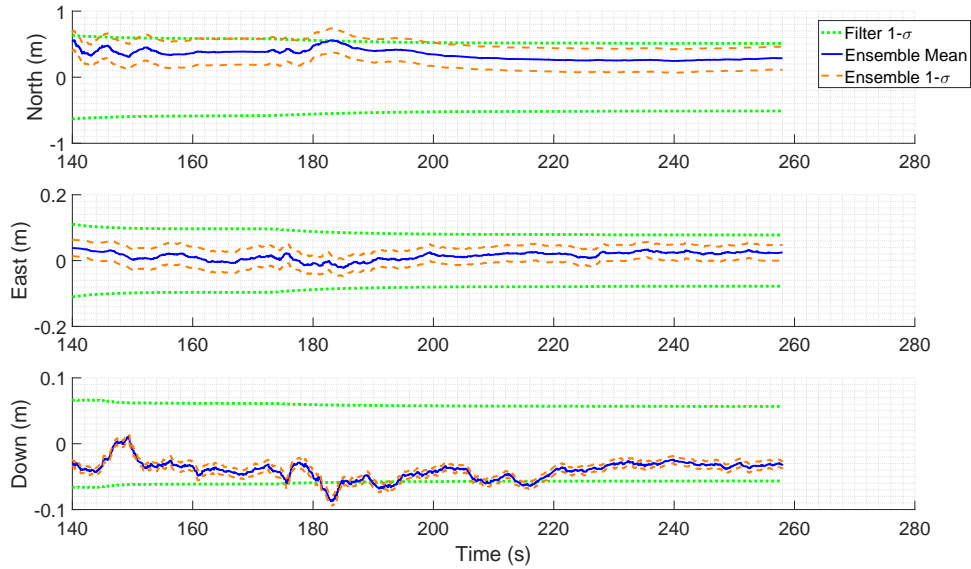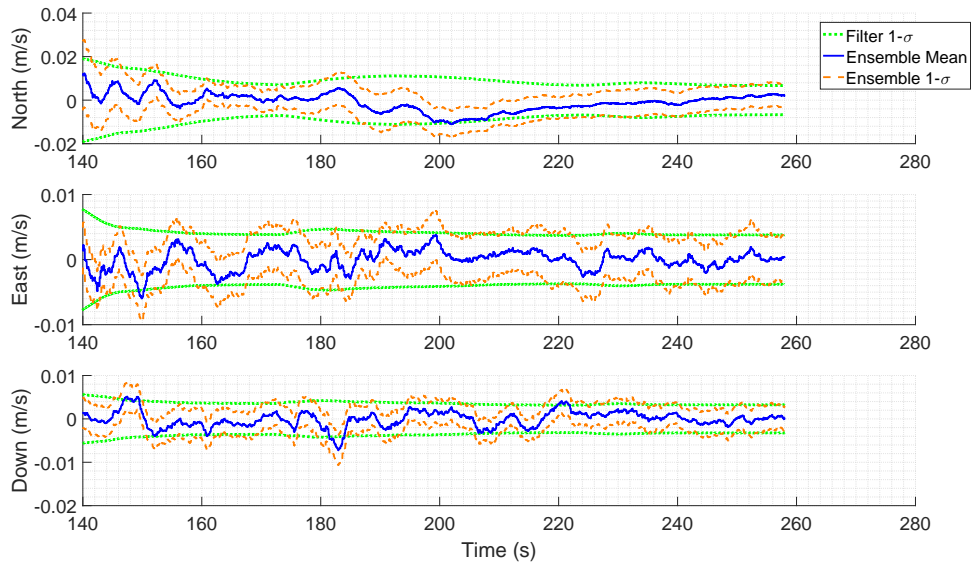
Figure 32. Case 1 Scenario IS Error between Filter Estimated Velocity and True Velocity within 50 m with 100 Iterations, Including Ensemble Error Mean, Ensemble Error 1-σ, and Filter 1-σ in the NED Frame

4.2.2.2 Case 2.

The zoomed in plot of the last 120 s of the simulation in Figure 33 highlight the filter behavior for Case 2. The behavior is similar to Case 1 but with slightly smaller covariance. This is observed by comparing the sections of the simulation that have larger error, such as the section at 180 s.
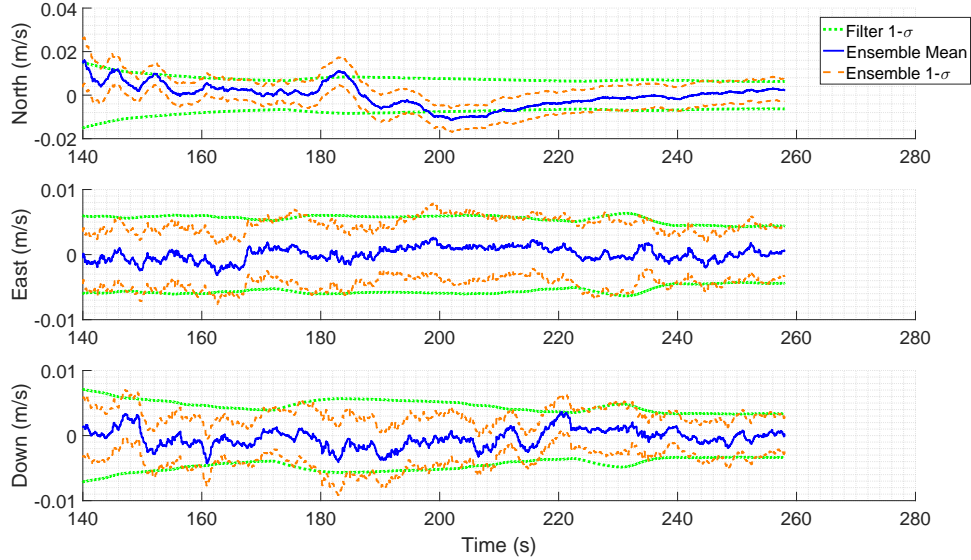
Figure 33. Case 2 Scenario IS Error between Filter Estimated Velocity and True Velocity within 50 m with 100 Iterations, Including Ensemble Error Mean, Ensemble Error 1-σ, and Filter 1-σ in the NED Frame

4.2.3 Attitude.

This section displays the results of the filter Case 1 and Case 2 attitudes for Scenario IS. All attitudes are relative rotations between the tanker and the receiver in the NED frame. All covariances, likewise, transform into representing the relative states.

4.2.3.1 Case 1.

Figure 34 displays the relative attitude estimation error for Scenario IS for Case 1. The filter clearly has observability into the Roll and Pitch with only relative position measurements. Based on these results, the filter is correctly estimating the attitude errors and the relative position measurements are enough to prevent the continued drift of the roll and pitch. However, without observability into the yaw the covariance will continue to grow. When performing observability analysis on the filter for each time step of the simulation, the typical observability was 16 states (up to 19). Because the measurements are relative, each observable state actually corresponds to the relative states. The 16 observable states consist of the three relative position states, the three relative velocity states, two of the relative attitude states, the three relative accelerometer bias states, two of the relative gyro

69

bias states, and all three stereo bias states.
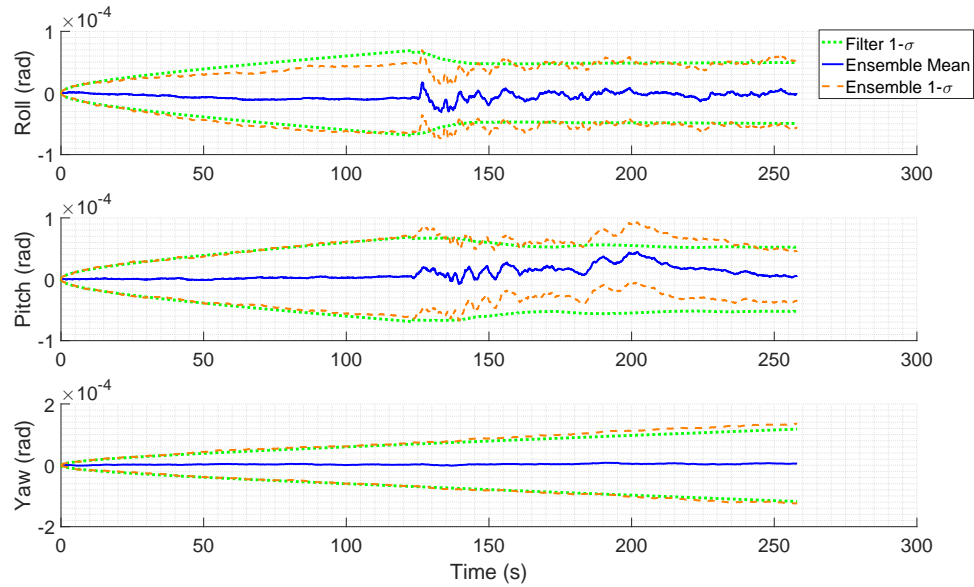
Figure 34. Case 1 Scenario IS Error between Filter Estimated Attitude and True Attitude for Full Simulation with 100 Iterations, Including Ensemble Mean, Ensemble 1-σ, and Filter 1-σ in the NED Frame

4.2.3.2   Case 2.

Figure 35 displays the relative attitude estimation error for Case 2. There is very little change from Case 1. The ensemble mean and 1-σ behave as respected within the filter covariance bounds and the resulting errors are comparable to the errors seen in Case 1.
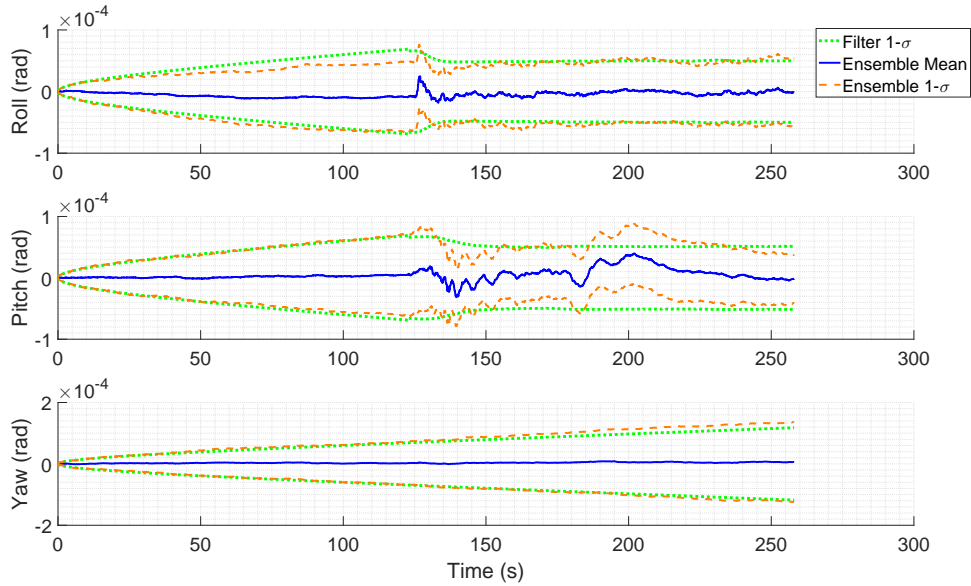
Figure 35. Case 2 Scenario IS Error between Filter Estimated Attitude and True Attitude with 100 Iterations, Including Ensemble Error Mean, Ensemble Error 1-σ, and Filter 1-σ in the NED Frame

The attitude estimates represent one of two different types of states that are unobservable. The attitude error will not be evaluated directly for any of the other scenarios. It was provided to show overall filter performance and displaying attitude for all scenarios will provide no added benefit since the only measurements received are position measurements and the error is of such a small magnitude due to the navigation grade IMU. Filter performance was consistent between scenarios.

4.2.4 SMV Bias.

The SMV bias has been discussed briefly as part of the analysis on the relative position results. However, this section will look at the values of the states themselves as well as the filter predicted covariance and actual ensemble covariance.

4.2.4.1 Case 1.

Figure 36 displays the error in the stereo bias state estimate for Case 1. As expected, the error in the bias estimation falls within the covariance bounds estimated by the filter, which are designed to be conservative. There is a burst of error in the down direction when

71

measurements first begin. This is ultimately due to poor modeling of the error at this point. The stereo FOGM bias state has a lower modeled noise value than is reflected in the measurements. Because of the distance and speed of the approaching aircraft, this only occurs for a few measurements before it falls within the filter estimated covariance bounds. The behavior observed for this scenario is consistent with the filter behavior in the rest of the scenarios.
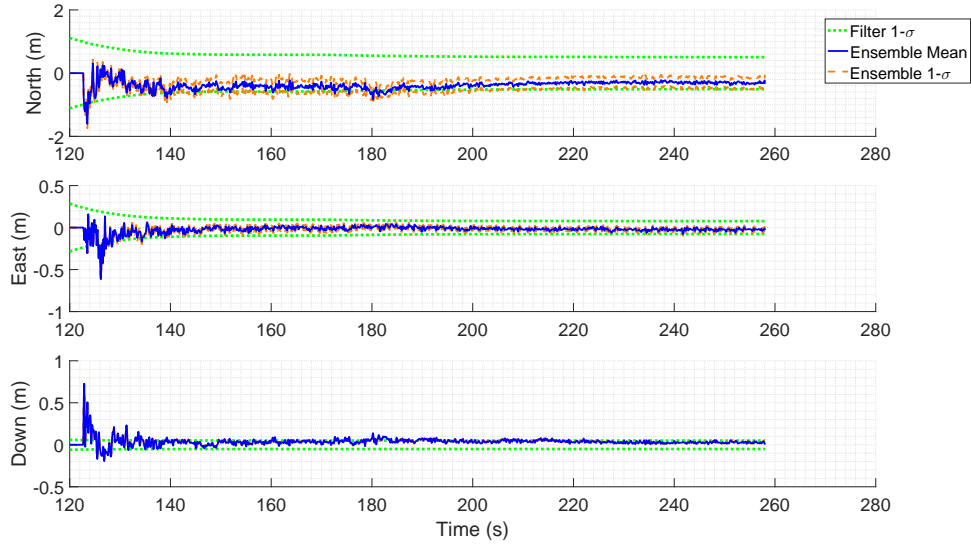
Figure 36. Case 1 Scenario IS SMV Bias State Ensemble Mean, Ensemble 1-σ, and Filter Estimated 1-σ in the NED Frame

4.2.4.2 Case 2.

Figure 37 displays the error in the stereo bias state estimate for Case 2. The covariance is smaller for Case 2 due to the preprocessing and reduced FOGM noise. Case 2 also has the error spike in the down direction at the beginning of measurements. This is indicative that the combined model for the down direction is not a tightly fitting model at larger distances. Like Case 1, the error quickly falls within the filter covariance. The East error pushes the edges of the filter covariance which matches what was seen in the position error discussion in Section 4.2.1.2. The behavior observed for this scenario is consistent with the filter behavior in the rest of the scenarios.
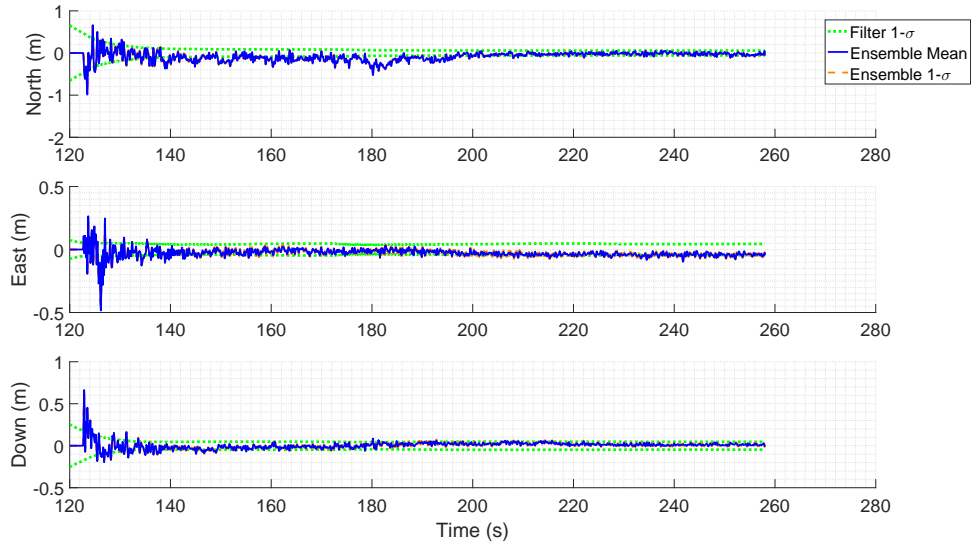
Figure 37. Case 2 Scenario IS SMV Bias State Ensemble Mean, Ensemble 1-σ, and Filter Estimated 1-σ in the NED Frame

The stereo bias states will not be discussed or evaluated for the rest of the scenarios. The filter performance in these states is consistent and there is no benefit to discussing them further.

4.2.5 Accelerometer Bias.

This section will look at the results for the filter's accelerometer bias estimation. Results are displayed as an error in the relative bias state estimation between the tanker and the receiver. The bias errors for each aircraft only correspond to that aircraft, but because of the extremely small attitude changes in this simulation it is a close enough approximation to treat them as a relative measurement.

4.2.5.1 Case 1.

Figure 38 displays the error in the filter's estimation of the accelerometer bias states for Case 1. The filter performs as expected. The ensemble mean and ensemble 1-σ align closely with the filter estimates. The relative position measurements actually improve the accuracy of the filter, dropping the uncertainty by a factor of 2.
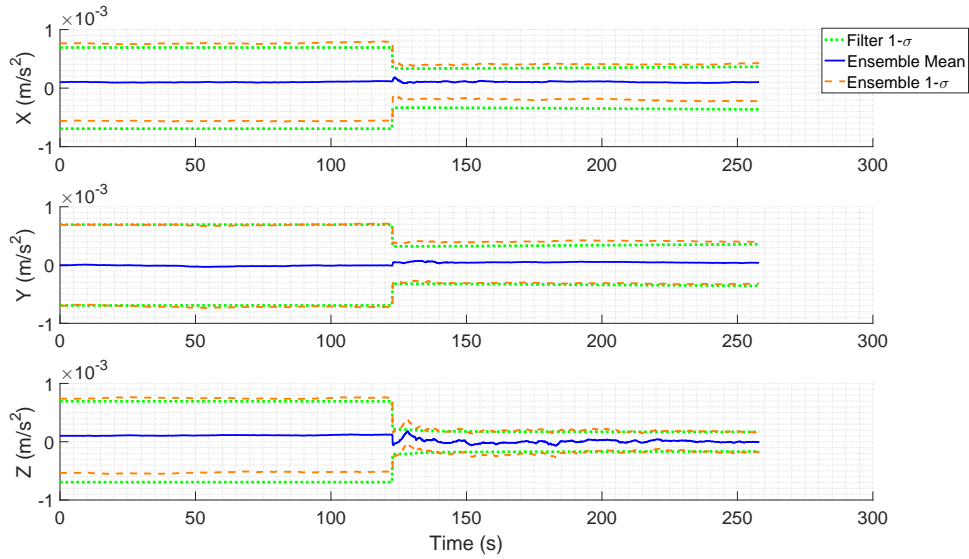
Figure 38. Case 1 Scenario IS SMV Relative Accelerometer Bias State Ensemble Mean, Ensemble 1-σ, and Filter Estimated 1-σ in the Tanker Body Frame

4.2.5.2 Case 2.

Figure 39 displays the error in the filter's estimation of the accelerometer bias states for Case 2. The behavior is consistent with that observed in Case 1. The mean error is slightly smaller, but the scale of these estimates is such a small magnitude that the difference is negligible.
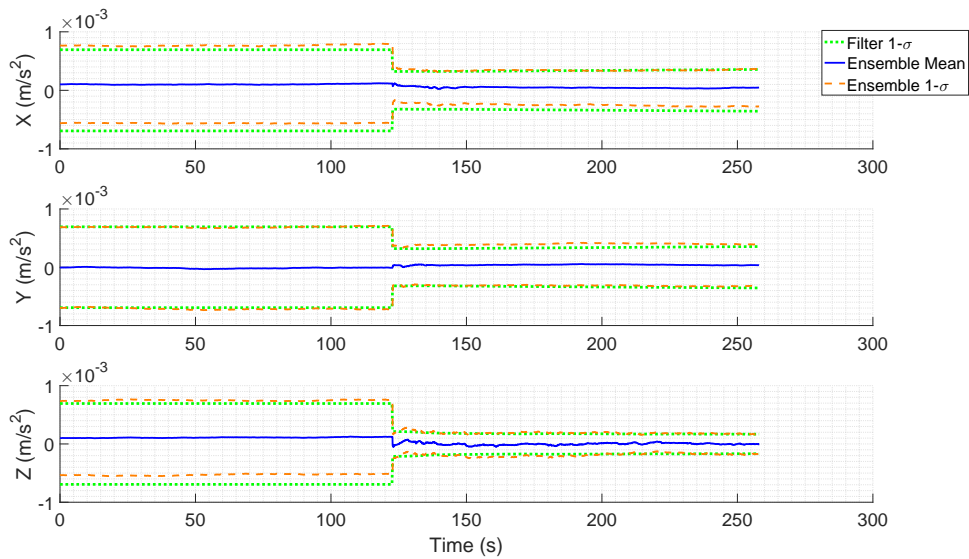
Figure 39. Case 1 Scenario IS SMV Relative Accelerometer Bias State Ensemble Mean, Ensemble 1-σ, and Filter Estimated 1-σ in the Tanker Body Frame

The accelerometer bias states will not be discussed or evaluated for the rest of the scenarios. The filter performance in these states is consistent and there is no benefit to discussing them further.

4.2.6   Gyro Bias.

This section will look at the results for the filter's gyro bias estimation. Like in Section 4.2.5, results are displayed as an error in the relative bias state estimation between the tanker and the receiver.

4.2.6.1   Case 1.

Figure 40 displays the error in the filter estimated relative gyro bias states for Case 1. The relative position measurements do not provide much insight into the gyro bias states. There is observability into the X and Y, but the measurements only have a slight impact on the estimation of the Gyro biases. The Z bias state is not observable at all leaving the error in the bias state estimate equal to the values of the actual biases themselves. The key observation is that the filter is behaving properly. The error ensemble mean and 1-σ align with the filter's estimated 1-σ.
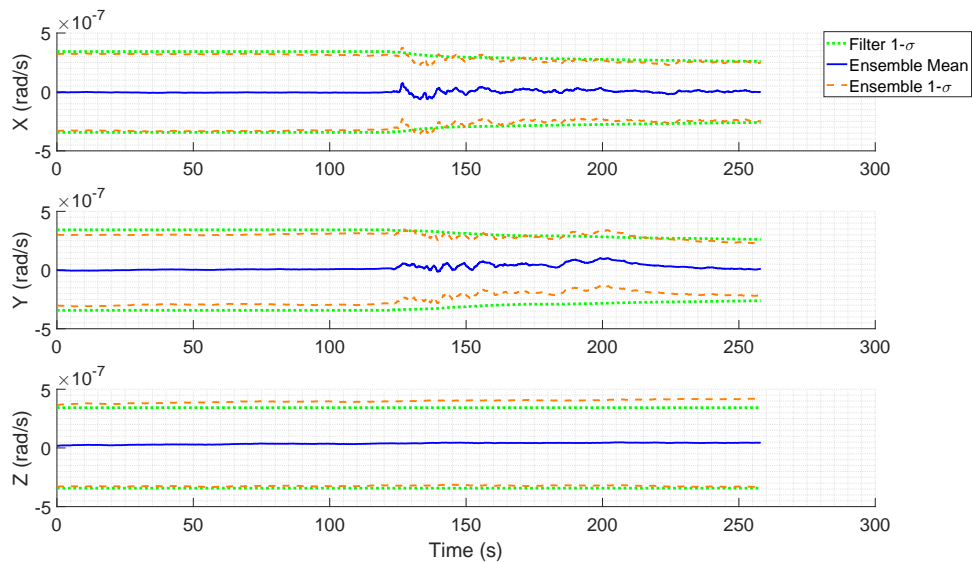
Figure 40. Case 1 Scenario IS SMV Relative Gyro Bias State Ensemble Mean, Ensemble 1-σ, and Filter Estimated 1-σ in the Tanker Body Frame

75

4.2.6.2 Case 2.

Figure 41 displays the error in the filter estimated relative gyro bias states for Case 2. There is little difference in the filter's behavior between the two cases. As in Case 1, the X and Y receive some improved estimation with no observation at all into the Z. The filter performance is consistent with the filter estimated 1-σ aligning with the ensemble error mean and ensemble error 1-σ.
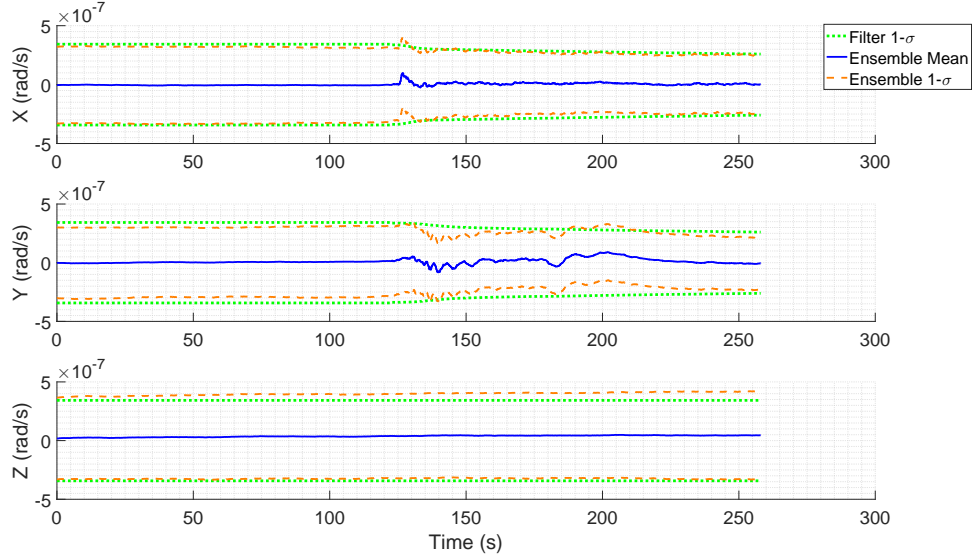
Figure 41. Case 2 Scenario IS SMV Relative Gyro Bias State Ensemble Mean, Ensemble 1-σ, and Filter Estimated 1-σ in the Tanker Body Frame

The gyro bias states will not be discussed or evaluated for the rest of the scenarios. The filter performance in these states is consistent and there is no benefit to discussing them further.

4.3 Scenario S

Recall that Scenario S refers to the SMV measurements alone. Scenario S is not evaluated in detail here. It is primarily discussed in Section 3.3.3.3.3 and is also seen in Figures 16 and 29 for Case 1 and Figures 19 and 31 for Case 2.

4.4 Scenario IG

Recall that Scenario IG refers to the combination of INS and DGPS when GPS is lost 50 m from the tanker. Scenario IG is not discussed independently. It exists to show the drift in the EKF solution following the loss of DGPS. This effect is seen in both Figures 58 and 59. The DGPS signal keeps the RMSE low until it is lost. At that point the drift of the INS begins again causing the RMSE to grow large enough to cause problems in an AAR maneuver.

4.5 Scenario IGS

Recall that Scenario IG refers to the combination of INS, DGPS, and SMV when GPS is lost 50 m from the tanker. While the integration of the SMV is the primary design goal for the EKF, integrating DGPS into the EKF is essential. This gives the EKF the advantage of reliable and accurate measurements when available. The DGPS also improves the estimation of the SMV bias, thus improving the EKF solution when DGPS is lost.

4.5.1 Position.

This section displays the results of the filter Case 1 and Case 2 positions for Scenario IGS. All positions are relative positions between the tanker and the receiver in the NED frame. All covariances (and 1-σ values) are, likewise, transformed into representing the relative states.

4.5.1.1 Case 1.

Figure 42 displays the error for each of the 100 runs in Case 1 for the filter's estimated relative position in the NED frame. Unlike Scenarios I and IS, there is no sudden drop in the EKF solution error. This allows the entire run to be observed in one figure.

The DGPS signal integrates well into the EKF. For the first 147 s of the simulation both the filter and the DGPS bring the filter covariance down to a 1σ of 1.5 cm, 1.2 cm, and 1.4 cm in the North, East, and Down, respectively. The ensemble covariance closely

follows the EKF estimated covariance at this point. Once the DGPS ensemble mean drifts to follow the SMV measurements and the covariance grows to 19 cm, 3.7 cm, and 3.5 cm in the North, East and Down, respectively. The EKF is clearly able to maintain accurate estimation, even once DGPS is lost.

Another benefit of using the DGPS is the improved estimation of the SMV bias. Figure 43 shows the EKF estimated SMV bias state plotted against the smoothed SMV error for Case 1. Because of the additional DGPS measurements, the EKF better estimates the bias state. The DGPS reduces the covariance so when the SMV measurements come in, the filter knows the correct state to correctly bring the information into the bias state. Because the time constant is higher in Case 1, the information is stored longer in the bias state even after the DGPS is lost.

Figure 42. Case 1 Scenario IGS Error between Filter Estimated Position and True Position for Full Simulation with 100 Iterations Including Ensemble Error Mean, Ensemble Error 1-σ, and Filter 1-σ in the NED Frame
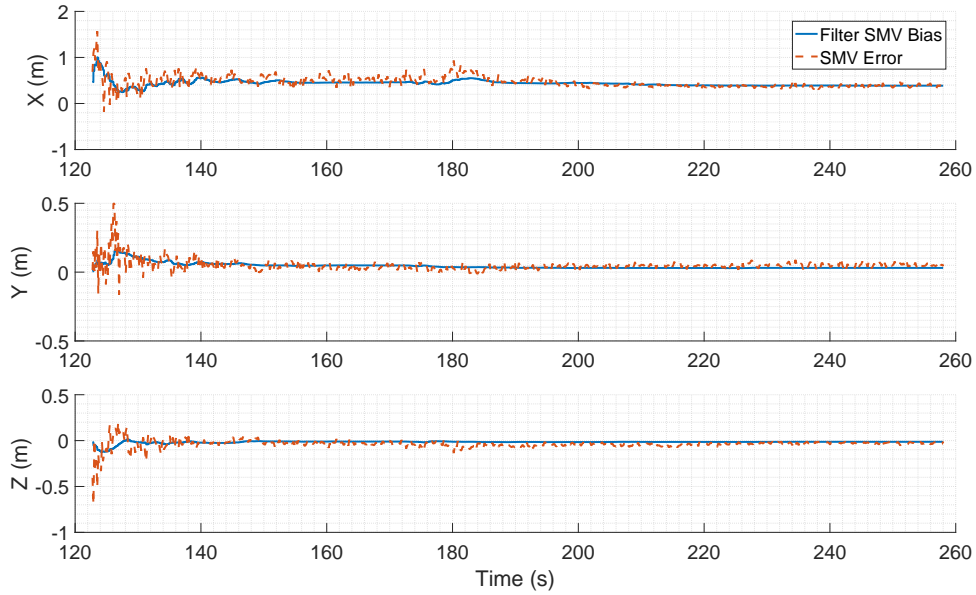
Figure 43. Case 1 Scenario IGS Estimated Stereo Bias Against Actual SMV Error

4.5.1.2 Case 2.

Figure 44 displays the error for each of the 100 runs in Case 1 for the filter's estimated relative position in the NED frame. For the first 147 s of the simulation, Case 2 is identical to Case 1 where the covariance is maintained to a 1σ of 1.5 cm, 1.2 cm, and 1.4 cm in the North, East, and Down, respectively. Once DGPS is lost, the covariance grows to 7.1 cm, 4.6 cm, and 4.7 cm. The slightly higher covariance in the East and Down directions is due to the smaller time constant associated with the SMV bias state. In Case 2 the bias quickly decorrelates, and the covariance rises to it's steady state. In Case 1, the SMV bias state decorrelates more slowly which prevents the bias from growing as quickly. Even though the SMV bias information is lost more quickly in this case, Figure 45 demonstrates the EKF more accurately estimates the SMV bias state while the DGPS is active. Long DGPS losses will ultimately decorrelate until the EKF operates as if it only has SMV. This capability will help the system to overcome short periods of DGPS unavailability.

79
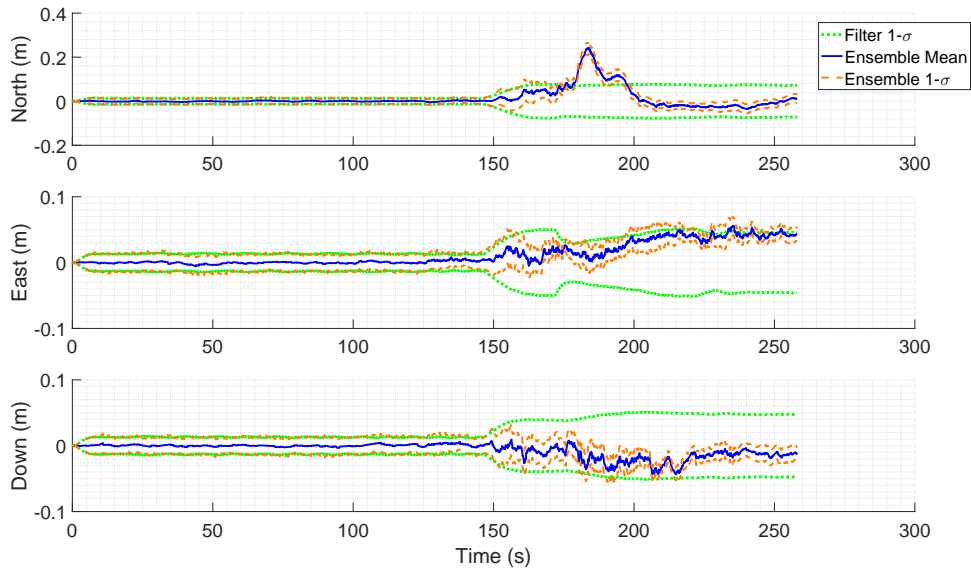
Figure 44. Case 2 Scenario IGS Error between Filter Estimated Position and True Position for Full Simulation with 100 Iterations Including Ensemble Error Mean, Ensemble Error 1-σ, and Filter 1-σ in the NED Frame
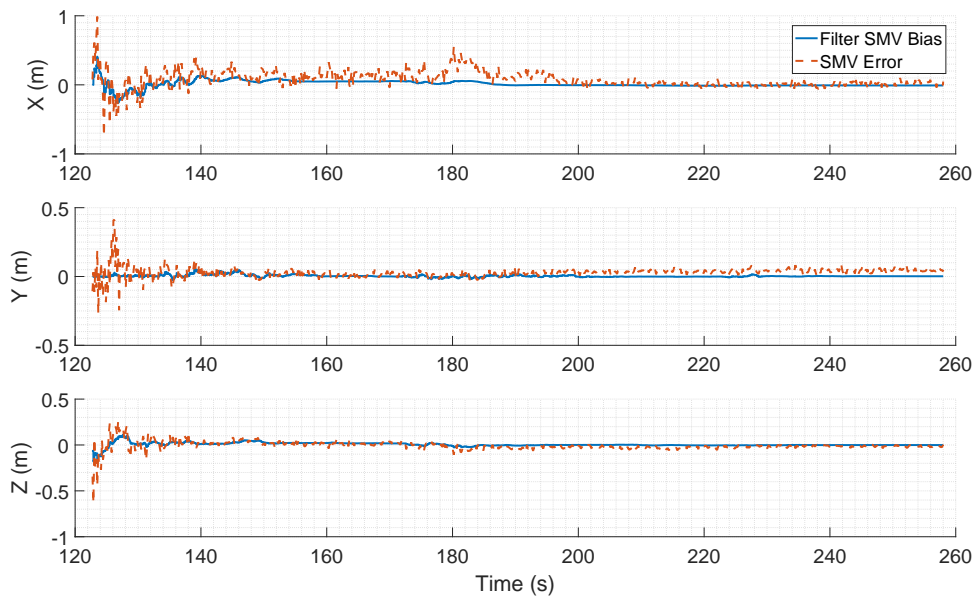
Figure 45. Case 2 Scenario IGS Estimated Stereo Bias Against Actual SMV Error

Table 9 shows the RMSE values for the relative position EKF solution when the receiver is within 100 m and 47 m of the tanker. The values follow the same trend as Table 8 where Case 1 has better values in some sections due to a better estimation of the SMV bias states. The most notable difference is the drop in the gap between the Case 1 and Case 2

80

North RMSE values. Because Case 1 more accurately estimates the bias due to the DGPS measurements, the EKF solution with only the SMV is much better than in Scenario 1.

Table 9. Comparison of RMSE for Scenario IGS Case 1 and Case 2 Filter Estimated Relative Position Errors when Receiver Is within 100 m and 47 m of Tanker

	100 m			47 m		
Scenario	North (m)	East (m)	Down (m)	North (m)	East (m)	Down (m)
Case 1	0.0712	0.0190	0.0257	0.0851	0.0210	0.0295
Case 2	0.0659	0.0324	0.0222	0.0783	0.0381	0.0245

4.5.2 Velocity.

This section displays the results of the filter Case 1 and Case 2 velocities for Scenario IGS. All velocities are relative between the tanker and the receiver in the NED frame. All covariances are transformed into representations of the relative states.
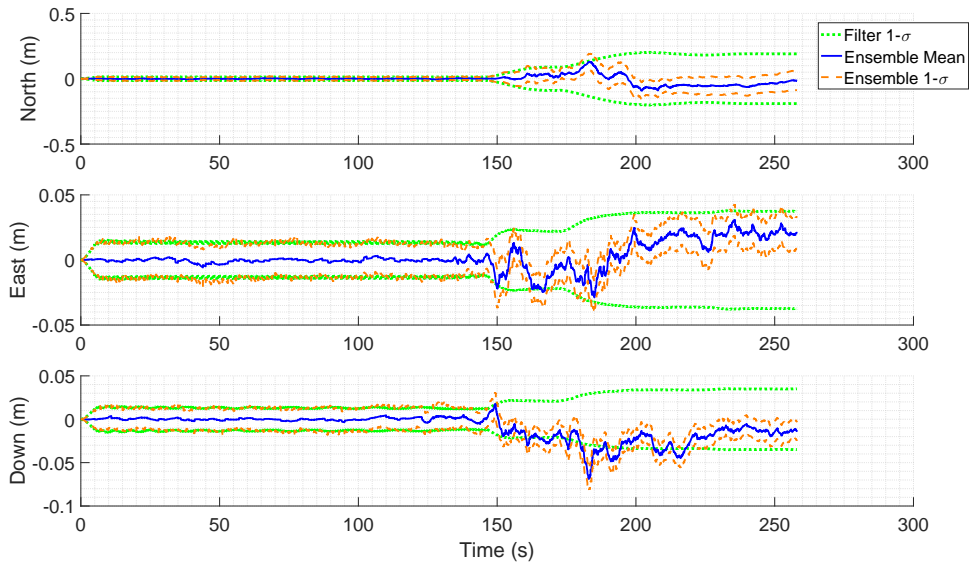
4.5.3 Case 1.

Figure 46 displays the error for each of the 100 runs in Case 1 for the filter's estimated relative velocity in the NED frame. Beside some covariance growth in the North direction, the SMV measurements closely maintain the filter estimated covariance. The covariance is maintained at 0.39 cm/s, 0.39 cm/s, and 0.36 cm/s in the North, East, and Down directions, respectively. till 147 s into the simulation. The DGPS loss at 147 s allows the covariance to drift to 0.66 cm/s, 0.38 cm/s, and 0.32 cm/s in the North, East and Down, respectively. While the drift in the North is noticeable, the final East and Down covariances are comparable to when DGPS is integrated. The velocity mean varies more without the DGPS because the ensemble mean error fluctuates, but the velocity maintains the same level of uncertainty.

81
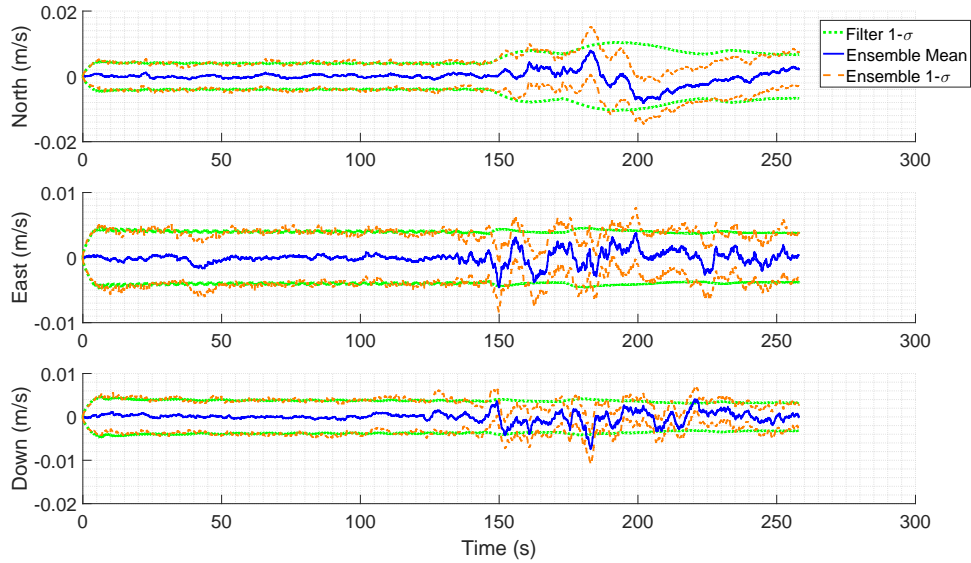
Figure 46. Case 1 Scenario IGS Error between Filter Estimated Velocity and True Velocity for Full Simulation with 100 Iterations, Including Ensemble Mean, Ensemble 1-σ, and Filter 1-σ in the NED Frame

4.5.4 Case 2.

Figure 47 displays the error for each of the 100 runs in Case 2 for the filter's estimated relative velocity in the NED frame. Similar to Case 1, the covariance is maintained at 0.39 cm/s, 0.39 cm/s, and 0.36 cm/s in the North, East, and Down directions, respectively, up to 147 s into the simulation. The DGPS loss at 147 s allows the covariance 1-σ to drift to 0.63 cm/s, 0.44 cm/s, and 0.34 cm/s in the North, East and Down, respectively, by the end of the simulation. These values are comparable to those in Case 1. The RMSE values are small that a discussion of them has no benefit, as observed in Section 4.8.2 in Tables 14 to 16.

82
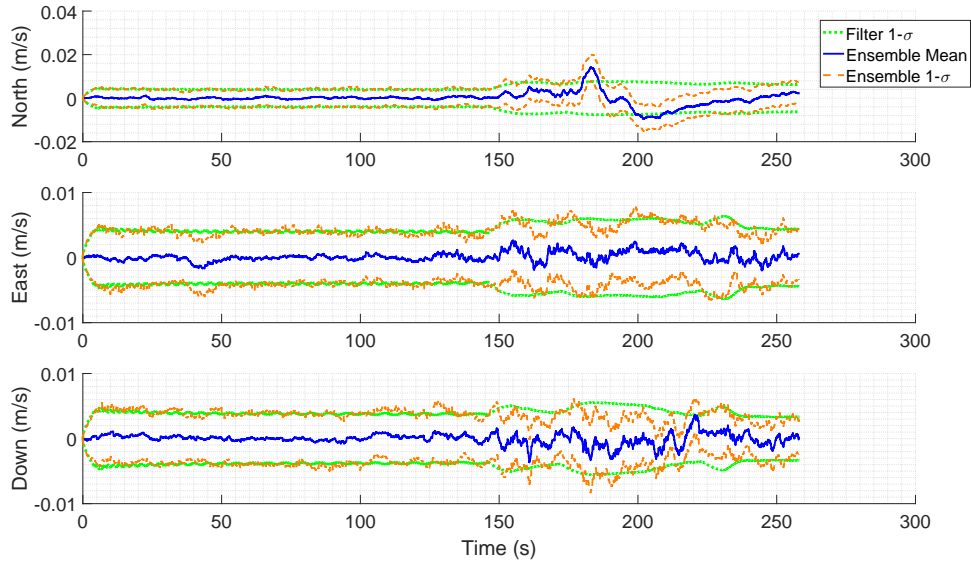
Figure 47. Case 2 Scenario IGS Error between Filter Estimated Velocity and True Velocity for Full Simulation with 100 Iterations, Including Ensemble Mean, Ensemble 1-σ, and Filter 1-σ in the NED Frame

4.6   Scenario IGS/NL

Scenario IGS/NL will not be discussed in detail, but the results are displayed for completeness. The filter is designed to be able to take the DGPS measurements when they are available. In the situation where the DGPS is never lost, the filter will continue to receive the updates.

4.6.1   Position.

This section will show the filter results for when DGPS is never lost. As expected, the filter performs even better when the DGPS measurements are never lost.

4.6.1.1   Case 1.

Figure 48 displays the error for each of the 100 runs in Case 1 for the filter's estimated relative position in the NED frame. The ensemble covariance and mean remain stable for the majority of the simulation, closely matching the filter estimated covariance. The introduction of the SMV measurements causes the mean to vary more than with DGPS

alone, but the filter still provides an accurate solution. Without the loss of the DGPS the filter continues to accurately estimate the SMV bias as seen in Figure 49.
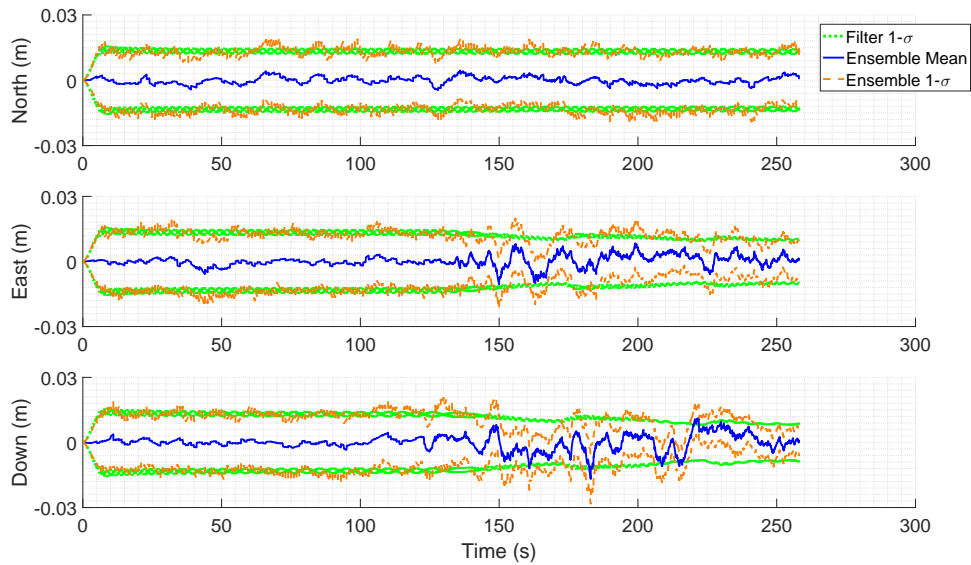
Figure 48. Case 2 Scenario IGS/NL Error between Filter Estimated Velocity and True Velocity for Full Simulation with 100 Iterations, Including Ensemble Mean, Ensemble 1-σ, and Filter 1-σ in the NED Frame
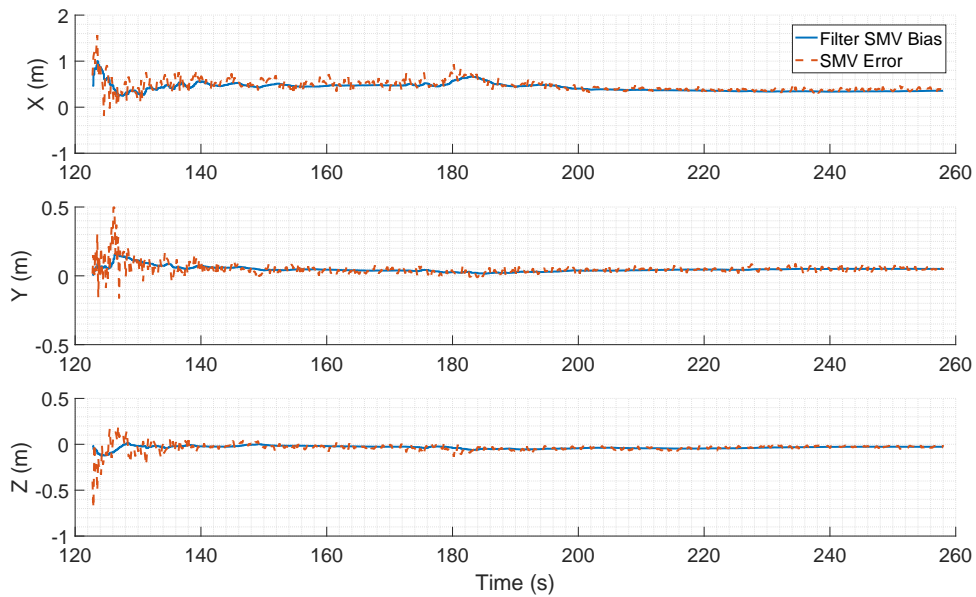
Figure 49. Case 2 Scenario IGS/NL Estimated Stereo Bias Against Actual SMV Error

4.6.1.2 Case 2.

Figure 50 displays the error for each of the 100 runs in Case 2 for the filter's estimated relative position in the NED frame. With the 2 cm accurate DGPS signal, the performance of Case 2 is effectively the same as Case 1. Figure 51 shows that Case 2 can also estimate the SMV bias more accurately when the DGPS continues.
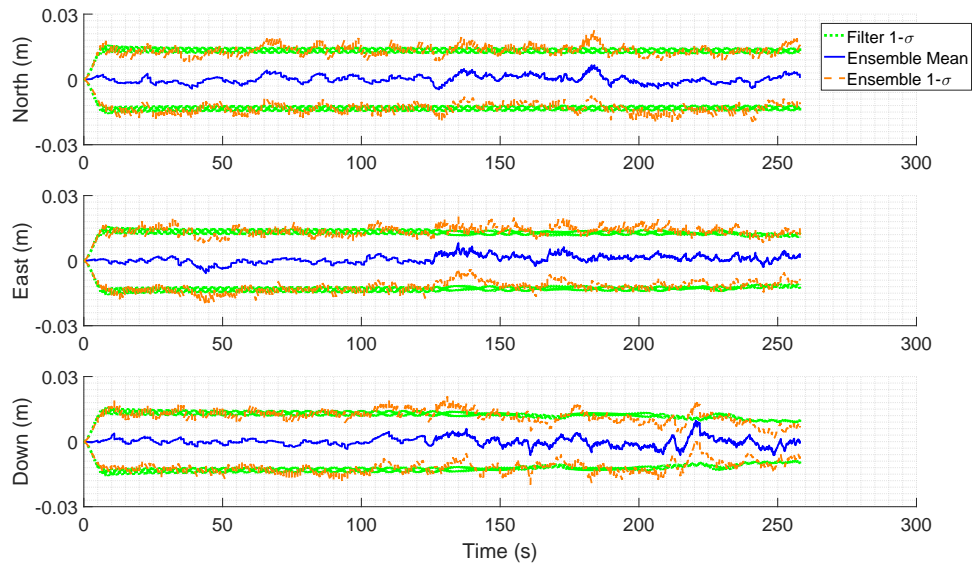
Figure 50. Case 2 Scenario IGS/NL Error between Filter Estimated Velocity and True Velocity for Full Simulation with 100 Iterations, Including Ensemble Mean, Ensemble 1-σ, and Filter 1-σ in the NED Frame
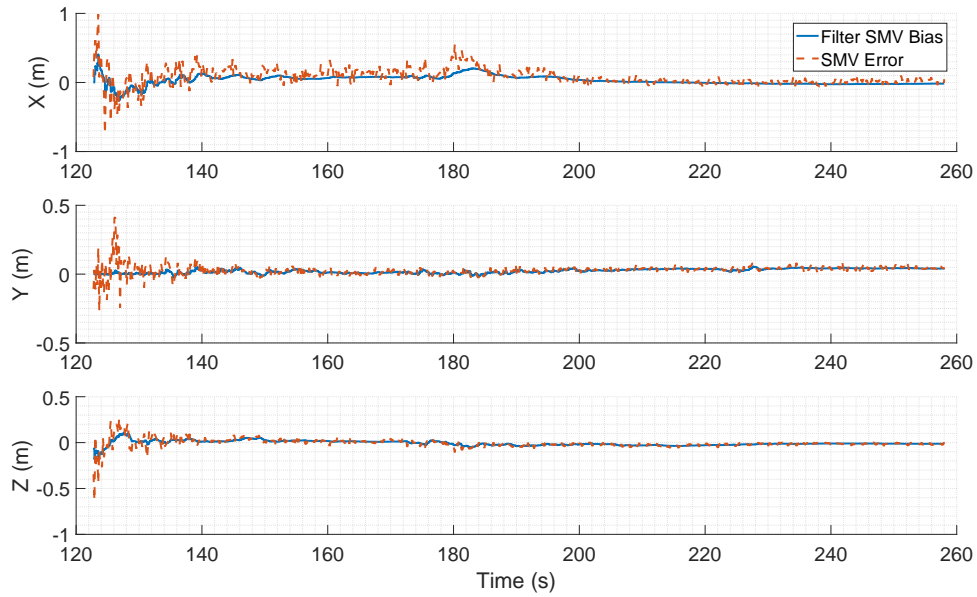
Figure 51. Case 2 Scenario IGS/NL Estimated Stereo Bias Against Actual SMV Error

4.6.2 Velocity.

Like with position, the velocity performs better when the DGPS measurements are not lost. Figures 52 and 53 display the error for each of the 100 runs in Case 1 and Case 2, respectively, for the filter's estimated relative velocity in the NED frame. The performance is consistent with the behavior observed in position.
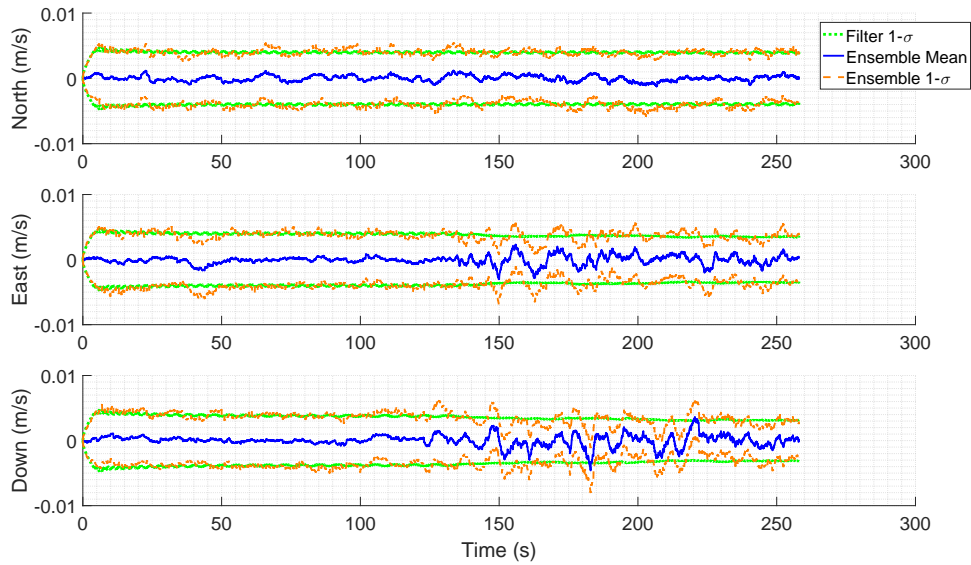
Figure 52. Case 1 Scenario IGS/NL Error between Filter Estimated Velocity and True Velocity for Full Simulation with 100 Iterations, Including Ensemble Mean, Ensemble 1-σ, and Filter 1-σ in the NED Frame
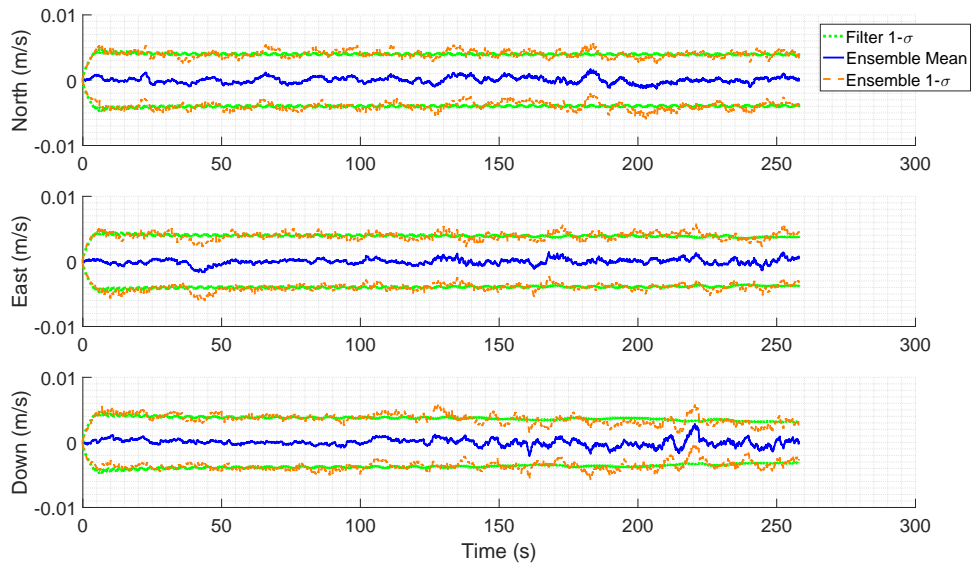
Figure 53. Case 2 Scenario IGS/NL Error between Filter Estimated Velocity and True Velocity for Full Simulation with 100 Iterations, Including Ensemble Mean, Ensemble 1-σ, and Filter 1-σ in the NED Frame

4.7   Scenario Comparisons

To best highlight the filter behavior in a concise manner, most of the results displayed are different combinations of the six scenarios. For clarity, the RMSE calculated for the

ensemble at every time step is used in Figures 54 to 61. This allows for the general behavior of the error to be viewed more simply by removing the full ensemble plots and covariance bounds.

4.7.1 Scenarios I, IS, S.

The comparison of scenarios I, IS, and S show the significant improvement in relative position RMSE using either SMV or the EKF with SMV. Figures 54 and 55 show the growth of RMSE for both Scenario I and Scenario IS until the SMV measurements are introduced. At that point, both Scenario IS and S have significantly lower RMSE than Scenario I as it continues to drift, which causes the MRSE to continue growing as well.
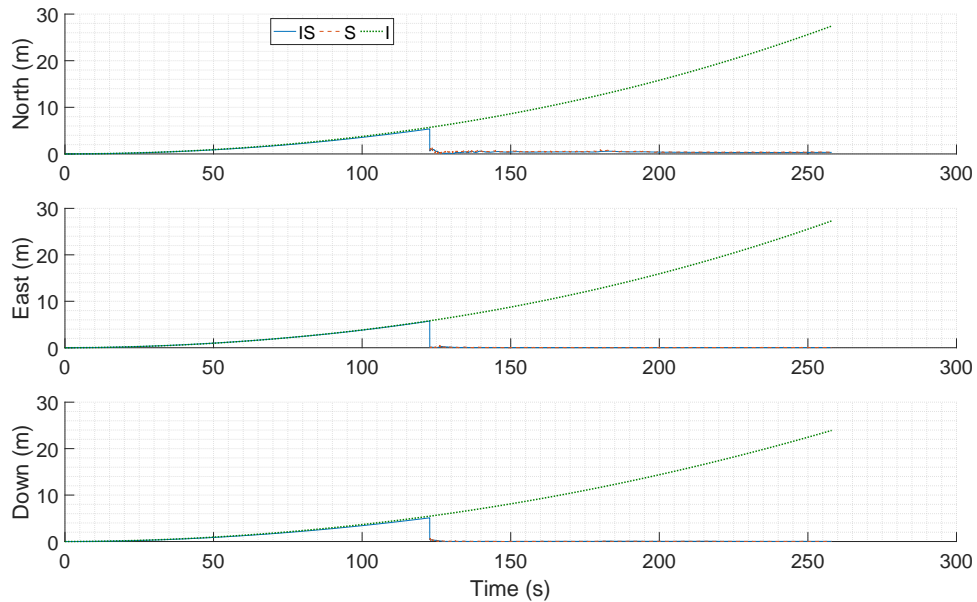
Figure 54. RMSE from Case 1, Scenarios I, IS, and S. RMSE Calculated at Each Time Step for All 100 Iterations

Figure 55. RMSE from Case 2, Scenarios I, IS, and S. RMSE Calculated at Each Time Step for All 100 Iterations

4.7.2 Scenarios IS and S.

Figures 56 and 57 show the plots of Scenario IS and S for the last 120 s of the simulations in Case 1 and 2 respectively. Note the axis are different scales in the North. This is to ensure the individual behavior of each case is still visible. In both plots the combination of INS and SMV in the EKF results in a smoother plot with lower RMSE. The spike in the North error at 180 s is seen in these plots. As discussed, this is due to the tail of the receiver aircraft leaving the FOV of the camera. The higher error from 140 s to 180 s is a factor of the specific trajectory the receiver aircraft takes. As the aircraft comes in at a higher angle, the SMV bias in the North direction increases. Overall, the Case 2 RMSE is lower in total because the SMV measurements have lower total error due to the preprocessing performed prior to incorporating the measurements into the filter. However, Scenario IS in Figure 56 reduces the SMV error more than Scenario IS in Figure 57. This is visible in the lower INS/SMV line following the SMV line.

89
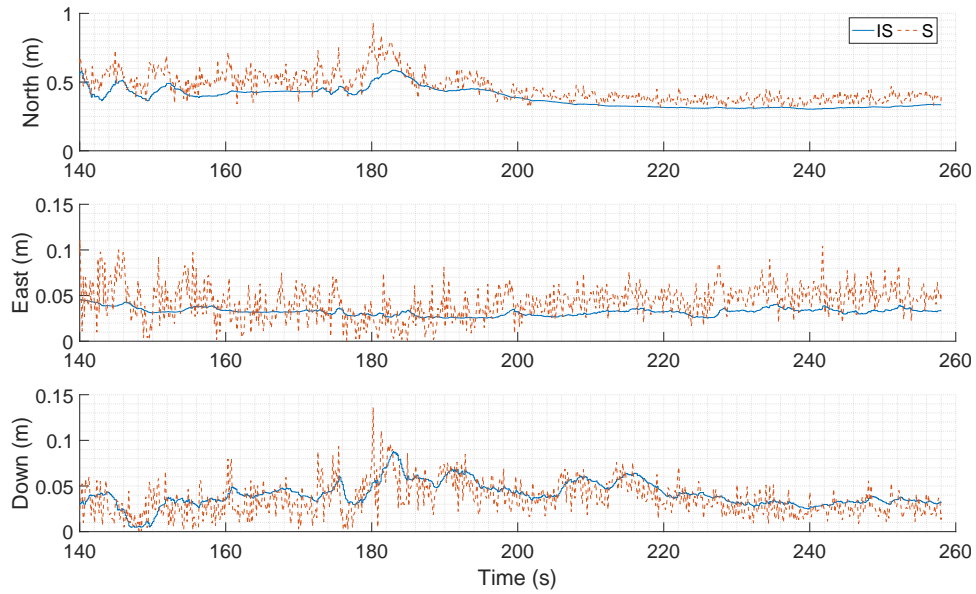
Figure 56. RMSE from Case 1, Scenarios IS and S. RMSE Calculated at Each Time Step for All 100 Iterations
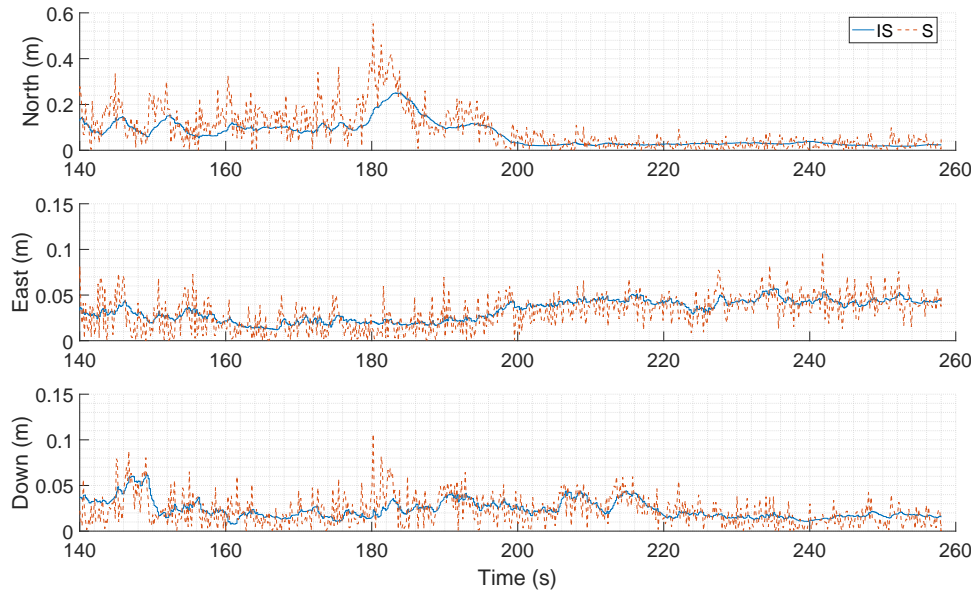
Figure 57. RMSE from Case 2, Scenarios IS and S. RMSE Calculated at Each Time Step for All 100 Iterations

4.7.3   Scenarios IS, IG, and IGS.

This section takes a closer look at the behavior of the filter when GPS measurements are included in Figures 58 and 59. A comparison of Scenarios IS, IG, and IGS is made. In both

figures, Scenario IS RMSE grows until SMV measurements are available, and then it drops sharply. During this period both Scenario IG and Scenario IGS RMSE are significantly lower and hover close to 0. Once the GPS is lost, Scenario IG begins to drift again allowing the RMSE to grow quickly. Both Scenario IS and Scenario IGS remain close to 0. The next section looks closely at these two scenarios.
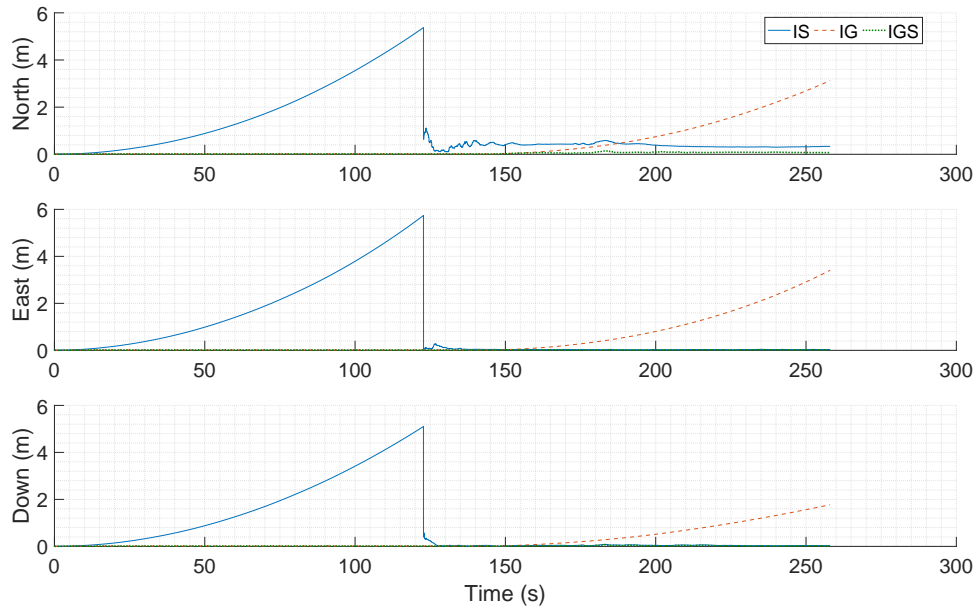
Figure 58. RMSE from Case 1, Scenarios IS, IG, and IGS. RMSE Calculated at Each Time Step for All 100 Iterations
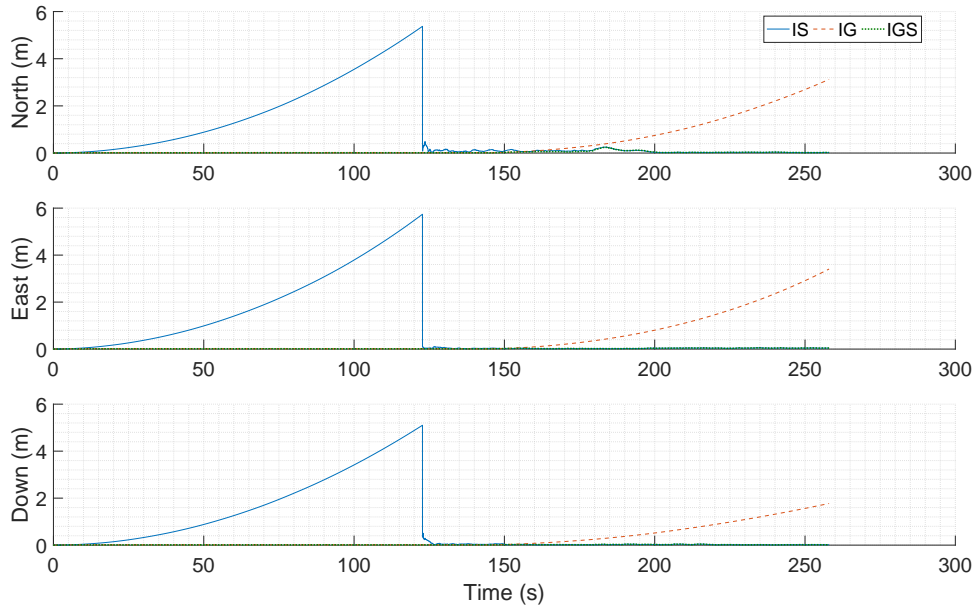
Figure 59. RMSE from Case 2, Scenarios IS, IG, and IGS. RMSE Calculated at Each Time Step for All 100 Iterations

4.7.4   Scenarios IS, IGS, and IGS/NL.

This section observes the last 120 s of Scenarios IS and IGS from Figures 58 and 59, adding in Scenario IGS/NL to observe the difference in EKF performance when DGPS is never lost. Note the axis are different scales in the North. This is to ensure the individual behavior of each case is still visible. Figures 60 and 61 show the combination of these three scenarios starting just before the DGPS solution is lost. Prior to DGPS loss, Scenario IGS and IGS/NL align so closely they cannot be distinguished from one another. However, when the DGPS signal is lost, Scenario IGS begins to drift towards Scenario IS.

In Case 1, the two lines never meet. Again, the longer time constant in Case 1 allows it to retain the bias values longer. As time progresses and the bias decorrelates over time, the Scenario IGS solution RMSE continues to approach the Scenario IS solution. In Case 2, the shorter time constant allows the SMV bias to decorrelate quickly causing Scenario IGS to quickly merge with Scenario IS. There is a period of time when it retains some of the stored SMV bias, but it is almost completely gone after 35 s. Previously in Section 4.5.1.2, this is still useful in situations where GPS is intermittent or not completely lost. The SMV bias state provides some correction for a short period of time.

92
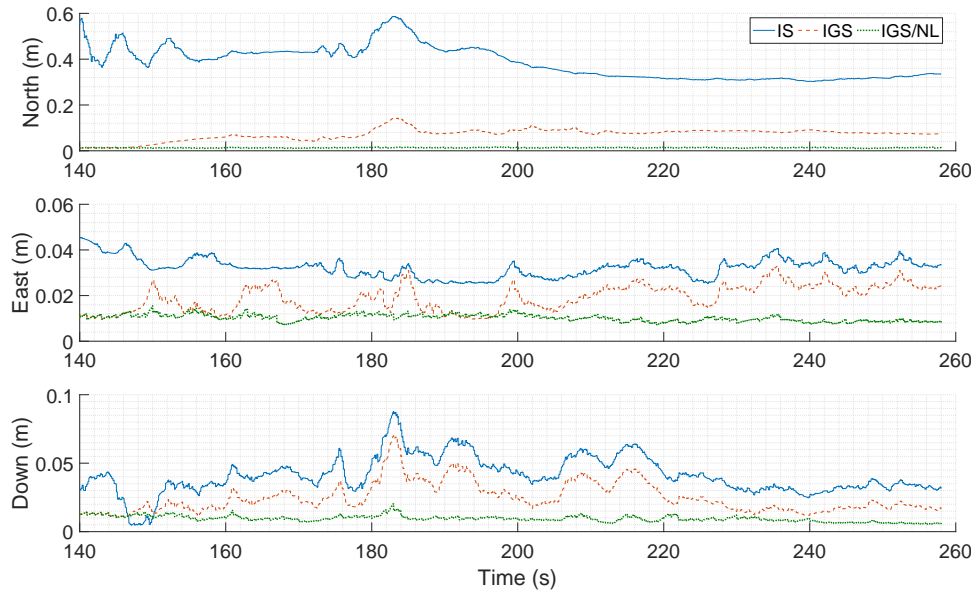
Figure 60. RMSE from Case 1, Scenarios IS, IGS, and IGS/NL. RMSE Calculated at Each Time Step for All 100 Iterations
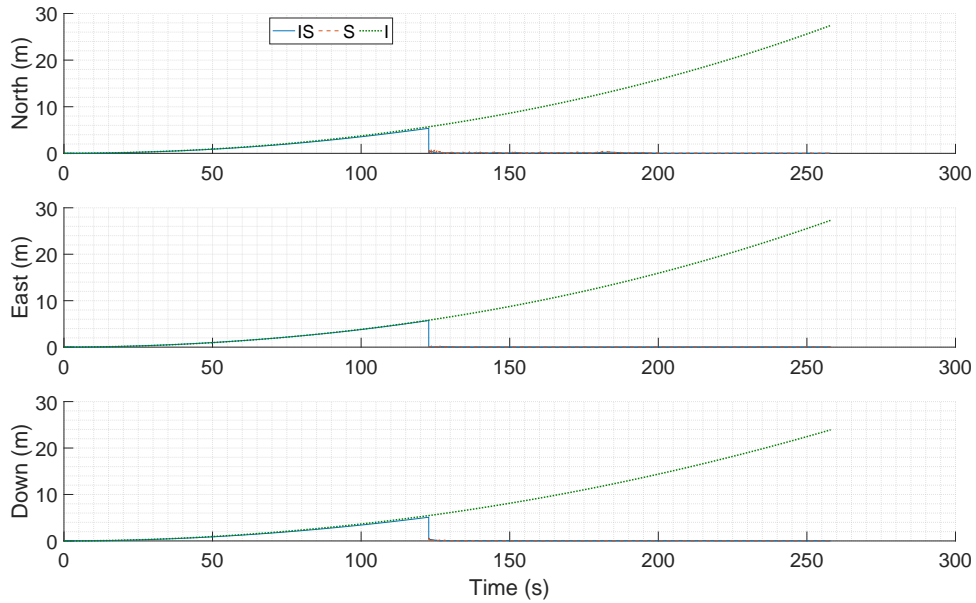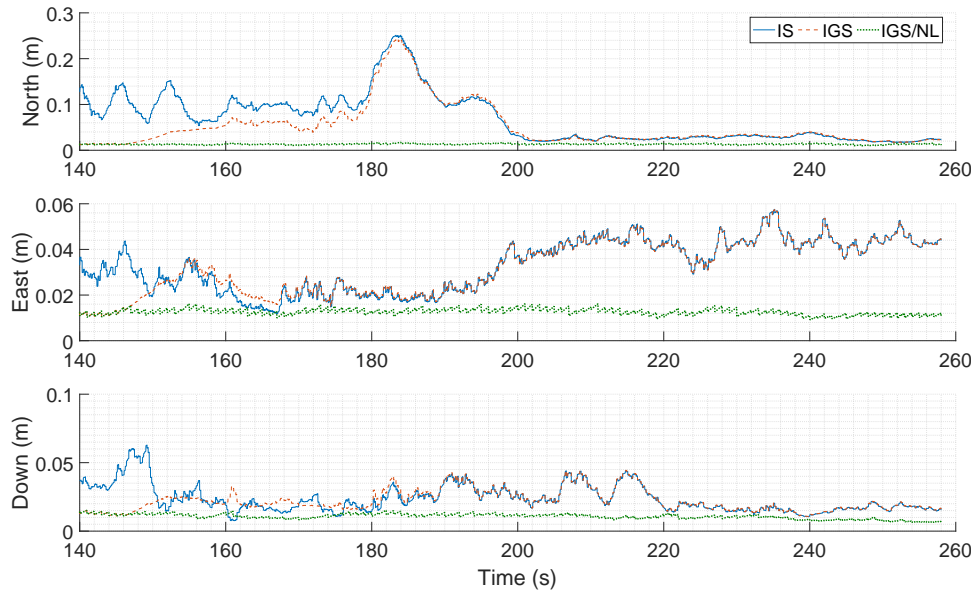

Figure 61. RMSE from Case 2, Scenarios IS, IGS, and IGS/NL. RMSE Calculated at Each Time Step for All 100 Iterations

4.8   Comparison

This final section compares all of the scenarios and cases in one set of tables. For both position and velocity, there are three tables. Each table displays the RMSE for a period

of the simulation to see general performance of the scenario. The first table looks at the entirety of the simulation. The second table looks at when the receiver is within 100 m of the tanker, when SMV measurements begin. The third table looks at when it is within 47 m. This is long enough in time, after the loss of GPS, to prevent the immediate influence of DGPS from affecting the RMSE. The last table looks at the contact point. Some of the information in the tables are presented in previous sections but it is repeated for ease of comparison.

4.8.1 Position.

This section compares the accuracy of the different scenarios and cases for position estimation. Table 10 displays the RMSE errors for the entire simulation. Scenario S, SMV only, has no values due to SMV measurements starting when the receiver is within 100 m of the tanker. As expected, Scenarios I, IS, and IG have high RMSE due to the portions of their simulations with a drifting solution. Scenarios I and IG are not discussed directly, though they are present in the tables for comparison. Both Scenario IGS and IGS/NL maintain measurements for the duration of the simulation resulting in lower RMSE values. Due to DGPS complete availability, Scenario IGS/NL had the best RMSE values. Case 1 had better RMSE than Case 2 due to its capability to estimate the SMV bias state. With the DGPS and SMV combination, it is able to continually estimate the SMV bias.

Table 10. Ensemble Relative Position RMSE for Full Trajectory in meters

Scenario	Case 1			Case 2		
	North	East	Down	North	East	Down
I	11.9	12.0	10.7	11.9	12.0	10.7
IS	1.68	1.77	1.59	1.65	1.77	1.59
S	N/A	N/A	N/A	N/A	N/A	N/A
IG	0.924	0.995	0.559	0.924	0.995	0.559
IGS	0.0549	0.0202	0.0207	0.0486	0.0252	0.0183
IGS/NL	0.0133	0.0119	0.0115	0.0133	0.0129	0.0120

Tables 11 and 12 perform the same comparison but with Scenario S values as well. These show the benefit of utilizing an EKF rather than the SMV alone. Table 11 shows RMSE values within 100 m. SMV with INS perform better than SMV alone in both cases. Case 2 outperformed Case 1 for the full duration due to the preprocessed measurements. As in Table 10, Scenario IGS and IGS/NL outperformed Scenario IS with Case 1. Scenario IGS/NL provides the best values due to SMV bias estimation. Scenario IGS/NL improves slightly between Tables 10 and 11. This is not a significant improvement, but it does show that combining the DGPS and the SMV results in better values than DGPS alone since Table 10 has portions of the trajectory with no SMV, while Table 11 has the SMV measurements. Specifically looking at filter performance, The total magnitude of error is reduced 18-33% when SMV measurements are combined with INS in the filter. Preprocessing the measurements by removing the characterized mean prior to adding them to the filter results in an 73% reduction in the estimation error.

Table 11. Ensemble Relative Position RMSE Within 100 m in meters

Scenario	Case 1			Case 2		
	North	East	Down	North	East	Down
I	16.3	16.3	14.6	16.3	16.3	14.6
IS	0.398	0.0497	0.0619	0.0945	0.0371	0.0454
S	0.487	0.0666	0.0622	0.148	0.0500	0.0532
IG	1.28	1.37	0.772	1.28	1.37	0.72
IGS	0.0712	0.0190	0.0257	0.0659	0.0324	0.0222
IGS/NL	0.0134	0.0106	0.0103	0.0133	0.0126	0.0112

Table 12 shows RMSE values within 47 m of the tanker. The relationship between the different scenarios and cases remains similar to within 100 m. Both Scenario IS and S improve slightly due to improved SMV measurements. The benefit of the filter is seen in the North direction. There are notable improvements in RMSE from the SMV alone in Scenario S to combining the SMV with the INS in Scenario IS.

Two minor inconsistencies appear as the RMSE is confined to the closer distance. The error in the Down direction increases from Scenario S to Scenario IS for Case 1. The error in the East direction also increases from Scenario S to Scenario IS for Case 1. In both inconsistencies, the difference is due to the bias state estimating biases in the wrong direction, effectively adding in additional error to each measurement. However, the change in error for both values is negligible and has little impact on overall filter performance. The total magnitude of error is reduced 16-24% when SMV measurements are combined with INS in the filter. Preprocessing the measurements prior to adding them to the filter results in an 75% reduction in the estimation error.

The Scenario IGS error increases as the range decreases. While the SMV measurements are increasing in accuracy, the bias stored during DGPS operation is decorrelating. This results in poorer bias estimation and increased error.

Table 12. Ensemble Relative Position RMSE Within 47 m in meters

	Case 1			Case 2		
Scenario	North	East	Down	North	East	Down
I	19.5	19.5	17.4	19.5	19.5	17.4
IS	0.375	0.0313	0.0458	0.082	0.0382	0.0238
S	0.445	0.0457	0.0431	0.114	0.0378	0.0271
IG	1.61	1.74	0.974	1.61	1.74	0.974
IGS	0.0851	0.0210	0.0295	0.0783	0.0381	0.0245
IGS/NL	0.0136	0.0101	0.0093	0.0135	0.0126	0.0107

Table 13 shows RMSE values within within 33 m or at the contact point. This table is displayed to show the continued improvement of the SMV system as the aircraft relative distance shrinks. For both cases the error in the East is slightly larger than in Table 12 due to an increase in the SMV bias. However, the drop in error in the North axis is much more significant. The east error increases less than 1 cm while the error in the SMV North measurements decreases by 6-8 cm. This decrease is also reflected when the measurements

are incorporated into the filter with the INS, reducing the total magnitude of the error. Looking at the IS and S results displayed, both preprocessing measurements and adding them to the filter greatly reduces the estimation error. The total magnitude of error is reduced 8-17% when SMV measurements are combined with INS in the filter. Preprocessing the measurements prior to adding them to the filter results in an 83% reduction in the estimation error.

Table 13. Ensemble Relative Position RMSE at Contact Point in meters

Scenario	Case 1			Case 2		
	North	East	Down	North	East	Down
I	23.8	23.8	21.0	23.8	23.8	21.0
IS	0.316	0.0335	0.0329	0.0273	0.0439	0.0162
S	0.379	0.0526	0.0290	0.0334	0.0457	0.0169
IG	2.33	2.50	1.37	2.33	2.50	1.37
IGS	0.0821	0.0242	0.0177	0.0284	0.0438	0.0165
IGS/NL	0.0132	0.00906	0.00785	0.0131	0.0118	0.00896

4.8.2 Velocity.

The velocity RMSE values are not discussed in much detail. Tables 14 to 17 display the velocity RMSE for the same ranges displayed for positions. Note that the units are in cm/s instead of m/s. The small RMSE for the velocities made it difficult to analyze and compare values when the larger units were used. In all cases where measurements are incorporated (SMV or DGPS), the RMSE error is less than 1 cm/s. In general, the solution improves when DGPS is added in and further improves if the DGPS is never lost. There is little difference between the two cases as the estimation of the bias does not significantly impact the velocity estimation. The levels of error observed are small enough that specific comparisons have little benefit.

Table 14. Ensemble Relative Velocity RMSE for Full Trajectory in cm/s

	Case 1			Case 2		
Scenario	North	East	Down	North	East	Down
I	12.8	12.5	10.8	12.8	12.5	10.8
IS	3.64	3.78	3.35	3.63	3.79	3.35
S	N/A	N/A	N/A	N/A	N/A	N/A
IG	2.23	2.38	1.26	2.23	2.38	1.26
IGS	0.539	0.390	0.369	0.558	0.432	0.381
IGS/NL	0.399	0.383	0.360	0.399	0.398	0.366

Table 15. Ensemble Relative Velocity RMSE Within 100 m in cm/s

	Case 1			Case 2		
Scenario	North	East	Down	North	East	Down
I	16.9	16.5	14.0	16.9	16.5	14.0
IS	0.997	0.559	0.515	0.962	0.585	0.512
S	N/A	N/A	N/A	N/A	N/A	N/A
IG	3.06	3.26	1.70	3.06	3.26	1.70
IGS	0.638	0.377	0.351	0.669	0.456	0.375
IGS/NL	0.400	0.415	0.376	0.396	0.393	0.344

Table 16. Ensemble Relative Velocity RMSE Within 47 m in cm/s

Scenario	Case 1			Case 2		
	North	East	Down		East	Down
I	18.1	18.4	14.6	18.1	18.4	14.6
IS	0.751	0.373	0.335	0.753	0.473	0.378
S	N/A	N/A	N/A	N/A	N/A	N/A
IG	3.82	4.08	2.09	3.82	4.08	2.09
IGS	0.706	0.373	0.336	0.752	0.475	0.372
IGS/NL	0.402	0.361	0.315	0.402	0.398	0.332

Table 17. Ensemble Relative Velocity RMSE at Contact in cm/s

Scenario	Case 1			Case 2		
	North	East	Down	North	East	Down
I	21.9	21.1	17.4	21.9	21.1	17.4
IS	0.579	0.371	0.299	0.563	0.449	0.317
S	N/A	N/A	N/A	N/A	N/A	N/A
IG	4.99	5.39	2.56	4.99	5.39	2.56
IGS	0.580	0.371	0.298	0.563	0.449	0.317
IGS/NL	0.393	0.362	0.293	0.393	0.389	0.309

4.9 Summary

In summary, many different combinations of sensors obtain less than 1 m accuracy. SMV alone, INS combined with SMV and INS combined with SMV and DGPS when DGPS is lost or maintained, all fall under the necessary accuracy. This chapter demonstrates a filter that successfully combines SMV with an INS but also utilizes additional DGPS measurements when available for continued, improved accuracy. SMV is best used when combined with additional sensors when available. This improves filter accuracy and also its ability to

99

estimate the SMV bias states. The filter can be tuned to specifically address this refueling simulation for improved SMV accuracy, and it can be tuned for a more generic simulation with comparable or slightly improved results.

V. Conclusion

This thesis presents a design for an EKF able to incorporate INS, SMV, and DGPS measurements to estimate the relative position of a receiver and a tanker flying a refueling trajectory. This chapter discusses the final conclusions determined from this research as well as recommendations for future research.

5.1 Conclusions

This research found it possible to design an EKF capable of fusing the SMV measurements with INS and DGPS measurements. SMV measurements were simulated with the use of 3D reprojection and ICP in a 3DVW. The simulated measurements accounted for observed biases and were broken into two types of measurements or two cases. The first uses the SMV measurements without any correction. The second incorporates the knowledge of the biases to correct for them. The EKF estimates the biases present in SMV measurements and tunes them separately for each case.

Without preprocessing, within 100 m, the SMV measurements had NED RMSE of 48.7 cm, 6.66 cm, and 6.22 cm. Incorporated into the tuned EKF and combined with the INS, the error became NED RMSE of 39.8 cm, 4.97 cm, and 6.19 cm. Fusing available DGPS measurements reduced the error further, bringing it down to NED RMSE of 7.12 cm, 1.9 cm, and 2.57 cm. With preprocessing, within 100 m, the SMV measurement NED RMSE is 14.8 cm, 5 cm, and 5.32 cm. Incorporating these measurements into the EKF tuned for preprocessed measurements with the INS reduces the error to NED RMSE of 9.45 cm, 4.14 cm, and 4.54 cm. Bringing the DGPS measurements into the EKF further reduces the error to NED RMSE of 6.59 cm, 3.24 cm, and 2.22 cm. These RMSE values reflect the trend seen in this filter design. As measurements are incorporated, relative position estimation improves, up to 18% without preprocessing and up to 33% with preprocessing, for incorporating SMV into the filter!

The SMV bias states were able to successfully estimate some of the bias values and prevent the filter covariance from collapsing When only combining the SMV and INS they

drove a more conservative filter than would be ideal with most of the filter estimates falling within the estimated covariance. Fusing additional sensors with the SMV only increased the filter accuracy and even improved the SMV inputs by enabling the filters to better estimate the SMV bias states. In all Scenarios and Cases, the EKF had no trouble estimating relative position with the required sub meter accuracy and were able to provide sub 50 cm accuracy.

5.2 Recommendations

This section outlines how this work can be improved, expanded, or further explored. SMV and AAR are relatively untouched in combination so there are many ways to improve estimation for AAR.

5.2.1 Attitude Measurements.

This work assumes a navigation grade IMU and a well known starting position and attitude. Combined with the knowledge the SMV attitude measurements lack accuracy the decision was made to leave them out of this simulation. Practically, a receiver's navigation system operates for a period of time prior to rendezvousing with the tanker. Even with a navigation grade IMU attitude errors impacting estimation may still exist. Implementing and testing an attitude measurement processor allows future simulations and flight tests to examine how SMV can be used to bring in attitude measurements as well as position measurements for a complete solution. To accomplish this with the current model, a commercial grade IMU with significant drift could be used to incorporate the current attitude measurements.

5.2.2 Adaptive Filtering.

An issue in designing this filter was characterizing the SMV behavior in a way that provided measurement accuracies. The current characterization is inherently simulation specific and may not be representative of complete SMV behavior. Adaptive filtering provides a possible avenue to avoid having to characterize the error in that fashion. While it

may not directly deal with the bias', adaptive filtering could provide a flexible solution for incorporating SMV measurements under a wide range of scenarios.

5.2.3 Unscented Kalman Filter.

This filter utilizes a set of linearized INS error equations for the filter system dynamics. Fully modeling the dynamics decreases the magnitude of any linearizion errors. Executing the non-linear dynamics as an Unscented kalman Filter (UKF) may improve the solution. The dynamics in this filter are well-developed, so it is possible a UKF solution would not provide much improvement.

5.2.4 Residual Monitoring.

Residual monitoring may help protect the system against uncharacterized errors. Ideally, the SMV algorithm is robust and able to filter out potential sources of error. However, if a measurement slips through containing a larger than expected error, a method may be necessary to protect the filter from incorporating the error. A residual monitor may identify these measurements. While it may not protect against the gradually moving bias observed in the measurements, it may protect against a sudden change in error such as when the tail of the aircraft leaves the FOV.

5.2.5 Robust SMV.

The majority of the filter design for this research is done to incorporate the SMV data that was previously unknown, but not necessarily to improve upon it. Through simulation the behavior of the algorithm was approximated to allow design choices to be made to help the filter read the data. Exploration in three different areas could benefit this work. First, simply improving the SMV algorithm could greatly improve the filter's function. Reductions in the SMV bias and magnitude of error will make it easier to design the filter to incorporate the measurements.

Second, better characterizing the SMV behavior could provide a more robust filter design. Currently it is not know exactly how the SMV will operate in different situations.

Obtaining more data on the sensors behavior in different situations will aid in designing filters to incorporate the data. Specifically, obtaining a large real-world data set will enable study of SMV algorithms behaviors. It is hard to tell currently if behaviors are due to the algorithm in general, or to the specific simulation it was run through.

Third, better modeling the SMV system directly influences the filter's ability to incorporate the data. This is closely related to characterizing the behavior but can be different. It may be necessary to more accurately characterize the data in order to better model it. One of the weaknesses of this filter design is the relatively inflexible FOGM bias state used to model the SMV system. If the bias or other behaviors can be accurately modeled, the filter will incorporate the SMV measurements with less error.

5.2.6   Boom Modeling.

This research did not evaluate the SMV performance with the simulated boom. The boom location places it directly in the middle of the stereo camera system view blocking a significant portion of the receiver aircraft. While some initial testing was done to design a mask for the boom and generate initial measurements, the measurements were not characterized or run through the filter. In order to implement a vision based system in AAR, it will need to function even when the boom obstructs the view.

Bibliography

1. J. A. Curro II. *Automated Aerial Refueling Position Estimation Using a Scanning Li-DAR*. MS thesis, AFIT/ENG/12-11. Graduate School of Engineering and Management, Air Force Institute of Technoolgy (AU), Wright-Patterson AFB, OH, Mar 2012 (AD-A562501).

2. M. Mammarella, G. Campa, M. R. Napolitano, and M. L. Fravolini, "Comparison of Point Matching Algorithms for the UAV Aerial Refueling Problem," *Machine Vision and Applications*, vol. 21, no. 3, pp. 241–251, Apr 2010.

3. M. L. Fravolini, V. Brunori, A. Ficola, M. La Cava, and G. Campa, "Feature Matching Algorithms for Machine Vision Based Autonomous Aerial Refueling," in *Proceedings of the 14th Mediterranean Conference on Control and Automation*, pp. 1–8. IEEE, 2006.

4. M. Mammarella, G. Campa, M. R. Napolitano, M. L. Fravolini, Y. Gu, and M. G. Perhinschi, "Machine Vision/GPS Integration Using EKF for the UAV Aerial Refueling Problem," *Institute of Electrical and Electronic Engineers Transactions on Systems, Man and Cybernetics Part C: Applications and Reviews*, vol. 38, no. 6, pp. 791–801. Sep 2008.

5. G. Campa, M. L. Fravolini, A. Ficola, M. R. Napolitano, B. Seanor, and M. G. Perhinschi, "Autonomous Aerial Refueling for UAVs Using a Combined GPS-Machine Vision Guidance," in *Proceeedings of AIAA Guidance, Navigation and Control Conference and Exhibit*, pp. 1–11. AIAA, 2004.

6. M. L. Fravolini, M. Mammarella, G. Campa, M. R. Napolitano, and M. Perhinschi, "Machine Vision Algorithms for Autonomous Aerial Refueling for UAVs Using the USAF Refueling Boom Method," in *Innovations in Defence Support Systems-1*, ser. Studies in Computational Intelligence, A. Finn and L. C. Jain, Eds., vol. 304, pp. 95–138. Springer Berlin Heidelberg, 2010.

7. M. L. Fravolini, G. Campa, M. Napolitano, and A. Ficola, "Evaluation of Machine Vision Algorithms for Autonomous Aerial Refueling for Unmanned Aerial Vehicles," *Journal of Aerospace Computing, Information, and Communications*, vol. 4, no. 9, pp. 968–958, Sep 2007.

8. K. P. Werner. *Precision Relative Positioning for Automated Aerial Refueling from a Stereo Imaging System.* MS thesis, AFIT/ENG/15M-048. Graduate School of Engineering and Management, Air Force Institute of Technoolgy (AU), Wright-Patterson AFB, OH, Mar 2015.

9. "Berlin blockade and airlift," in *Encyclopadia Britannica.* Encyclopaedia Britannica, Inc., 2015. [Online]. Available: https://www.britannica.com/event/ Berlin-blockade-and-airlift. Retrieved on 6 Feb 2017.

10. (2013, Aug) Air force core missions. USAF. [Online]. Available: http://www.af. mil/News/ArticleDisplay/tabid/223/Article/466868/air-force-core-missions.aspx. Retrieved on 6 February 2017.

11. "Unmanned Aircraft Systems (UAS) Service Demand 2015-2035: Literature Review and Projections of Future Usage," Version 0.1, U.S. Department of Transportation John A. Volpe National Transportation Systems Center, Cambridge, MA, Tech. Rep. DOT-VNTSC-Dod-13-01, Sep 2013.

12. M. Orton. (2009, Jan) Air force remains committed to unmanned aircraft systems. USAF. [Online]. Available: http://www.af.mil/News/ArticleDisplay/tabid/223/ Article/121391/air-force-remains-committed-to-unmanned-aircraft-systems.aspx. Retrieved on 6 February 2017.

13. C. J. Spinelli. *Development and Testing of a High-Speed Real-Time Kinematic Precise DGPS Positioning System Between Two Aircraft.* MS thesis, AFIT/ENG/06-12. Graduate School of Engineering and Management, Air Force Institute of Technoolgy (AU), Wright-Patterson AFB, OH, Sep 2006.

14. E. A. Olsen, C.-W. Park, and J. P. How, "3D Formation Flight using Differential Carrier-phase GPS Sensors," *Navigation*, vol. 46, no. 1, pp. 35–48, Mar 1999.

15. S. M. Khanafseh and B. Pervan, "Autonomous Airborne Refueling of Unmanned Air Vehicles Using the Global Positioning System," *Journal of Aircraft*, vol. 44, no. 5, pp. 1670–1682. Sep 2007.

16. J. Valasek, K. Gunnam, J. Kimmett, M. D. Tandale, J. L. Junkins, and D. Hughes, "Vision-based Sensor and Navigation System for Autonomous Air Refueling," *Journal of Guidance Control and Dynamics*, vol. 28, no. 5, pp. 979–989. Oct 2005.

17. J. Valasek, J. Kimmett, D. Hughes, K. Gunnam, and J. L. Junkins, "Autonomous Aerial Refueling Utilizing a Vision Based Navigation System," in *Proceedings of the AIAA Guidance, Navigation, and Control Conference and Exhibit*, vol. 4469, pp. 1–11. AIAA, 2002.

18. K. W. Colson Jr. *Toward Automated Aerial Refueling: Relative Navigation with Structure from Motion.* MS thesis, AFIT/ENG/16M-009. Graduate School of Engineering and Management, Air Force Institute of Technoolgy (AU), Wright-Patterson AFB, OH, Mar 2016.

19. B. D. Denby. *Toward Automated Aerial Refueling: Real Time Position Estimation with Stereo Vision.* MS thesis, AFIT/ENG/16M-252. Graduate School of Engineering and Management, Air Force Institute of Technoolgy (AU), Wright-Patterson AFB, OH, Mar 2016.

20. G. Campa, M. R. Napolitano, and M. L. Fravolini, "Simulation Environment for Machine Vision Based Aerial Refueling for UAVs," *Institute of Electrical and Electronics Engineers Transactions on Aerospace and Electronic Systems*, vol. 45, no. 1, pp. 138–151. Jan 2009.

21. M. Mammarella, G. Campa, M. R. Napolitano, and B. Seanor, "GPS / MV Based Aerial Refueling for UAVs," in *Proceedings of the AIAA Guidance, Navigation and Control Conference and Exhibit*, pp. 1–16. AIAA, 2008.

22. W. R. Williamson, G. J. Glenn, V. T. Dang, J. L. Speyer, S. M. Stecko, and J. M. Takacs, "Sensor Fusion Applied to Autonomous Aerial Refueling," *Journal of Guidance, Control, and Dynamics*, vol. 32, no. 1, pp. 262–275. Feb 2009.

23. Y. Xu, D. Luo, N. Xian, and H. Duan, "Pose Estimation for UAV Aerial Refueling with Serious Turbulences Based on Extended Kalman filter," *Optik*, vol. 125, no. 13, pp. 3102–3106, Jul 2014.

24. T. J. Barnidge and J. L. Tchon, "3D Display Considerations for Rugged Airborne Environments," in *Proceedings of the SPIE 9470 Display Technologies and Applications for Defense, Security and Avionics IX*, vol. 9470, pp. 1–9.   SPIE, 2015.

25. A. Fosbury and J. Crassidis, "Relative Navigation of Air Vehicles," *Journal of Guidance, Control, and Dynamics*, vol. 31, no. 4, pp. 824–834. Jul 2008.

26. S. Nykl, C. Mourning, E. Nykl, D. Chelberg, and T. Skidmore, "JPALS Visualization Tool," in *Proceedings of the Institute of Electrical and Electronics Engineers International Symposium on Distributed Simulation and Real-Time Applications*, pp. 3–10. IEEE, 2012.

27. S. Nykl, C. Mourning, N. Ghandi, and D. Chelberg, "A Flight Tested Wake Turbulence Aware Altimeter," in *Proceedings of the International Symposium on Visual Computing*, ser. Lecture Notes in Computer Science, G. Bebis, Ed., vol. 6939, pp. 219–228.   Springer Berlin Heidelberg, 2011.

28. C. Parsons and S. Nykl, "Real-Time Automated Aerial Refueling Using Stereo Vision," in *Proceedings of the International Symposium on Visual Computing*, ser. Lecture Notes in Computer Science, vol. 10072, pp. 605–615.   Cham, Switzerland: Springer International Publishing, 2016.

29. T. Stuart. *Stereo Vision Based Integrity Monitor for Automated Aerial Refueling.* MS thesis. Graduate School of Engineering and Management, Air Force Institute of Technoolgy (AU), Wright-Patterson AFB, OH (unpublished).

30. "BlueMax6: Aircraft Flight Dynamics, Flight Path Generator, Maneuver, Mission, and Aero-Performance Evaluation Model," Software Package, Ver. 1.0, Defense Systems Information Analysis Center, Belcamp, MD, 2014.

31. P. D. Groves, *Applied Mathematics in Integrated Navigation Systems*, 2nd ed. Boston: Artech House, 2013. ch. 2.

32. "World Geodetic System 1984: Its Definition and Relationships with Local Geodetic Systems," National Imagery and Mapping Agency TR8350.2, St. Louis, MO, Tech. Rep., Jan 2000.

33. P. S. Maybeck, in *Stochastic Models, Estimation, and Control*, ser. Mathematics in Science and Engineering, R. Bellman, Ed., vol. 141, ch. 6 and 12. New York: Academic Press, 1982.

34. D. H. Titterton and J. L. Weston, in *Strapdown Inertial Navigation Technology*, 2nd ed., ser. The Institute of Engineering and Technology Radar, Sonar, Navigation and Avionics Series, N. Stewart and H. Griffiths, Eds., vol. 17, ch. 3. London: The Institute of Engineering and Technology, 2004.

35. W. S. Flenniken IV, J. H. Wall, and D. M. Bevly, "Characterization of Various IMU Error Sources and the Effect on Navigation Performance," in *Proceedings of the ION GNSS Conference*, pp. 967–978. Fairfax, VA: ION, 2005.

36. P. Misra and P. Enge, *Applied Mathematics in Integrated Navigation Systems*, 2nd ed. Lincoln, MA: Ganga-Jamuna Press, 2013. ch. 2, 6 and 7.

37. G. Warwick, "AFRL Advances Autonomous Aerial Refueling," *AeroSpace Daily & Defense Report*, pp. 1–2, Jun 2008. [Online]. Available: http://aviationweek.com/awin/afrl-advances-autonomous-aerial-refueling. Retrieved on 18 Nov 2016.

38. J. M. Howard and M. J. Veth, "Image Aided Relative Navigation for Air Vehicles Using a Passive Statistical Predictive Rendering Approach," in *Proceedings of the 24th*

International Technical Meeting of the Satellite Division of the Institude of Navigation, pp. 3546–3556. ION, 2011.

39. A. D. Weaver. *Using Predictive Rendering as a Vision-Aided Technique for Autonomous Aerial Refueling.* MS thesis, AFIT/ENG/09-45. Graduate School of Engineering and Management, Air Force Institute of Technoolgy (AU), Wright-Patterson AFB, OH, Mar 2009 (AD-A796715).

40. S. M. Calhoun, J. Raquet, and J. Curro, "Flight Test Evaluation of Image Rendering Navigation for Close-Formation Flight," in *Proceedings of the 25th International Technical Meeting of the Satellite Division of the Institute of Navigation*, pp. 826–832. ION, 2012.

41. M. L. Fravolini, A. Ficola, M. R. Napolitano, G. Campa, and M. G. Perhinschi, "Development Of Modelling And Control Tools For Aerial Refueling For UAVs," in *Proceedings of the AIAA Guidance, Navigation, and Control Conference and Exhibit*, pp. 1–10. AIAA, 2003.

42. M. L. Fravolini, A. Ficola, G. Campa, M. R. Napolitano, and B. Seanor, "Modeling and Control Issues for Autonomous Aerial Refueling for UAVs Using a Probe-drogue Refueling System," *Aerospace Science and Technology*, vol. 8, no. 7, pp. 611–618, Oct 2004.

43. D. B. Wilson, A. H. Goktogan, and S. Sukkarieh, "A Vision Based Relative Navigation Framework for Formation Flight," in *Proceedings of the IEEE International Conference on Robotics and Automation*, pp. 4988–4995. IEEE, 2014.

44. W. Ding, J. Wang, and A. Almagbile, "Adaptive Filter Design for UAV Navigation with GPS/INS/Optic Flow integration," in *Proceedings of the International Conference on Electrical and Control Engineering*, pp. 4623–4626. IEEE, 2010.

45. X. Wang, N. Cui, and J. Guo, "INS/VisNav/GPS Relative Navigation System for UAV," *Aerospace Science and Technology*, vol. 28, no. 1, pp. 242–248, Jul 2013.

46. M. Ding, L. Wei, and B. Wang, "Vision-based Estimation of Relative Pose in Autonomous Aerial Refueling," *Chinese Journal of Aeronautics*, vol. 24, no. 6, pp. 807–815. Dec 2011.

47. J. H. Spencer. *Optical Tracking for Relative Positioning in Automated Aerial Refueling.* MS thesis, AFIT/GE/ENG/07-22. Graduate School of Engineering and Management, Air Force Institute of Technoolgy (AU), Wright-Patterson AFB, OH, Mar 2007.

48. S. Nedevschi, R. Danescu, D. Frentiu, T. Marita, F. Oniga, C. Pocol, R. Schmidt, and T. Graf, "High accuracy stereo vision system for far distance obstacle detection," in *Proceedings of the IEEE Intelligent Vehicles Symposium*, pp. 292–297. IEEE, 2004.

49. G. Hager, "A Modular System for Robust Positioning Using Feedback from Stereo Vision," *IEEE Transactions on Robotics and Automation*, vol. 13, no. 4, pp. 582–595, Aug 1997.

50. M. Maimone and L. Matthies, "Visual Odometry on the Mars Exploration Rovers," in *Proceedings of the IEEE International Conference on Systems, Man and Cybernetics*, vol. 1, pp. 903–910. IEEE, 2005.

51. P. Corke, "An Inertial and Visual Sensing System for a Small Autonomous Helicopter," *Journal of Robotic Systems*, vol. 21, no. 2, pp. 43–51, Jan 2004.

52. L. R. G. Carrillo, A. E. D. López, R. Lozano, and C. Pégard, "Combining Stereo Vision and Inertial Navigation System for a Quad-rotor UAV," *Journal of Intelligent and Robotic Systems*, vol. 65, no. 1-4, pp. 373–387, Jan 2012.

53. J. Kelly, S. Saripalli, and G. S. Sukhatme, "Combined Visual and Inertial Navigation for an Unmanned Aerial Vehicle," in *Field and Service Robotics*, ser. Springer Tracts in Advanced Robotics, R. Siegwart and C. Laugier, Eds., vol. 42, pp. 255–264. Springer Berlin Heidelberg, 2008.

54. R. E. Bowers. *Estimation Algorithm for Autonomous Aerial Refueling.* MS thesis. Texas A&M, College Station, TX, Aug 2005.

55. M. Achtelik, A. Bachrach, R. He, S. Prentice, and N. Roy, "Stereo Vision and Laser Odometry for Autonomous Helicopters in GPS-denied Indoor Environments," in *Proceedings of the SPIE 7332 Unmanned Systems Technology XI*, G. R. Gerhart, D. W. Gage, and C. M. Shoemaker, Eds., vol. 7332, pp. 19:1–10.   SPIE, 2009.

56. M. Agrawal and K. Konolige, "Real-time Localization in Outdoor Environments using Stereo Vision and Inexpensive GPS," in *Proceedings of the 18th International Conference on Pattern Recognition (ICPR'06)*, vol. 3, pp. 1063–1068.   IEEE, 2006.

57. *Scorpion.* Version 0.8 Computer software. Autonomy Navigation Technology Center. Wright-Patterson AFB, OH, 2017. [Online]. Available: https://github.com/ANTCenter.

58. B. M. Scherzinger and D. B. Reid, "Modified strapdown inertial navigator error models," in *Proceedings of the Position Location and Navigation Symposium*, pp. 426–430. IEEE, 1994.

59. D. Goshen-Meskin and I. Y. Bar-Itzhack, "Unified approach to inertial navigation system error modeling," *Journal of Guidance, Control, and Dynamics*, vol. 15, no. 3, pp. 648–653, Jun 1992.

60. (2016) Terrain elevation data. Department of the Interior USGS. [Online]. Available: https://earthexplorer.usgs.gov/. Retrieved on 9 November 2016.

61. (2016) Satellite imagery. Microsoft. [Online]. Available: https://www.bing.com/maps. Retrieved on 9 November 2016.

62. *FLY.* Version 1.0, Computer software. Autonomy Navigation Technology Center. Wright-Patterson AFB, OH, 2017.

63. *Geo-RelNAV High-Accuracy, Real-Time Relative Positioning and Orientation System Data Sheet*, Geodetics, Inc., San Diego, CA. [Online]. Available: http://www.navtechgps.com/assets/1/7/GeoRelNav_DS.pdf. Retrieved on 22 Nov 2016.

64. *1750 IMU Fiber Optic Gyro Inertial Measurement Unit*, KVH Industries, Inc., Middletown, RI. [Online]. Available: http://www.kvh.com/Military-and-Government/ Gyros-and-Inertial-Systems-and-Compasses/Gyros-and-IMUs-and-INS/IMUs/ 1750-IMU.aspx. Retrieved on 22 Nov 2016.

65. G. Bradski, "The OpenCV Library," *Dr. Dobb's Journal of Software Tools*, 2000.

66. *Matlab*. Version 9.0.0.341360 (R2016a), Computer software. The MathWorks Inc. Natick, MA, 2016.

67. J. Robinson, M. Piekenbrock, L. Burchett, S. Nykl, B. Woolley, and A. Terzuoli, "Parallelized Iterative Closest Point for Autonomous Aerial Refueling," in *Proceedings of the International Symposium on Visual Computing*, ser. Lecture Notes in Computer Science, vol. 10072, pp. 593–602. Cham, Switzerland: Springer International Publishing, 2016.

68. *Matlab Computer Vision System Toobox*. Version 7.1 (R2016a), Computer software. The MathWorks Inc. Natick, MA, 2016.

69. P. Besl and N. McKay, "A Method for Registration of 3-D Shapes," *Institute of Electrical and Electronics Engineers Transactions on Pattern Analysis and Machine Intelligence*, vol. 14, no. 2, pp. 239–256, Feb 1992.

REPORT DOCUMENTATION PAGE

Form Approved
OMB No. 0704–0188

1. REPORT DATE *(DD–MM–YYYY)*	2. REPORT TYPE	3. DATES COVERED *(From — To)*
03–23–2017	Master's Thesis	Sept 2015 — Mar 2017

4. TITLE AND SUBTITLE

Combined Stereo Vision and Inertial Navigation for Automated Aerial Refueling

5a. CONTRACT NUMBER

5b. GRANT NUMBER

5c. PROGRAM ELEMENT NUMBER

6. AUTHOR(S)

Johnson, Daniel T., Capt, USAF

5d. PROJECT NUMBER

17G170

5e. TASK NUMBER

5f. WORK UNIT NUMBER

7. PERFORMING ORGANIZATION NAME(S) AND ADDRESS(ES)

Air Force Institute of Technology
Graduate School of Engineering and Management (AFIT/EN)
2950 Hobson Way
WPAFB OH 45433-7765

8. PERFORMING ORGANIZATION REPORT NUMBER

AFIT-ENG-MS-17-M-036

9. SPONSORING / MONITORING AGENCY NAME(S) AND ADDRESS(ES)

Air Force Research Lab Aerospace Systems Directorate Power and Control Div
2130 8th Street, Bldg 45, Room 190
WPAFB OH 45433-7765
COMM 937-938-4617
Email: ba.nguyen@us.af.mil

10. SPONSOR/MONITOR'S ACRONYM(S)

AFRL/RQQC

11. SPONSOR/MONITOR'S REPORT NUMBER(S)

12. DISTRIBUTION / AVAILABILITY STATEMENT

DISTRIBUTION STATEMENT A:
APPROVED FOR PUBLIC RELEASE; DISTRIBUTION UNLIMITED.

13. SUPPLEMENTARY NOTES

This material is declared a work of the U.S. Government and is not subject to copyright protection in the United States

14. ABSTRACT

This paper describes the design of an EKF to obtain the precise relative position of two aircraft in a refueling maneuver while operating in GPS denied environments. The EKF uses the INS already present in both aircraft as well as the stereo camera system organic to new tanker systems. The aircraft trajectories are generated according to authentic refueling profiles with flight dynamics software and executed in a 3D virtual environment to enable deterministic simulation of the stereo camera system and to demonstrate the effectiveness of the combined system in a refueling scenario. Results show the system can achieve sufficient accuracy utilizing only SMV and INS measurements, though the system is capable of incorporating GPS measurements when available for an additional increase in accuracy.

15. SUBJECT TERMS

Kalman Filter, Stereo Vision, Automated Aerial Refueling, Relative Navigation

16. SECURITY CLASSIFICATION OF:			17. LIMITATION OF ABSTRACT	18. NUMBER OF PAGES	19a. NAME OF RESPONSIBLE PERSON
a. REPORT	b. ABSTRACT	c. THIS PAGE			Dr. Scott Nykl, AFIT/ENG
U	U	U	U	131	19b. TELEPHONE NUMBER *(include area code)* (937) 255-3636, x4395; scott.nykl@afit.edu

Standard Form 298 (Rev. 8–98)
Prescribed by ANSI Std. Z39.18